


2016

On-orbit Inter-satellite Radiometric Calibration of Cross-track Scanning Microwave Radiometers

Hamideh Ebrahimi
University of Central Florida

 Part of the [Electrical and Computer Engineering Commons](#)
Find similar works at: <https://stars.library.ucf.edu/etd>
University of Central Florida Libraries <http://library.ucf.edu>

This Doctoral Dissertation (Open Access) is brought to you for free and open access by STARS. It has been accepted for inclusion in Electronic Theses and Dissertations, 2004-2019 by an authorized administrator of STARS. For more information, please contact STARS@ucf.edu.

STARS Citation

Ebrahimi, Hamideh, "On-orbit Inter-satellite Radiometric Calibration of Cross-track Scanning Microwave Radiometers" (2016). *Electronic Theses and Dissertations, 2004-2019*. 5250.
<https://stars.library.ucf.edu/etd/5250>

**ON-ORBIT INTER-SATELLITE RADIOMETRIC
CALIBRATION OF CROSS-TRACK SCANNING MICROWAVE
RADIOMETERS**

by

HAMIDEH EBRAHIMI

B.S. Tehran Polytechnic University, 2008
M.S. Tehran Polytechnic University, 2011

A dissertation submitted in partial fulfillment of the requirements
for the degree of Doctor of Philosophy
in the Department of Electrical Engineering and Computer Science
in the College of Engineering and Computer Science
at the University of Central Florida
Orlando, Florida

Fall Term
2016

Major Professor: W. Linwood Jones

© 2016 Hamideh Ebrahimi

ABSTRACT

This dissertation concerns the development of an improved algorithm for the inter-satellite radiometric calibration (XCAL) for cross track scanning microwave radiometers in support of NASA's Global Precipitation Mission (GPM). This research extends previous XCAL work to assess the robustness of the CFRSL "double difference" technique for sounder X-CAL. In this work, using a two-year of observations, we present a statistical analysis of radiometric biases performed over time and viewing geometry.

In theory, it is possible to apply the same X-CAL procedure developed for conical-scanning radiometers to cross-track scanners; however the implementation is generally more tedious. For example, with the cross-track scan angle, there is a strong response in the observed T_b due to changes in the atmosphere slant path and surface emissivity with the Earth incidence angle. For ocean scenes this is trivial; however for land scenes there is imperfect knowledge of polarized emissivity. However, for the sounder channels the surface emissivity is not the dominant component of top-of-the-atmosphere T_b , which is a mitigating factor. Also, cross-track scanners introduce changes in the radiometer antenna observed polarization with scan angle. The resulting observation is a mixture of un-polarized atmospheric emissions and vertical and horizontal polarized surface emissions. The degree of polarization mixing is known from geometry; however, reasonable estimates of the surface emissivity are required, which complicate over land comparisons. Finally, the IFOV size monotonically increases over the cross-track scan. Thus, when inter-comparing cross-track scanning radiometers, it will be necessary to carefully consider these effects when performing the double difference procedure.

To my dearest parents and brothers

And to all who inspired me

ACKNOWLEDGMENTS

This was quite a journey, and I would not have made it to this step alone. Therefore, I would like to extend my gratitude to those who made this possible.

First and foremost, I would like to express my sincere appreciation to my advisor, Dr. W. Linwood Jones. I thank him for his encouragement and support during the development of this work. He has been more than a mentor for me, and always been there for me. He is one of the best teachers I know, and I hope that I could be as lively and energetic as him, and to someday be able to command an audience as well as he can.

In addition, I would like to thank my committee members: Dr. Thomas Wilheit, Dr. James Wang, Dr. Wasfy Mikhael, and Dr. Parveen Wahid. Particularly, I like to thank Dr. Wang for accepting to be in my committee regardless of his retirement, and for his peer revision of my dissertation.

I would like to thank the NASA GPM XCAL team. As a member of them, I learned a lot by interacting with them. The team members I would like to thank include but not limited to Dr. Thomas Wilheit, Dr. James Wang, Dr. Wesley Berg, Dr. Erich Stocker, Dr. Vivienne Payne, Dr. Saswati Data, Dr. Rachael Kroodsma, Steve Bilanow, Dr. Darren Mckague, and Dr. John Xun Yang. Also I would like to thank NASA PPS team Dr. Yimin Ji, and Dr. Joyce Chou for their endless support.

I like to thank my professors and friends in the college of Optics and Photonics and Planetary Sciences Department, attending their classes and seminars broaden my horizons. Particularly I would like to thank Dr. Joseph Harrington, Dr. Daniel Britt, and Dr. Boris Y. Zeldovich.

I would like to Thanks Dr. Isaac Moradi, and Ralph Ferraro from the Earth System Science Interdisciplinary Center at University of Maryland-College Park, for giving me the opportunity to collaborate with them. Working there has been a great opportunity for me to interact with other scientists and engineers from NOAA, NASA, and broaden my knowledge in Earth Sciences.

I would like to thank my friends and colleagues at CFRSL, Spencer Farrar, Yazan Hejazin, Zoubair Ghazi, Larry Schneider, Saleem Sahawneh, Ruiyao Chen, Faisal Alquaied, Abdoulsalam Alasgah, Andrea Santos, and Maria Marta Jacob; for all the insightful discussions that we had on different topics, and all their support. To Mrs. Beverly Jones for all her kindness and her heavenly baked goodies.

Special thanks to my amazing friends, which always are there for me: Zahoora Sanjabi, Milad Hooshyar, Rouhollah Rahmatizadeh, Anahita Davoudi, Behnaz Seyfi, Sara Bakhshi, Zahra Hooshmand, and Maedeh Fasihi.

Last but not least, I would like to thank my beloved parents. I have never been this far away for this long. I am always grateful for their unconditional love and their limitless sacrifices. Thanks to my wonderful brothers: Hossein, Hassan, Hamed. I am so blessed to have them in my life, and I could not have asked for a better siblings.

Finally, I would like to acknowledge that the financial support to pursue my PhD program was sponsored by various NASA grants.

TABLE OF CONTENTS

ABSTRACT.....	iii
ACKNOWLEDGMENTS	v
TABLE OF CONTENTS.....	vii
LIST OF FIGURES	x
LIST OF TABLES	xv
CHAPTER 1: INTRODUCTION	1
1.1 Principle of Radiometric Measurements	1
1.2 Inter-calibration Description	3
1.3 Global Precipitation Measurement Mission	5
1.4 Dissertation Objective and Overview	9
CHAPTER 2: DOUBLE DIFFERENCES TECHNIQUE.....	11
2.1 Radiative Transfer Model.....	13
2.2 Mixed Polarization	18
2.3 RTM Environmental Parameters.....	20
2.3.1 GDAS Data	20
2.3.2 ERA-Interim Data	20
2.3.3 Salinity Data.....	22
2.4 Relative Humidity	24
2.5 Relative Humidity Derived From SAPHIR	26

2.6	GPS Radio Occultation	26
2.6.1	Advantages and Disadvantages of GPS-RO	28
2.6.2	Relative Humidity Estimates	30
2.6.3	RTM Analysis Around 183.31 GHz	31
2.6.4	Changes of EIA and IFOV Resolution	32
CHAPTER 3: SENSORS AND CALIBRATION		42
3.1	Cross Track Scanners versus Conical Scanners	42
3.1.1	Cross Track Sensors.....	44
3.1.2	Conical Scanning Instruments	51
3.2	Cross Track with Cross Track.....	56
3.3	Conical with Cross Track.....	59
CHAPTER 4: CALIBRATION RESULTS.....		62
4.1	Pre-screening.....	63
4.1.1	SAPHIR	63
4.1.2	MHS.....	66
4.2	Clear Sky and Clear Ocean	67
4.3	Double Differences	69
4.3.1	Cross Track with Cross Track.....	69
4.3.2	Individual Matchups vs Binned Average.....	74
4.3.3	MHS with MHS	79

4.3.4	MHS with AMSU-B	83
4.4	Conical Scanner with Cross Track Scanner	84
4.4.1	GMI with MHS	84
CHAPTER 5: CONCLUSION AND SUMMARY		94
REFERENCES		97

LIST OF FIGURES

Figure 1-1: Microwave spectrum of atmospheric transmissivity for different atmospheres (surface temperatures and integrated water vapor content) [2].	2
Figure 1-2 Illustration of the multiple precipitation measurement satellites which comprise the GPM constellation [1].....	7
Figure 1-3: Coverage provided by a single orbit from the GPM microwave constellation [21]....	8
Figure 2-1: Flowchart for computing inter-calibration double differences (DDs). The flowchart can be applied to any target and reference radiometers for inter-calibration.	13
Figure 2-2: Microwave brightness temperature model.....	14
Figure 2-3: Upward and downward non-polarized atmospheric emissions [2].....	16
Figure 2-4: Cross track scanner mechanism [2].	18
Figure 2-5: Comparison of GDAS and ERA-Interim surface pressure.	21
Figure 2-6: Comparison of GDAS and ERA-Interim Cloud liquid water.....	22
Figure 2-7 Aquarius Sea Surface Salinity Flat Map for Dec 2011 [34].	23
Figure 2-8: Simulated TB emitted from the surface for ocean and fresh water, respectively [36].	24
Figure 2-9: Measured brightness temperature plotted against radiosonde Precipitable Water Vapor for cloud free cases [37].....	25
Figure 2-10: GPS-RO technique demonstration [55].	28
Figure 2-11 Typical locations of COSMIC soundings (green diamonds) compared to existing radiosonde launch sites (red circles) for a day. COSMIC provides about 2,500 sounding profiles every 24 hours [57].	30

Figure 2-12: Contribution profile of a water vapour absorption channel (red) compared to a window channel (blue) [59].	32
Figure 2-13: Cross track scanner antenna beam articulation, geometry and sampling [34].	33
Figure 2-14 SAPHIR and MHS swaths. Blue is MHS swath, and red is SAPHIR and the centre of their swaths is illustrated with magenta and black respectively.	34
Figure 2-15: The collocated 1 degree box for the Time Window ≤ 1 Hour. In the middle of scan or close to the nadir.	35
Figure 2-16. The collocated 1 degree box for the Time Window ≤ 1 Hour at the edge of scan.	35
Figure 2-17: The geometry of earth, satellite EIA, and the top of the atmosphere.	37
Figure 2-18: The geometry of earth, Satellite, satellite EIA.	38
Figure 2-19: Simulated Tbs for the 6 channels of the SAPHIR for the 8 different atmospheric profiles.	40
Figure 3-1: Conical scanning versus cross track scanning satellites [2].	43
Figure 3-2: Atmospheric Transmission at Microwave Wavelengths and ATMS channels [61].	44
Figure 3-3: distribution of channels in SAPHIR instrument [62].	46
Figure 3-4: Imaging geometry of Megha-Tropiques, and SAPHIR [62].	47
Figure 3-5: Functional block diagram of SAPHIR (image credit: CNES)[62].	47
Figure 3-6: Time spans for the TRMM and GPM missions and the polar orbiters in these missions.	50
Figure 3-7 GMI instrument.	52
Figure 3-8 Scan geometry of GMI (NASA) [65].	53
Figure 3-9: Antenna footprint (IFOV) for GMI channels for two consecutive along-scans (credit: NASA) [65].	54

Figure 3-10: Cross track scanning satellite intersecting with another cross track scanning satellite.	58
Figure 3-11: Conical scanning satellite intersecting with cross track scanning satellite.	60
Figure 4-1: Brightness temperature of SAPHIR for the first Channel for an orbit with anomaly (20140724-S034853-E053048).	63
Figure 4-2: EIA reference Used for the filtering SAPHIR data.	65
Figure 4-3: Before and after filtering with new reference.	65
Figure 4-4: EIA reference Used for the filtering MHS data.	66
Figure 4-5 Relation between (top) IWP and $\Delta T_b = T_{b1} - T_{b7}$ and (bottom) IWP and ATMS T_b s from channel 1. The legend shows the data that are considered either clear or cloudy by one of the filters [74].	68
Figure 4-6: Double difference anomaly dependence on earth incidence angle for MHS minus SAPHIR for channel 183.31 ± 1 GHz for various sets of environmental parameters: upper left panel using GDAS, upper right using ERA-I, lower left using GDAS with water vapour profile from SAPHIR retrieved RH, and lower right using ERA-I plus retrieved RH.	70
Figure 4-7: Double difference anomaly dependence on earth incidence angle for MHS minus SAPHIR for channel 183.31 ± 3 GHz for various sets of environmental parameters: upper left panel using GDAS, upper right using ERA-I, lower left using GDAS with water vapour profile from SAPHIR retrieved RH, and lower right using ERA-I plus retrieved RH.	71
Figure 4-8: Double difference anomaly dependence on earth incidence angle for MHS minus SAPHIR for channel 183.31 ± 7 GHz for various sets of environmental parameters: upper left panel using GDAS, upper right using ERA-I, lower left using GDAS with water vapour profile from SAPHIR retrieved RH, and lower right using ERA-I plus retrieved RH.	72

Figure 4-9: Double differences variation with temperature for MHS-SAPHIR with using GDAS, ERA-I, and retrieved RH. The number of data counts at each point has been presented with solid green line and diamond shape.....	76
Figure 4-10: Double differences variation with temperature for MHS-SAPHIR with using GDAS, ERA-I, and GPS-RO profiles. The number of data counts at each point has been presented with solid green line and diamond shape.....	77
Figure 4-11: Double differences variation with temperature for ATMS-SAPHIR with using GDAS, ERA-I, and retrieved RH. The number of data counts at each point has been presented with solid green line and diamond shape.....	78
Figure 4-12: Double differences variation with temperature for ATMS-MHS with using GDAS, ERA-I, and retrieved RH. The number of data counts at each point has been presented with solid green line and diamond shape.....	79
Figure 4-13: Single difference anomaly dependence on earth incidence angle for MHS on board of MetOp-B minus MHS on board of MetOp-A for the corresponding five channels, and number of counts for each pixels.	80
Figure 4-14: Double difference anomaly dependence on earth incidence angle for MHS on board of MetOp-B minus MHS on board of MetOp-A for the corresponding five channels, and number of counts for each pixels.	81
Figure 4-15: MetOp-B – MetOp-A biases changes with latitude.....	82
Figure 4-16: Double difference anomaly dependence on earth incidence angle for AMSU-B on board of NOAA17 minus MHS on board of MetOp-A for the corresponding five channels, and number of counts for each pixels.....	84

Figure 4-17: Double difference dependence on earth incidence angle for MHS on board of MetOp-B minus GMI for the corresponding five channels.	86
Figure 4-18 :Double difference dependence on the earth latitude for MHS on board of MetOp-B minus GMI for the corresponding five channels.	87
Figure 4-19: Observed brightness temperature comparisons for SAPHIR and SSMIS for the 183±3 GHz channel for F16, F17 and F18 [66].....	88
Figure 4-20: Double Differences values for F18 for six months [66].	89
Figure 4-21: Double differences dependence on Incidence angle for GMI-SAPHIR with using GDAS and ERA.....	90
Figure 4-22: Double differences variation with temperature for GMI-SAPHIR with using GDAS and ERA.....	91
Figure 4-23: variation of biases with time for 2014 [79].....	92

LIST OF TABLES

Table 2-1: simulated brightness temperatures for SAPHIR instrument for Nadir and 6.5 degree.	39
Table 2-2: run time, and number of samples using different resolutions.	41
Table 2-3: simulated brightness temperatures using different resolutions.	41
Table 3-1 ATMS Radiometric and Channel Characteristics [61].....	45
Table 3-2 SAPHIR Radiometric and Channel Characteristics.	48
Table 3-3 MHS Radiometric and Channel Characteristics.....	49
Table 3-4 Specifications of AMSU-B channels [64].....	50
Table 3-5 GPM GMI Channel Specifications [65].	54
Table 3-6: F18 SSMIS Sensor Characteristics (similar to F16, just the first 5 channels are Horizontal) [65].	56
Table 3-7: Sounder channels pairing.	61
Table 4-2: biases between SAPHIR and MHS using the binned average and IFOV matchups methods.	75
Table 4-3: biases between MHS sensors for 2015.....	82
Table 4-4: Biases between MHS on MetOp-A and AMSU-B on board of NOAA-17 for 2009..	84
Table 4-5: biases between GMI and MHS sensors for 2015.	87
Table 4-6: Average Double Differences values for different satellites for both Binned Average and IFOV Match-ups methods [66].	89
Table 4-7: Double differences using Rosencranz, MonoRTM with GDAS and ERA-I [79].....	93

CHAPTER 1: INTRODUCTION

In the study of climate and global water cycle, precipitation is a major factor since it is not homogenous and changes with time, making the retrieval of precipitation a challenging task. The measuring the precipitation is done with ground based and space-borne instruments. Ground based instruments are sparse, they can look at point sources, and measure the precipitation at a specific location, but there are not enough gauges around the world, and we could gather all the gauges around the world, they would fit into an area about the size of two basketball courts. But space-borne measurements enable us to provide a much more global picture [1].

Monitoring the precipitation using the Space-borne Instruments has been done during the past several decades and the methods are improving continuously. The Precipitation Measurement Mission's (PMM) program supports scientific research, algorithm development, and ground-based validation activities for the precipitation measurements [1].

In order to be able to obtain global precipitation measurements a satellite constellation is required to provide the necessary spatial/temporal sampling.

1.1 Principle of Radiometric Measurements

The earth's surface, ocean, and atmosphere emit and absorb Microwave (MW) radiation. The amount of radiation a microwave radiometer receives is called brightness temperature. Several atmospheric gases provide specific absorption features which can be used to derive the

information about the abundance and structure of atmospheric components. For example, the oxygen absorption line around 60 GHz is used to derive temperature profiles, or the water vapor absorption line around 22.235 GHz, is used to observe the vertical profile of humidity. Other significant absorption lines are found at 118.75 GHz for oxygen absorption and at 183.31GHz for water vapor absorption, used for water vapor profiling. Figure 1-1 shows the microwave spectrum of atmospheric transmissivity for different atmospheres [2]. The black lines show the transmissivity for a standard atmosphere at mid latitude, the blue line presents the transmissivity in polar region with dry atmosphere and cold surface temperature, and the red line represents the transmissivity in tropical regions with high humidity and high surface temperature.

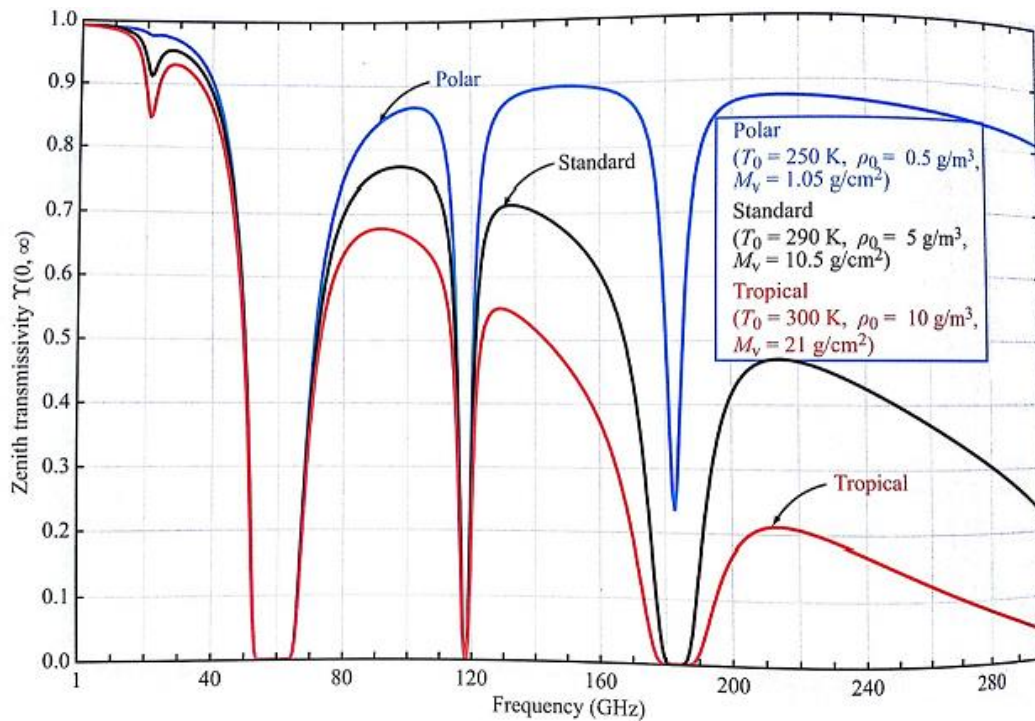


Figure 1-1: Microwave spectrum of atmospheric transmissivity for different atmospheres (surface temperatures and integrated water vapor content) [2].

In addition, there are also contributions by hydrometeors like liquid drops and ice particles. Liquid water emission increases with frequency; hence, measuring at two frequencies, typically one close to the water absorption line at 22.235 GHz and one in the nearby window region dominated by liquid absorption provides information on both the columnar amount of water vapor and the columnar amount of liquid water separately [3].

Also, larger rain drops as well as larger frozen hydrometeors like snow and hail, scatter microwave radiation especially at frequencies higher than 90 GHz. These scattering effects can be used to distinguish between rain and cloud water content exploiting polarized measurements [4], but also to constrain the columnar amount of snow and ice particles from space and from the ground [5, 6]. Therefore, in addition to absorption bands, frequencies in window bands are used in microwave remote sensing as well. Moreover, microwave radiometers built and launched by different space agencies have widely varying specifications, which should be considered in the retrievals of precipitations.

1.2 Inter-calibration Description

All physical measurements are subject to random and systematic errors, and satellite microwave radiance measurements are no exception. These errors can be classified into radiometric and geometric errors [7]. There are a number of methods to quantify the radiometric errors in microwave measurements, such as validation using airborne observations [8] and inter-calibration with similar instruments [9], which is our focus.

Radiometric inter-calibration begins with prescreening of the Tb's for each single sensor for self-consistency to identify and correct the systematic biases across the scan or along the orbit path. Brightness temperature images of the surface observations are the most obvious test, and

one- and two-dimensional histograms allow us to examine a large volume of data to identify anomalous outlier Tb's. Every sensor, particularly one in the early stages of analysis, will have outliers.

To provide unified estimates of precipitation, from microwave radiometers built and launched by different space agencies with widely varying specifications and capabilities, requires that the input brightness temperatures (Tb) be physically-consistent between sensors. This means that differences in the observed Tb between sensors should agree with the expected differences based on radiative transfer model simulations that account for variations in the observing frequencies, channel bandwidths, view angles, etc. Properly accounting for sensor differences is critical to producing consistent precipitation estimates between radiometers and the only way to ensure that observed changes in precipitation are real and not the result of sensor calibration issues.

Previous work focused on inter-calibration of nearly identical copies of the Special Sensor Microwave/Imager (SSM/I) instruments on board the Defense Meteorological Satellite Program (DMSP) spacecraft [10]. The following efforts have focused on extending the DMSP data record [11-13], including latest more efficient sensors for robust long-term data records [14-16], and analyzing calibration differences with cross-track water vapor sounding radiometers [9, 17]

The PMM inter-satellite radiometric calibration (XCAL) working group is a vital part of the PMM science team, which supports the passive microwave precipitation retrieval algorithm team and which ensures a high quality Tb product to the science team at large. Established in 2007, this team presently consists of four principal university subgroups, namely: University of Central Florida, University of Michigan, Colorado State University, and University of Texas A&M, who collaborate in the inter-satellite radiometric calibration of the GPM constellation microwave radiometers. Because the deliverables of this working group are derived on a consensus basis, it

is necessary to have several investigators working independently and comparing their results in frequent workshops to produce acceptable results.

As a charter member of the PMM X-CAL working group, the Central Florida Remote Sensing Lab (CFRSL) has developed an unique approach to perform radiometric inter-calibration between satellite radiometers. When two satellite radiometers simultaneously view the same earth scene, generally they have similar, but not identical, observation parameters such as frequency, polarization and viewing angle. To accommodate these differences, we have developed a robust brightness temperature normalization algorithm, which predicts the T_b observations from one satellite, based on the observations of another [18]. Based upon our analysis of the dynamic nature of atmosphere, ocean and land parameters, this restricts inter-comparisons to time windows of ± 1 hr and spatial collocations of 100 km.

1.3 Global Precipitation Measurement Mission

The Global Precipitation Measurement (GPM) mission uses both passive and active microwave instruments in order to measure the precipitation globally with high precision. This mission consists of nine satellites, provided by partnership of United States, Japan, India and Europe, and it is the follow-on mission of Tropical Rainfall Measuring Mission (TRMM). This joint effort between the Japan Aerospace Exploration Agency (JAXA) and the National Aeronautics and Space Administration (NASA), to measure the rain over the tropics, was launched on November 27, 1997 by JAXA from Japan. TRMM used both passive (PWM) and active microwave measurements. For the PWM measurements, the sensor was the TRMM Microwave Imager (TMI) and for the active measurements the sensor was the Precipitation Radar (PR). This

mission provided over 17 years of valuable precipitation observations that ended on April 2015 [1, 19].

Since the GPM launch in February 2014, a new satellite constellation continues and improves global precipitation measurements. In order to have consistent measurements, there is a need to reduce errors in global rainfall estimates associated with temporal/spatial sampling by using this constellation of satellites. The XCAL goal is to remove all the instrumental effects like gain drifts, and perform periodic, on orbit radiometric calibrations in the constellation.

Figure 1-2 presents the satellites in the GPM constellation that comprise an international effort to measure rain and snow globally every three hours. The goal is to advance space-borne precipitations measurements, improving the knowledge of freshwater availability and water cycle and its link to climate change, providing new insights into large-scale atmospheric processes like storm structures, improving forecasting abilities for natural hazards like floods and droughts, and improving agricultural crop forecasting [20].

In this constellation, GPM Core Observatory serves as a transfer standard for the brightness temperature calibration. Like TRMM, the GPM core observatory carries both active and passive remote sensors; namely, the GPM Microwave Imager (GMI) and the Dual-Frequency Precipitation Radar (DPR), but both instruments are more capable than TRMM. For example, the diameter of antenna in the GMI is twice that of TMI and the precipitation radar is dual-frequency which can provide improved three dimensional distributions of precipitation. GMI is a conical scanner, and it has 13 channels from 10 GHz to 183 GHz.

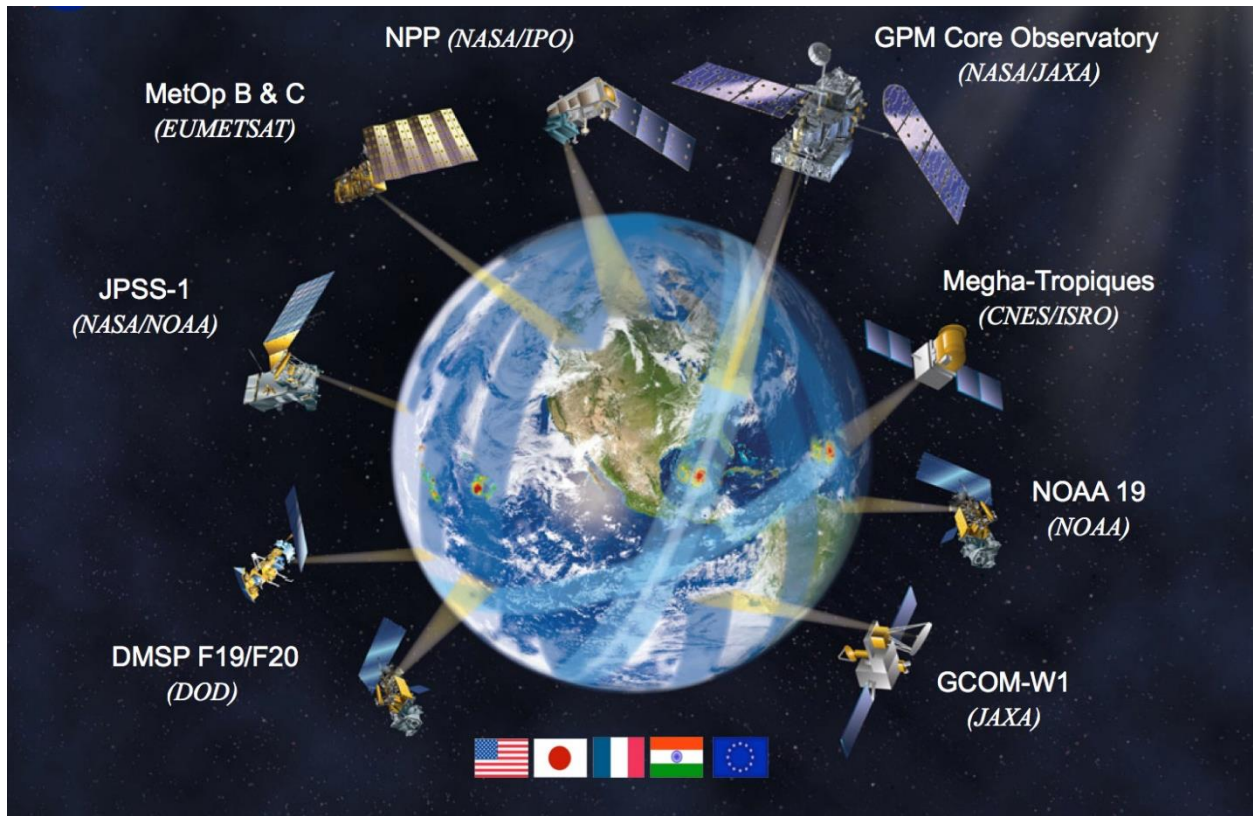


Figure 1-2 Illustration of the multiple precipitation measurement satellites which comprise the GPM constellation [1].

A snapshot of the spatial coverage (for a single orbit for a typical day) provided by the conically-scanning and the cross-track scanning microwave radiometers in the GPM constellation [21] is shown in Fig. 1-3. For these satellite orbits, the low inclination orbits of the TRMM and GPM satellites results in regular daily intersect with all the sun-synchronous polar-orbiting spacecraft. Also, because of their wide swath and the inclination of the polar orbits that provide high latitudes coverage, these radiometers provide the majority of desired 3-hourly global sampling requirements for the GPM constellation [19], [21].

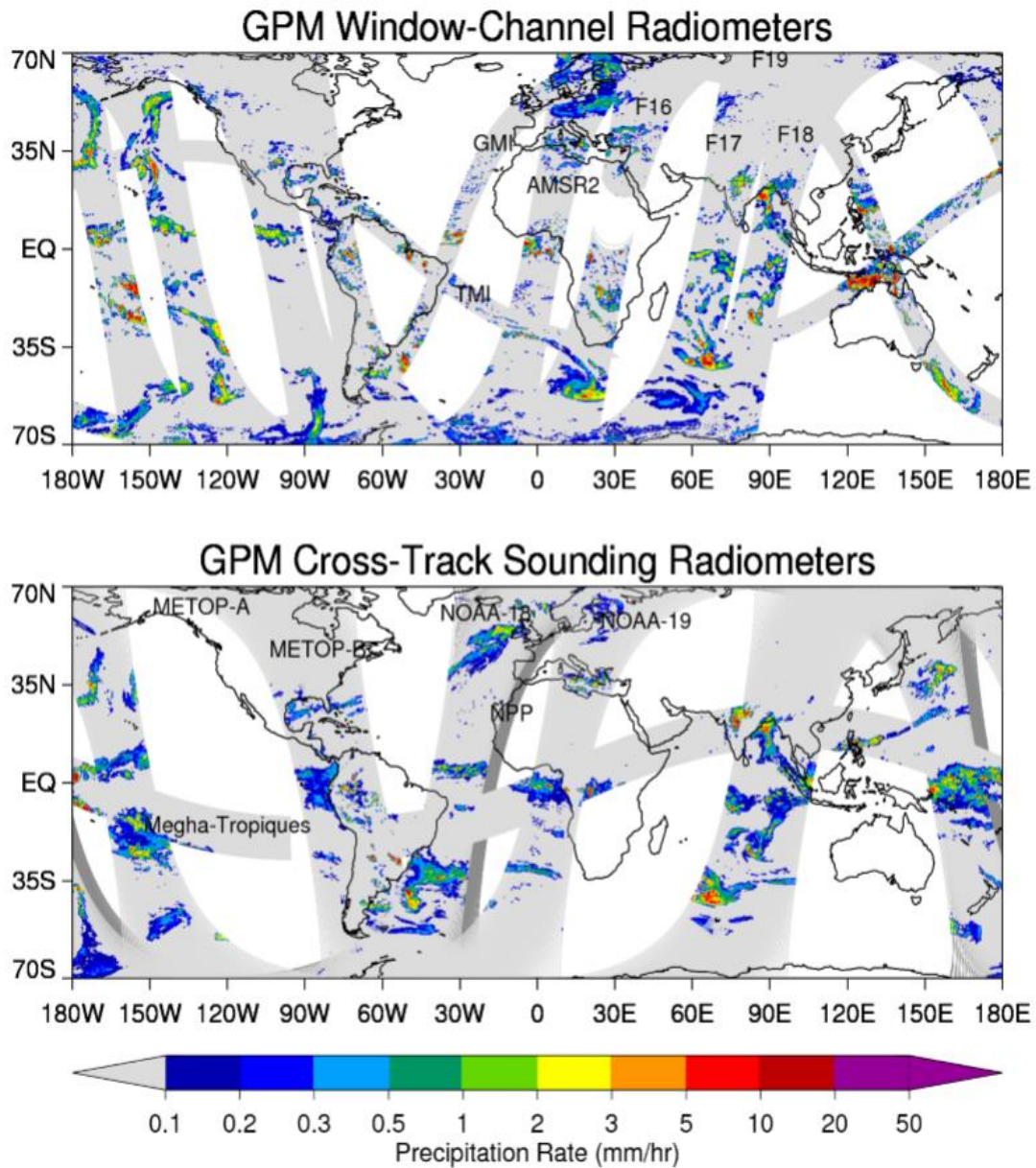


Figure 1-3: Coverage provided by a single orbit from the GPM microwave constellation [21].

The inter-calibration (XCAL) of microwave radiometer channels using GMI is a challenging task. In the GPM constellation there is a combination of different sensors, and the goal is to

make consistent brightness temperature measurements between the constellation members. In this dissertation, the main focus is on the radiometric calibration of higher frequency channels in the GPM constellation. In the next generations of rain retrievals algorithms which are more precise, the importance of higher frequencies is increasing. Inter-calibration channels of conical scanning imagers (or channels lower than 89 GHz) have been done successfully over years, but the calibration of high frequencies channels (higher than 89 GHz) or sounders is more challenging. For these calibrations, there are combinations of different type of scanning methods, and the radiative transfer atmospheric and surface emissivity models are less well defined, which makes the calibration of these channels more challenging.

1.4 Dissertation Objective and Overview

The purpose of this dissertation is to provide a robust radiometric calibration approach for sounder microwave radiometers in the GPM constellation. This addresses the challenges in the calibration of both cross-track and conical scanner geometries by characterizing scan dependency, investigation of the calibration dependence on brightness temperature, and analyzing calibration variability and dependence on geometry and temporal variations. Also, issues in the inter-calibration of high frequency channels have been identified and mitigation strategies are evaluated. Inter-Calibration methods are developed and applied to radiometers on both cross-track scanning and conical scanning instruments within the GPM constellation.

This dissertation is organized as follows: Chapter 2 discusses the Double Difference Technique, the radiative transfer model, and environmental parameters used (especially the importance of the relative humidity component); Chapter 3 describes different type of sensors and calibration

techniques used; Chapter 4 presents the calibration results for the both cross-tracking and conical scanning geometries, and Chapter 5 summarizes this dissertation findings.

CHAPTER 2: DOUBLE DIFFERENCES TECHNIQUE

There are several methods for inter-satellite calibration, which have been described in previous publications [16, 22, 23]; however for the PMM, the approach requires that all sensors be calibrated against a single reference sensor, and as discussed above, for the current GPM constellation, this is the GMI radiometer. Because the radiances for millimeter sounders come primarily from the atmosphere, there are different considerations than those used for the XCAL of the lower frequency imaging channels, which will be discussed below.

This first consideration for sounder XCAL is the spatial/temporal collocation. The objective is to obtain a large number (tens to hundred thousands) of high quality observations for comparisons. Also, following the imager approach, the emphasis is on “high quality”, which means that clear sky and calm ocean scenes are desirable, where there is large-scale spatial homogeneity of environmental conditions. Excluding precipitation, the spatial scales of atmospheric parameters (pressure, temperature and humidity) are large (100’s of km) and slowly varying in time (hours) over these scales. Therefore, the standard $1^\circ \times 1^\circ$ latitude/longitude boxes and ± 1 hr windows used for imager channels are acceptable for sounders, with conservative filtering. However, sounder XCAL is different in that there are two different scan configurations (cross-track and conical scan) that must be accommodated, and these are significant because they represent different slant paths through the atmosphere.

Often, GMI and cross-track scanners have near-identical viewing geometries (incidence angles and atmospheric slant paths) whereby direct Tb comparisons are possible, but for the majority of coincident observations, these conditions do not occur. For these cases, a

transformation of Tb's to a common basis is required before inter-comparisons can be made. For sounder XCAL, the approach is to use the double difference (DD) technique [22], which was previously successfully applied for imager channel calibration, as shown in Fig. 2-1. However, as will be discussed in Chapter 3, there are restrictions that must be applied for the different scan configurations (cross-track to cross-track and conical to cross-track). Regardless, the purpose of this technique is to find a radiometric calibration bias from one radiometer to another. Having two independent radiometers (e.g., GMI and Sounder), allow us to obtain the difference between the observed brightness temperatures, which is called the observed single difference (OSD). Next, using a theoretical radiative transfer model, the modeled Tb values for the two instruments are subtracted to produce the modeled single differences (MSD), which is the expected difference between two sensors without calibration biases. Then, the instrument calibration bias is defined as the difference of the single differences (double difference, DD) that is calculated by subtracting the MSD from OSD as:

$$DD = (Tb_Reference_obs - Tb_Target_obs) - (Tb_Reference_mod - Tb_Target_mod) \quad (2-1)$$

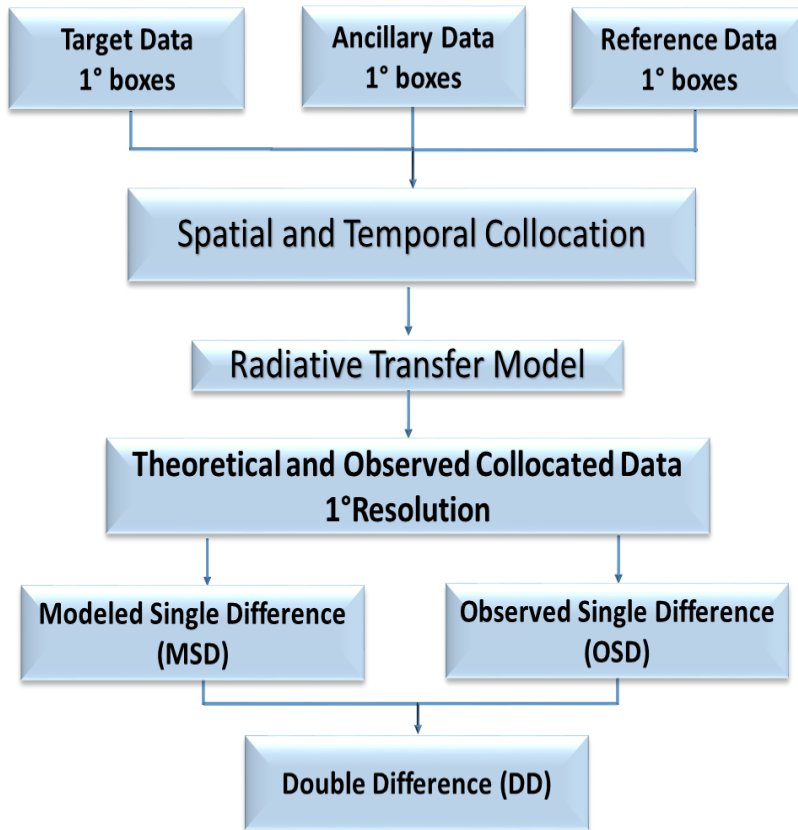


Figure 2-1: Flowchart for computing inter-calibration double differences (DDs). The flowchart can be applied to any target and reference radiometers for inter-calibration.

2.1 Radiative Transfer Model

The second consideration for sounder XCAL is the radiative transfer model used to calculate theoretical brightness temperatures. For a satellite microwave radiometer, there are three components of the measured brightness temperature (powers) that are scalars at the receiving antenna, as illustrated in Fig. 2-2. The linear polarized components (vertical and horizontal) are separated by the receiving antenna, namely: upwelling atmospheric brightness temperature (non-

polarized), downwelling atmospheric brightness temperature reflected upward at the ocean surface (polarized) and the brightness temperature due to sea surface emission (polarized).

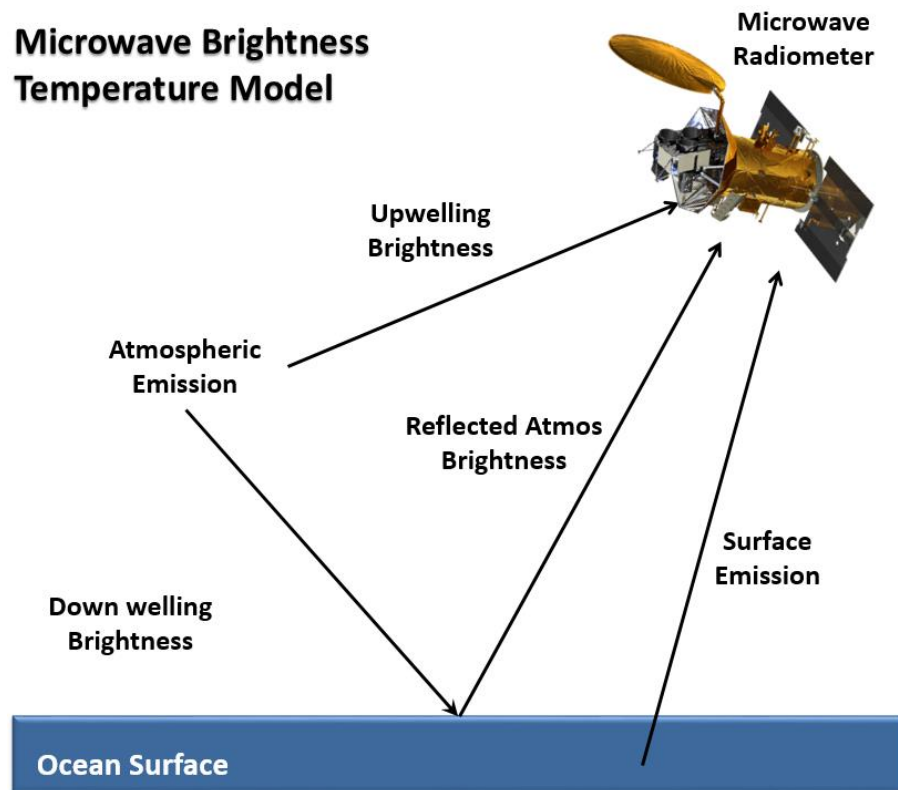


Figure 2-2: Microwave brightness temperature model.

In theory, the linear polarized measured brightness temperature by a satellite is given by the following equation:

$$T_b = T_{up} + \tau \varepsilon T_s + \tau (1 - \varepsilon) T_{down} (1 + \Omega_{scat}) + \tau^2 (1 - \varepsilon) T_{bc} \quad (2-2)$$

Where: T_{up} is the upwelling (non-polarized) atmospheric brightness temperature,

τ is the total atmospheric transmittance,

ε is the polarized surface emissivity,

T_s is sea surface temperature,

$(1 - \varepsilon)$ is the polarized specular power reflection coefficient,

T_{down} is downwelling (non-polarized) brightness temperature,

Ω_{scat} is the diffuse power scattering coefficient due to wind-roughed sea surface,

and,

T_{bc} is the cosmic background (non-polarized) brightness temperature.

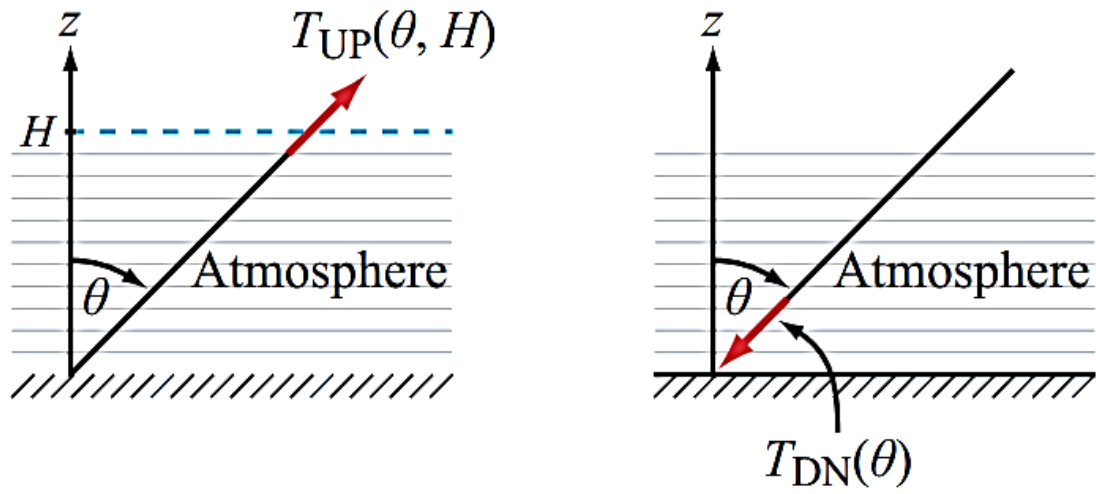


Figure 2-3: Upward and downward non-polarized atmospheric emissions [2].

T_{up} , and T_{down} are derived from the following equations:

$$T_{up}(\theta, TOA) = \sec(\theta) \int_0^{TOA} k_a(z') T(z') e^{-\tau(z', TOA)} dz' \quad (2-3)$$

$$T_{down}(\theta) = \sec(\theta) \int_{TOA}^0 k_a(z') T(z') e^{-\tau(0, z')} dz' \quad (2-4)$$

where k_a is the absorption coefficient due to oxygen, nitrogen, water vapor and cloud liquid water, and T is the atmospheric temperature profile. The nominal value for T_{bc} is 2.7 k, but at high frequencies it is necessary to calculate the T_{bc} with the exact Planck law [24]. This temperature can be calculated from the following equation:

$$T_{bc} = \frac{hv}{2k} \cdot \left(\frac{e^{\frac{hv}{kT_{c0}}} + 1}{e^{\frac{hv}{kT_{c0}}} - 1} \right) \quad (2-5)$$

where T_{c0} is the physical cold space temperature, and it is equal to $T_{c0} = 2.73 \text{ k}$, v is the frequency of the radiation, $h = 6.626176 \cdot 10^{-34} \text{ Joule.s}$ is Planck's constant and $k = 1.38066 \frac{\text{Joule}}{\text{Kelvin}}$ is Boltzmann's constant [25].

Concerning the surface emissivity, our knowledge over land is imperfect because of the heterogeneous nature; therefore, for this research, only the observations over ocean with two different models have been used [26, 27]. For the atmosphere, Sounders operate at frequencies $> \sim 90 \text{ GHz}$, in the vicinity of a strong oxygen line at 118 GHz and a water vapor absorption line at 183 GHz channels. For oxygen, we use the model of Liebe [28], and for water vapor, we use the model of Rosenkranz [29].

2.2 Mixed Polarization

Concerning the brightness temperature measurement geometry, there are major differences between cross track scanners and conical scanners. as illustrated in Fig. 2-4. In conical scanning, the antenna is pointed off-nadir at a fixed angle of incidence and rotated about the vertical axis, which results in a fixed earth incidence angle (EIA), fixed vertical and horizontal beam polarization, and a constant instantaneous field of view (IFOV) along a circular path on the surface. On the other hand, for cross track scanners, we have a fixed horn and a rotating flat mirror, which results in a variable EIA, a rotating beam polarization, and a variable IFOV for each scan position.

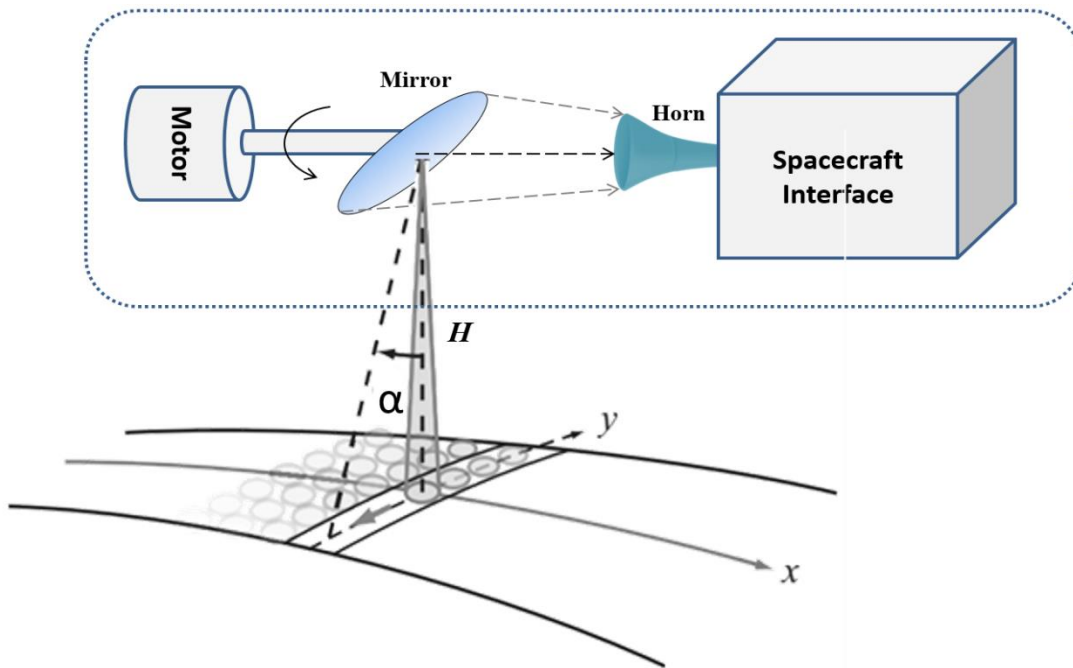


Figure 2-4: Cross track scanner mechanism [2].

Therefore, for the cross track scanner, because of the rotating linear polarization of the antenna beam with scan angle, it is necessary to adjust the polarization in the RTM to match the measured Tb. To accomplish this, the corresponding ocean surface emissivity in the cross track scanners is a result of combination of vertical and horizontal components of surface emissivity that must be considered in the RTM Model. The modeled brightness temperature for the quasi-horizontal is calculated as:

$$\varepsilon_{Qh} = \varepsilon_h \cos^2(\alpha) + \varepsilon_v \sin^2(\alpha) \quad (2-6)$$

where ε_h is the horizontal surface emissivity and ε_v is the vertical component.

The quasi-vertical the emissivity is calculated as:

$$\varepsilon_{Qv} = \varepsilon_v \cos^2(\alpha) + \varepsilon_h \sin^2(\alpha) \quad (2-7)$$

where the scan angle, α , is calculated as:

$$\alpha = \sin^{-1}\left(\frac{R_e}{R_e + H} * \sin(\pi - EIA)\right) \quad (2-8)$$

$R_e = 6,371 \text{ km}$ is Earth radius, and H is the satellite altitude.

2.3 RTM Environmental Parameters

In order to simulate the measured brightness temperature, the RTM requires environmental parameter inputs such as atmospheric temperature and humidity profiles, and ocean surface temperature and wind speed. The environmental data that have been used in this paper are the NOAA Global Data Assimilation System (GDAS) [30], and the European Center for Medium Range Weather Forecasting Interim Reanalysis (ERA-I) [31] datasets, and sea surface salinity.

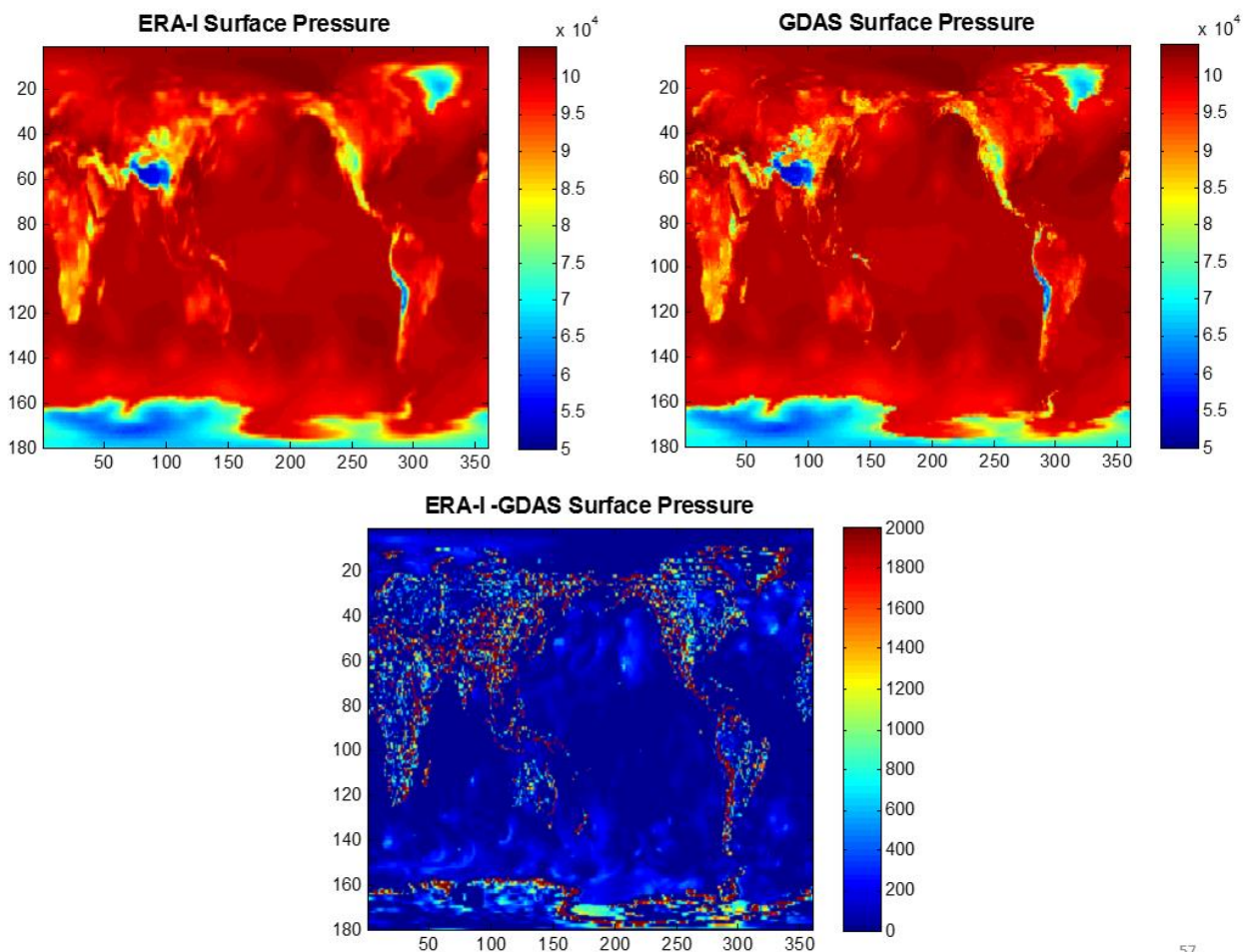
2.3.1 *GDAS Data*

The National Centers for Environmental Prediction's (NCEP) [32] Global Data Assimilation System (GDAS) is a global analysis of the Earth's atmosphere and ocean surface generated every 6 hours for 00Z, 06Z, 12Z, and 18Z. The analysis incorporates a variety of meteorological and oceanographic measurements from buoys, ships, planes, radiosondes, weather radars, and earth orbiting satellites. Atmospheric parameter profiles have 21 levels defined by atmosphere pressure between sea-level and 100 mbar.

2.3.2 *ERA-Interim Data*

ERA-Interim is a global atmospheric reanalysis produced by the European Center for Medium-Range Weather Forecast (ECMWF). The spatial resolution of the data set is similar to GDAS, and it is generated every 6 hours for 00Z, 06Z, 12Z, and 18Z. There are 29 pressure levels for ERA-I between 1000 and 50 mbar. Because the GDAS and ERA-Interim datasets are generated using independent models and often different input datasets, their results are different. Below (Fig. 2-5 and 2-6), we compare an example of surface pressure fields and integrated cloud liquid

water parameters for these models. Although, both datasets agree in most of the points, there are many instances with significant discrepancies as well. Because they are different, we use both datasets here and compare the results. Based upon the XCAL DD for imager radiometers, the resulting biases should be very similar.



57

Figure 2-5: Comparison of GDAS and ERA-Interim surface pressure.

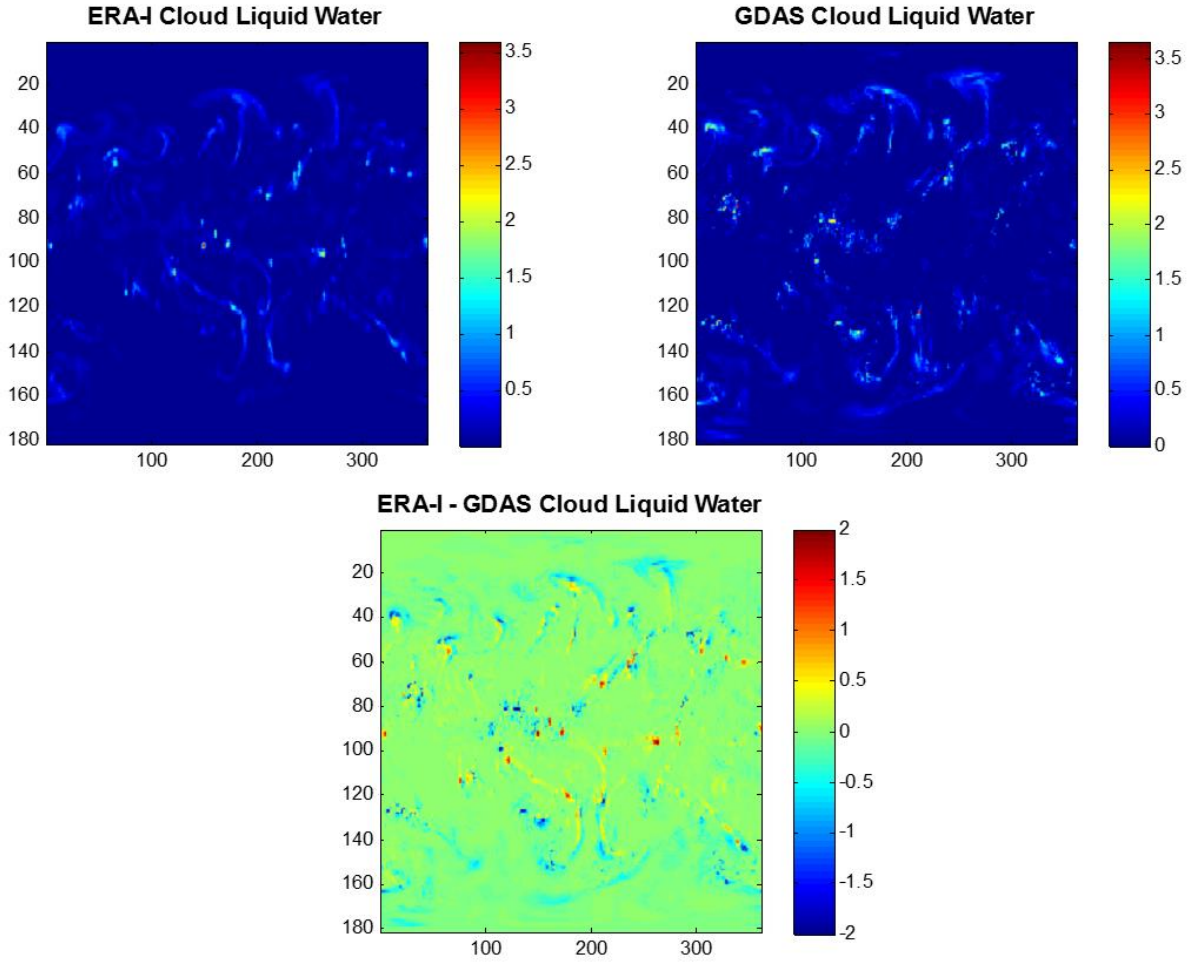


Figure 2-6: Comparison of GDAS and ERA-Interim Cloud liquid water.

2.3.3 Salinity Data

Salinity values used in the RTM are monthly averages from National Oceanographic Data Center World Ocean Atlas (NODC WOA) salinity [33], and Fig. 2-7 shows the sea surface salinity map for Dec 2011, which has salinity changing from 30 Practical Salinity Unit (PSU) to 38, with the average value of around 34 PSU.

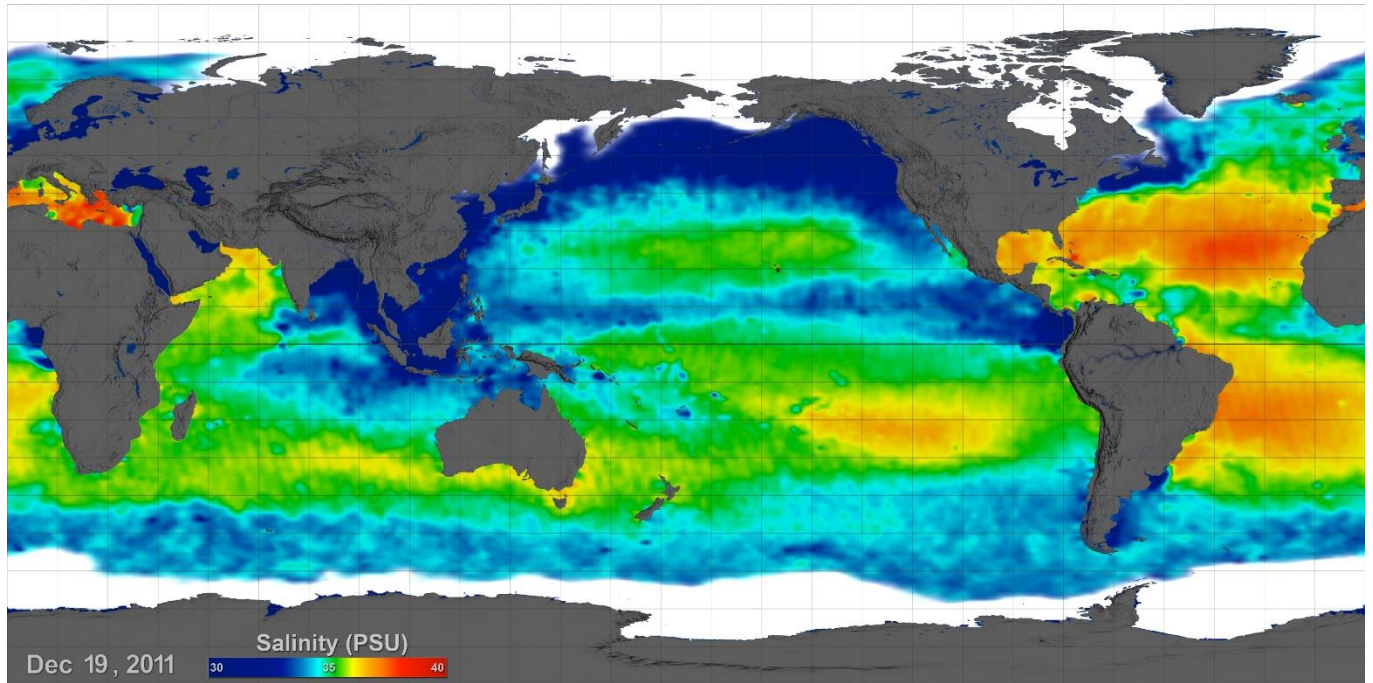


Figure 2-7 Aquarius Sea Surface Salinity Flat Map for Dec 2011 [34].

The RTM simulated Tb shown in Fig. 2-8, demonstrates that changes in sea surface salinity do not affect the calculated brightness temperature for frequencies higher than about 5 GHz. For these calculations, fresh (0 psu) and sea water (34 psu) were input to the ocean surface emissivity model developed by Elsasser [27, 35] for EIA equal to 53 degrees; water temperature 17 Celsius; and wind speed is 6 m/s [36]. Thus, in this research, focusing on high frequencies, we ignore the effect of changes in salinity.

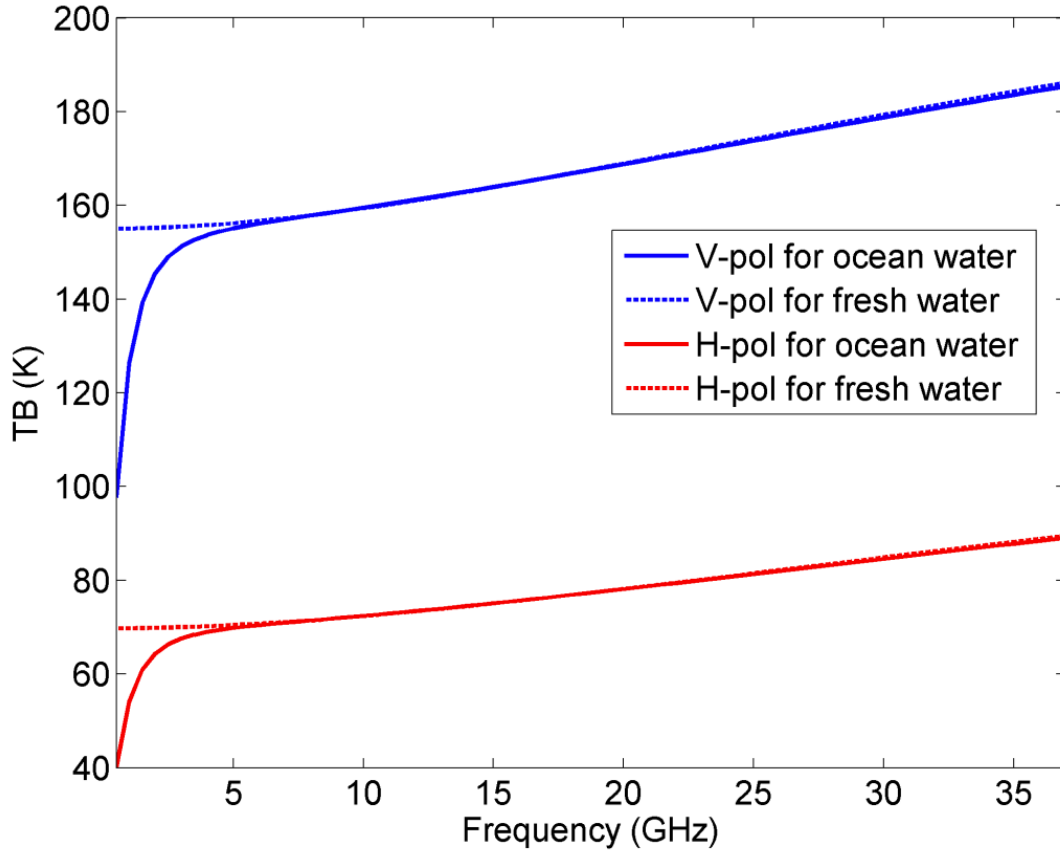


Figure 2-8: Simulated TB emitted from the surface for ocean and fresh water, respectively [36].

2.4 Relative Humidity

Of the environmental parameters needed to model the brightness temperatures, humidity is one of the most crucial ones, and it is difficult to estimate. Radiometer channels at both 23.8 GHz and 183.31 GHz have been used to remotely sense atmospheric water vapor. The resonant line at 22.235 GHz is used to measure total perceptible water (integrated water vapor); but since this channel has low atmospheric opacity, it is not suitable for the estimation of humidity vertical

profile. In the other hand, the 183.31 GHz line has high atmospheric opacity, and it is used for retrieval of water vapor profiles. Figure 2-9 shows the measured brightness temperature plotted against radiosonde Precipitable Water Vapor for cloud free cases for the 23 and 183 GHz channels [37]. From these plots, it is obvious that these frequencies are highly sensitive to the precipitable water vapor.

There are several algorithms to retrieve relative humidity from 183 GHz channels [38-41], here we use the relative humidity derived from SAPHIR data using the method presented by Sivira et al. 2015 [41].

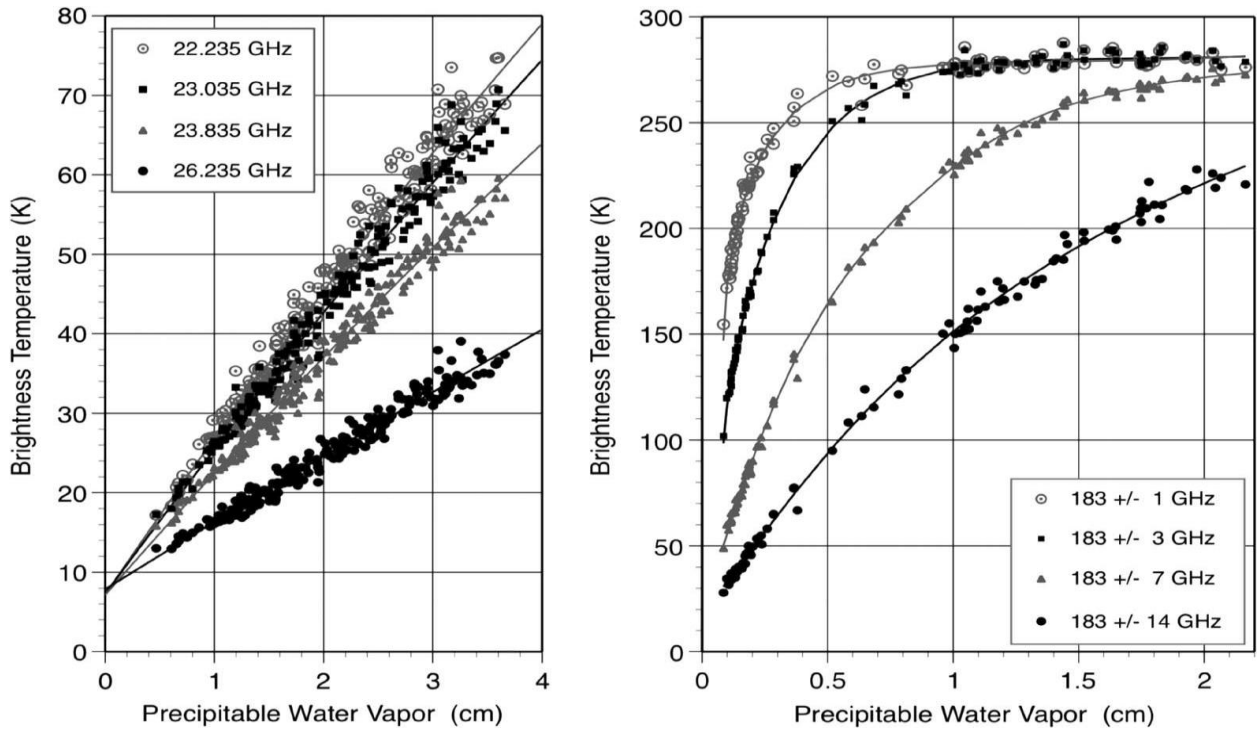


Figure 2-9: Measured brightness temperature plotted against radiosonde Precipitable Water Vapor for cloud free cases [37].

2.5 Relative Humidity Derived From SAPHIR

This product using the six channels of SAPHIR decomposes the troposphere into 6 layers: 100-200hPa, 250-350hPa, 400-600hPa, 650-700hPa, 750-800hPa and 850-950hPa. The retrieval scheme for "Atmospheric Relative humidity Profile Including the Analysis of confidence intervals" (ARPIA) encompasses the estimation of the mean RH as well as its standard deviation interpreted as the 1-sigma confidence interval [42]. ARPIA is performed for cloud-free and cloudy conditions and for oceanic and continental scenes. The only limit is for icy layers on top of convective clouds and for precipitating conditions, which are withdrawn using the Hong et al [43] threshold method adapted for SAPHIR channels [41]. We have used this data-set provided by the French scientific ground segment at the ICARE Data and Service Center.

To use this RH product, it is interpolated into the 21 layers for GDAS and 29 layers for ERA. For this purpose, the RH values in each pressure layer, is assumed to be the average value at the center of each layer, which is interpolated into the fixed pressure layers in the GDAS and ERA models.

2.6 GPS Radio Occultation

History: The idea of radio occultation (RO) was developed in 1964 for the study of planetary ionosphere [44], and since 1975, this technique has been applied to study the Earth's atmosphere using communications satellites [45]. The first earth-observing RO mission, the Global Positioning System (GPS) Meteorology (GPS/MET) experiment, was launched In 1995 [46]. GPS/MET produced roughly 100–150 measurements per day up until 1997. In 2001, the CHALLENGING Minisatellite Payload (CHAMP) mission [47] and the Argentinian Satelitede Aplicaciones Cientificas-C (SAC-C) became operational, and produced roughly 150 and 100

measurements per day, respectively. SAC-C profiles are available through most of 2002, while CHAMP is still operational. In 2006 the Constellation Observing System for Meteorology, Ionosphere and Climate (COSMIC) instrument array [48], a constellation of six satellites was launched, and currently produces about 1500 occultations daily across the globe. Ware et al. [46] and Kursinski et al. [49] examined profiles from GPS/MET and found RO to be quite accurate (within 1 K) for measuring atmospheric temperatures at altitudes of 5–15 km. Hajj et al. [50] followed up on their work, presenting a detailed characterization of the precision of RO data using CHAMP and SAC-C. They found the accuracy of RO to be within 0.5 K between 5 and 20 km [51].

GPS RO Technique: Global Positioning System (GPS) radio occultation is a creative technique for monitoring the global atmosphere that incorporates a variety of instruments, including high altitude GPS satellites and low earth orbiting (LEO) GPS receivers [49, 52]. The GPS transmitting satellites send radio signals through the limb of the earth's atmosphere to receiving satellites as illustrated in Fig. 2-10.

The atmosphere refracts the radio signals, delaying their arrival at the LEO receivers. By assuming local spherical symmetry, the phase delays can be used to determine vertical profiles of bending angle and refractivity [25], which can then be used to derive profiles of atmospheric temperature and humidity, although additional external temperature data are needed to distinguish between the effects of the two. Since RO involves the measurement of an elementary parameter – essentially a time delay – it is not susceptible to instrument drift, and RO satellites are self-calibrating [53]. RO provides a global measurement with a fairly uniform distribution, in all weather conditions, down to roughly the lowest 1–2 km of the atmosphere, where

atmospheric ducting, ray multipath, and low signal-to-noise ratios tend to make accurate retrievals very difficult to retrieve [54].

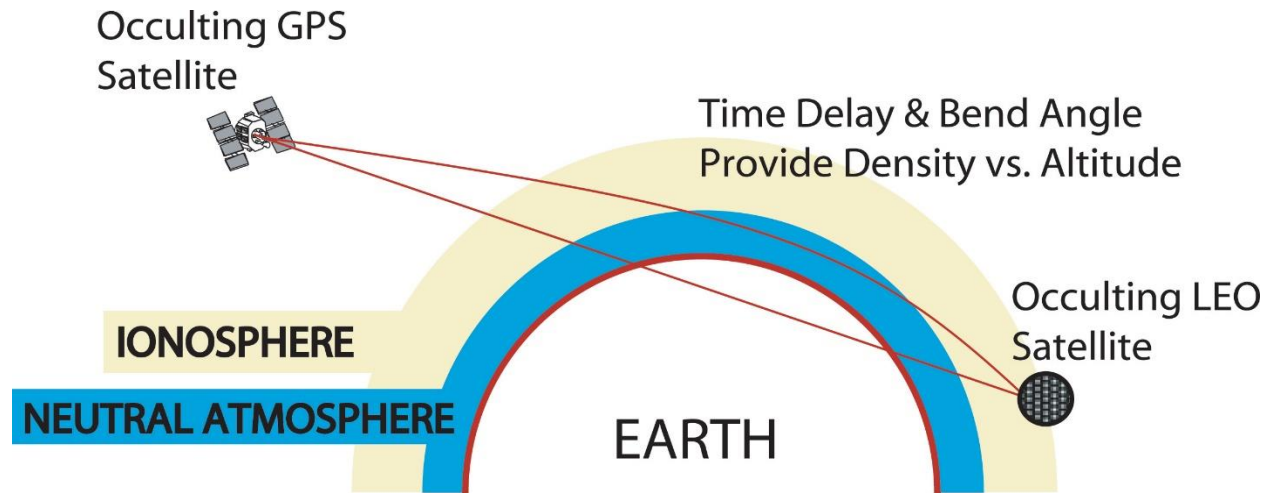


Figure 2-10: GPS-RO technique demonstration [55].

When utilizing RO data, it should be remembered that bending angles at a given point in the atmosphere are calculated from integrals over a ± 300 km occultation path [25]. This calculation involves the assumption that refractivity gradients are a function of height only, and fortunately, errors resulting from this assumption are generally small [56].

2.6.1 Advantages and Disadvantages of GPS-RO

Most measurements are based on physical devices (instruments) that are not perfect and often deteriorate with time i.e., they drift and need to be recalibrated. On the other hand, the Radio

Occultation technique is based on time delays, traceable to an absolute International System of Units (SI) base unit, and there is no need for recalibration.

Although the atmospheric profiles retrieved from the GPS-RO data are very accurate, there is a problem associated with the measurement density. Its spatial and temporal resolution is limited by the number of spacecraft in both the transmitting and receiving constellations.

In this dissertation, data from the Constellation Observing System for Meteorology, Ionosphere, and Climate (COSMIC) program office has been used, and the typical locations of COSMIC soundings for 24 hours has been shown in Fig. 2-11. Although this is an impressive quantity of data comparing to radiosondes, it is much less than the soundings per day achievable by a single instrument on a polar satellite. Therefore, GPS-RO atmospheric profiles cannot be a substitute for the environmental parameters provided by NCEP and ECMWF, such as GDAS, and ERA-Interim. On the other hand, because GNSS-RO provides very accurate dataset, it provides excellent reference measurements, which are used for the data validation (see Chapter4).

Occultation Locations for COSMIC, 6 S/C, 6 Planes, 24 Hrs

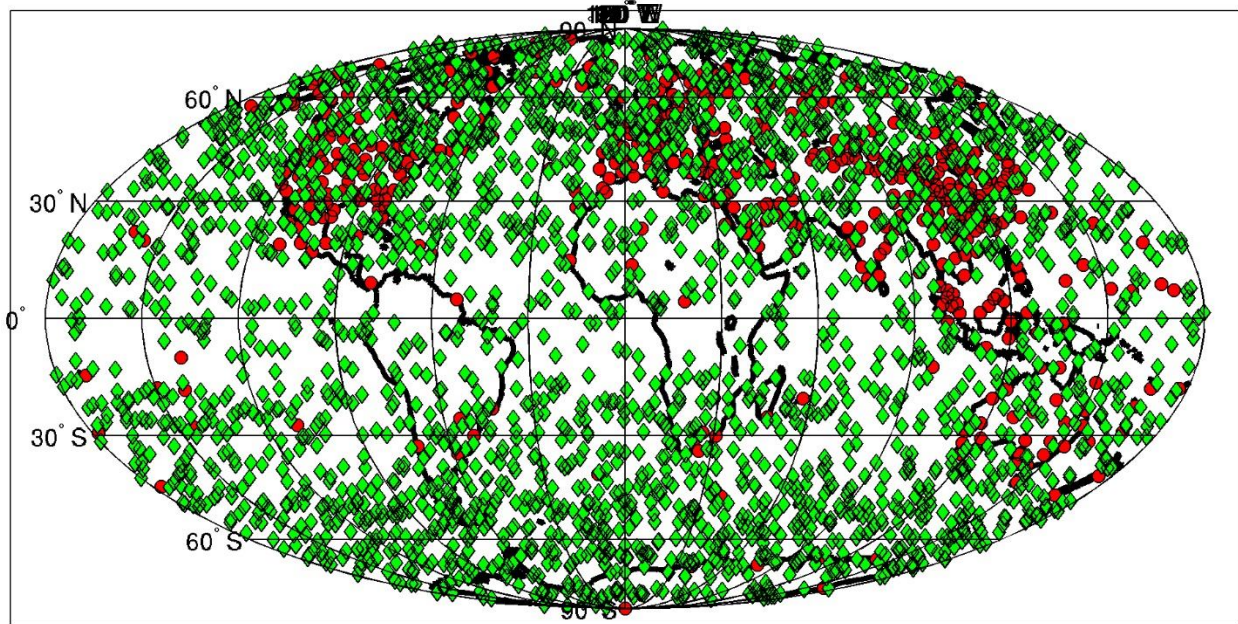


Figure 2-11 Typical locations of COSMIC soundings (green diamonds) compared to existing radiosonde launch sites (red circles) for a day. COSMIC provides about 2,500 sounding profiles every 24 hours [57].

2.6.2 *Relative Humidity Estimates*

The radiative transfer models accept relative humidity or specific humidity as input, and the in the GPS-RO profile water vapor pressure, temperature and pressure profiles are provided, fortunately, the relative humidity could be estimated using the available information from the following equations. And relative humidity is computed by water vapor pressure divided by the saturation vapor pressure

$$RH = \frac{p_w}{p_{ws}} \quad (2-9)$$

An equation used for estimating saturation vapor pressure is applied to estimate actual vapor pressure by using the air temperature [58] :

$$p_{ws} = 0.611 \exp \frac{17.27 T}{(T + 237.3)} \quad (2-10)$$

2.6.3 RTM Analysis Around 183.31 GHz

It is important to recognize that there are significant differences in the sources of the measured microwave radiances (Tb's) between sounder channels and imager channels. Specifically, in the sounder channels the atmospheric upwelling component of the bright temperature is dominant and the surface emission component is negligible; whereas in the imager channels the surface emission is dominant and the down-welling, and reflected down-welling temperatures are also significant. Moreover, for sounder channels (near the 183 GHz absorption line) the majority of this radiation comes from the upper atmosphere as illustrated in Fig. 2-12.

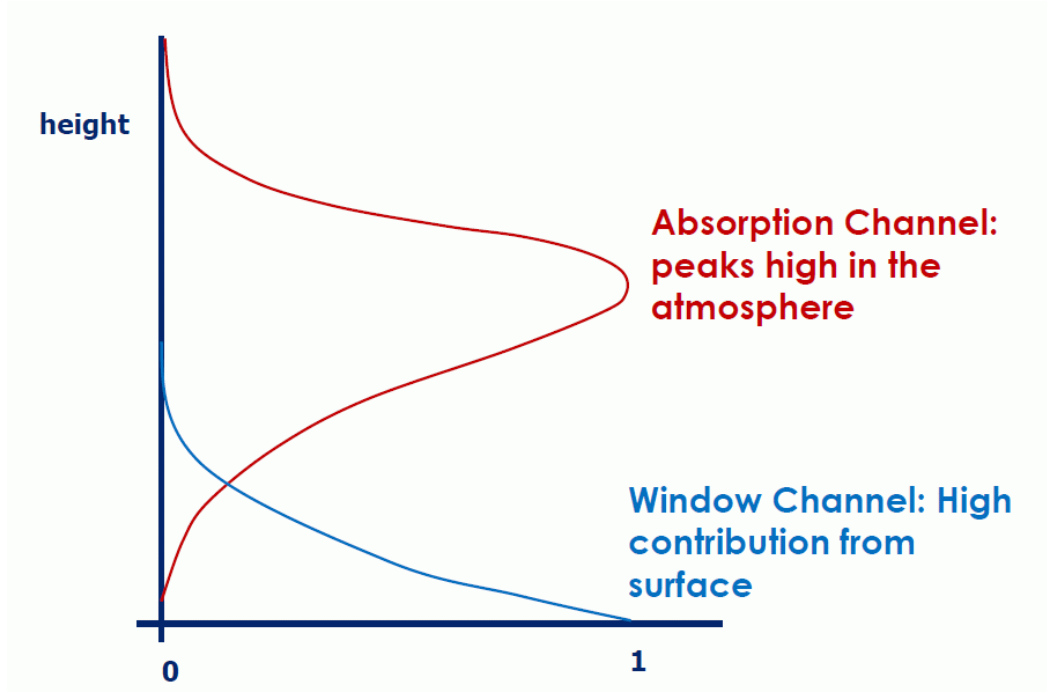


Figure 2-12: Contribution profile of a water vapour absorption channel (red) compared to a window channel (blue) [59].

2.6.4 Changes of EIA and IFOV Resolution

For the cross track scanners, as the antenna beam scans off the nadir (i.e., EIA increases), the size of IFOV increases and the resolution decreases, as illustrated in Fig. 2-13. Therefore, here we investigate the effect of reduced number of samples in our method, using the collocations of the SAPHIR and MHS instruments shown in Fig. 2-14. Blue is MHS swath, and red is SAPHIR's, and the center of their swaths is illustrated with magenta and black. We picked two 1 degree boxes of their overlap, first one in the center of the scan or nadir, and the other one in the edge of scan of the both instruments.

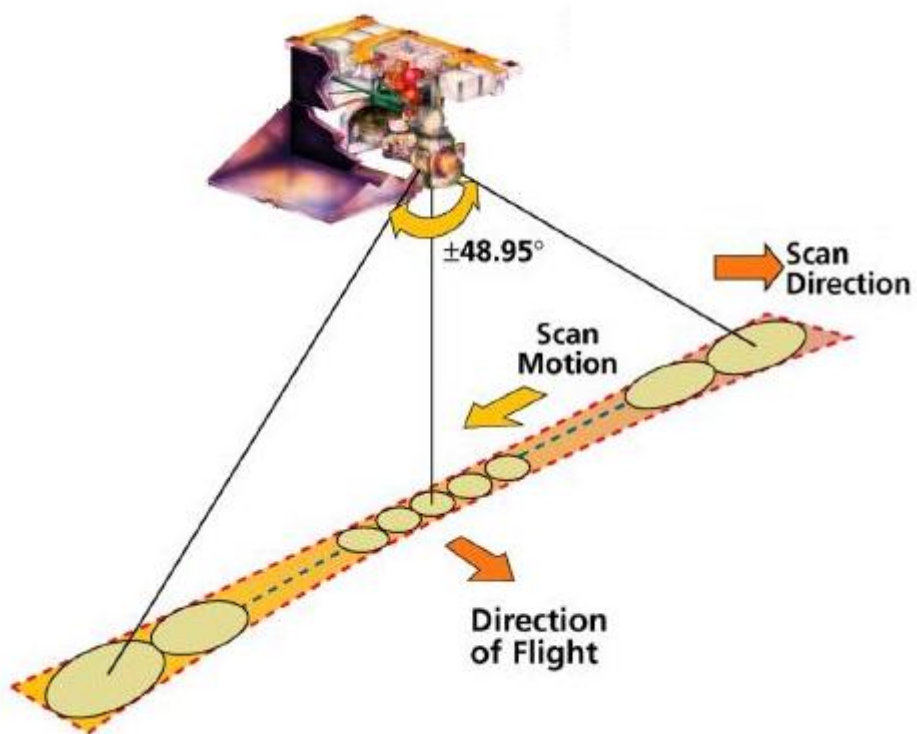


Figure 2-13: Cross track scanner antenna beam articulation, geometry and sampling [34].

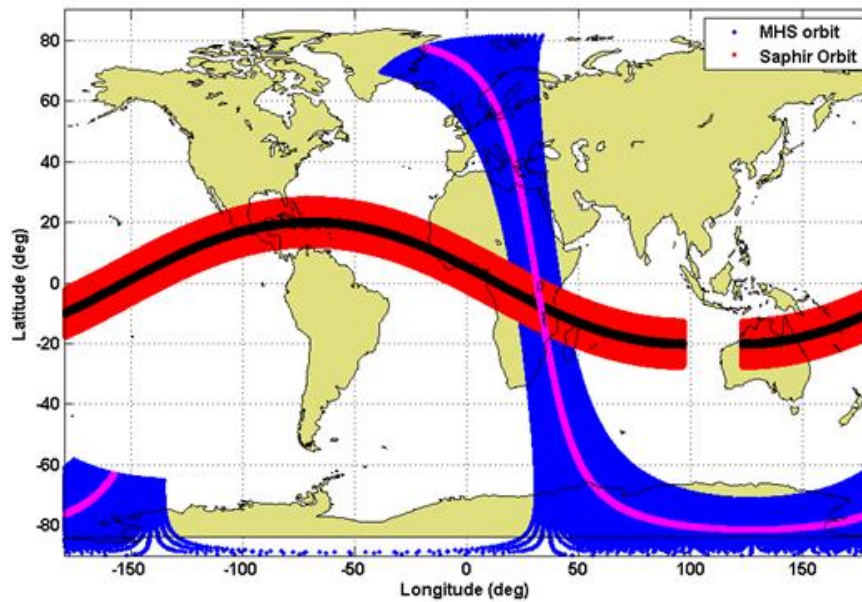


Figure 2-14 SAPHIR and MHS swaths. Blue is MHS swath, and red is SAPHIR and the centre of their swaths is illustrated with magenta and black respectively.

Figure 2-15 present results for the box at nadir, where there are 169 samples for SAPHIR, and 41 for MHS. For the box located at the edge of scan (Fig. 2-16), these numbers decrease to 74 for SAPHIR and 14 for MHS. So, the number of samples significantly decreases, but 1 degree box is sufficiently large to maintain a good number of samples for our analysis.

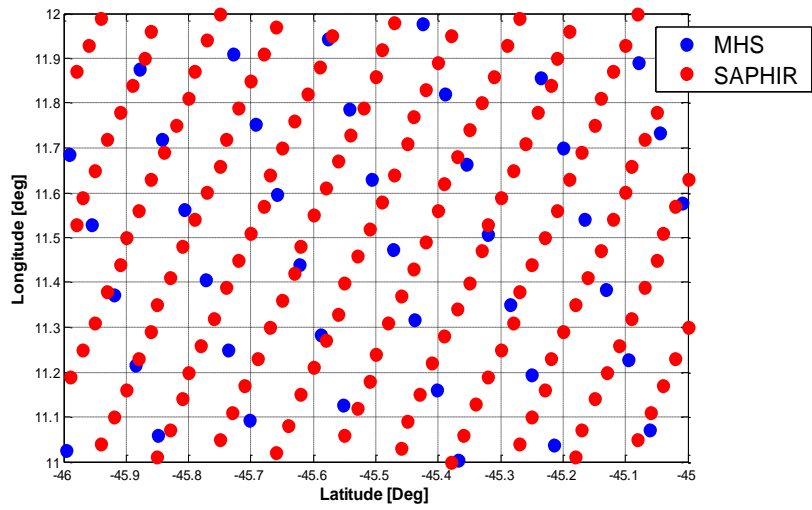


Figure 2-15: The collocated 1 degree box for the Time Window ≤ 1 Hour. In the middle of scan or close to the nadir.

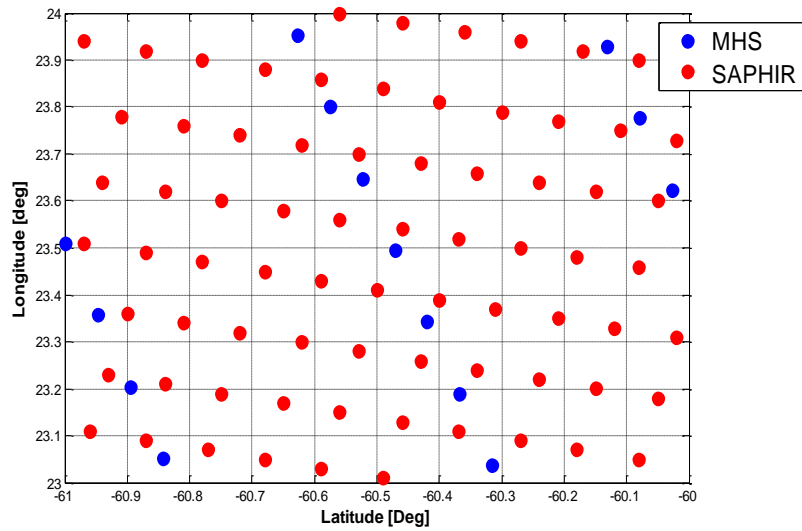


Figure 2-16. The collocated 1 degree box for the Time Window ≤ 1 Hour at the edge of scan.

Moreover, there are several details that we must check before we starting our analysis. First, in the cross track scanners, since EIA is constantly changing within 1 degree box, we want to make sure that the change in EIA at the top of atmosphere is the same as at the earth surface. Figure 2-17 shows the geometry of earth, radiometer EIA, and the top of the atmosphere. For our purposes, the top of the atmosphere is the top of the troposphere, which is around the altitude of 20 km, using the law of Sines, we can calculate the limit of EIA as follow:

$$\frac{\sin(180-EIA)}{a} = \frac{\sin(180-(180-EIA)-\frac{\gamma}{2})}{b} \quad (2-11)$$

where $\gamma = 1 \text{ deg}$, $b = 6371 \text{ Km}$, $b = a + 20 = 6391 \text{ Km}$, EIA is equal to:

$$\mathbf{EIA = 71.05 \text{ deg}} \quad (2-12)$$

Thus, this means that if the $EIA > 71$ degree, the top of the atmosphere extends beyond the vertical projection of the one degree box. However, for all the instruments in the GPM constellations, the maximum $EIA < 63$ degree, so this will not be an issue.

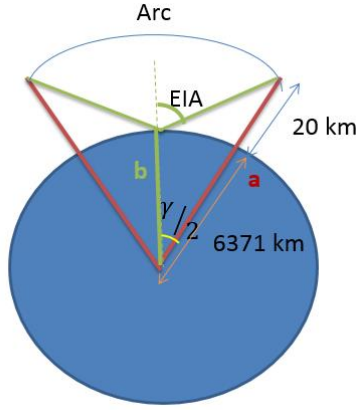


Figure 2-17: The geometry of earth, satellite EIA, and the top of the atmosphere.

Next, we need to consider within the 1 degree box, what is the variation of the EIA? For this analysis, the approach is similar above, except we should use the altitude of the satellite, which is around 830 Km. Figure 2-18 shows the geometry of earth, radiometer EIA, and the location of satellite.

$$\frac{\sin(180-EIA)}{R_e} = \frac{\sin(180-(180-EIA)-\frac{\gamma}{2})}{R_e+h} \quad (2-13)$$

$$\frac{R_e+h}{R_e} = \frac{\sin(EIA-\frac{\gamma}{2})}{\sin(EIA)} = \frac{\sin(EIA)\cos(\frac{\gamma}{2})-\sin(\frac{\gamma}{2})\cos(EIA)}{\sin(EIA)} \quad (2-14)$$

$$EIA = \arccot\left(\frac{\cos(\frac{\gamma}{2}) - \frac{R_e}{R_e+h}}{\sin(\frac{\gamma}{2})}\right) \quad (2-15)$$

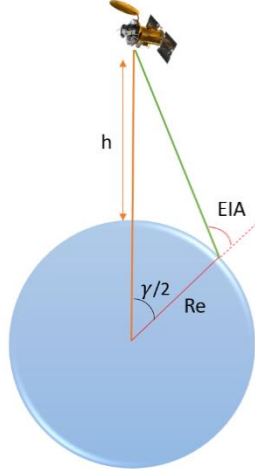


Figure 2-18: The geometry of earth, Satellite, satellite EIA.

where $\gamma = 1 \text{ deg}$, $R_e = 6371 \text{ Km}$, $h > 530 \text{ Km}$, EIA is equal to:

$$\mathbf{EIA} < \mathbf{6.5 \text{ deg}} \quad (2-16)$$

Thus in the final step, we checked our model for the variation of the modeled brightness temperature with 6.5 degree change in EIA. The results of the simulation of TBs for the 6 channels of SAPHIR around 183 GHZ for a set of typical geophysical parameters, is presented in the following table. Results show no significant changes (which is desirable), and this result demonstrates that one degree resolution is sufficient.

Table 2-1: simulated brightness temperatures for SAPHIR instrument for Nadir and 6.5 degree.

Ch EIA	Ch1	Ch2	Ch3	Ch4	Ch5	Ch6
0°	230.3786	242.1437	255.8807	262.3422	270.3551	277.5550
6.5°	230.3012	242.0741	255.8150	262.2787	270.2891	277.4899
Difference	0.0774	0.0696	0.0657	0.0635	0.066	0.0651

2.6.4.1 Changes Within the Bandwidth

One of the important factors we considered here is the variation of the modeled brightness temperatures within the Bandwidth (BW) of each channel. For the imagers, or window channels, the brightness temperature variations over the BW are not significant, so usually the center frequency has been used for the simulations. However, for sounder channels near the water vapor resonance at 183 GHz, we have significant variation within the BW; therefore, we investigated the impact of these changes. In Fig. 2-19, the modeled values of the Tbs for the 6 channels of the SAPHIR are shown for the 8 different atmospheric profiles has been shown, as it can be seen the brightness temperature changes across the bandwidth of each channel, and this variation can reach up to 4K for certain cases.

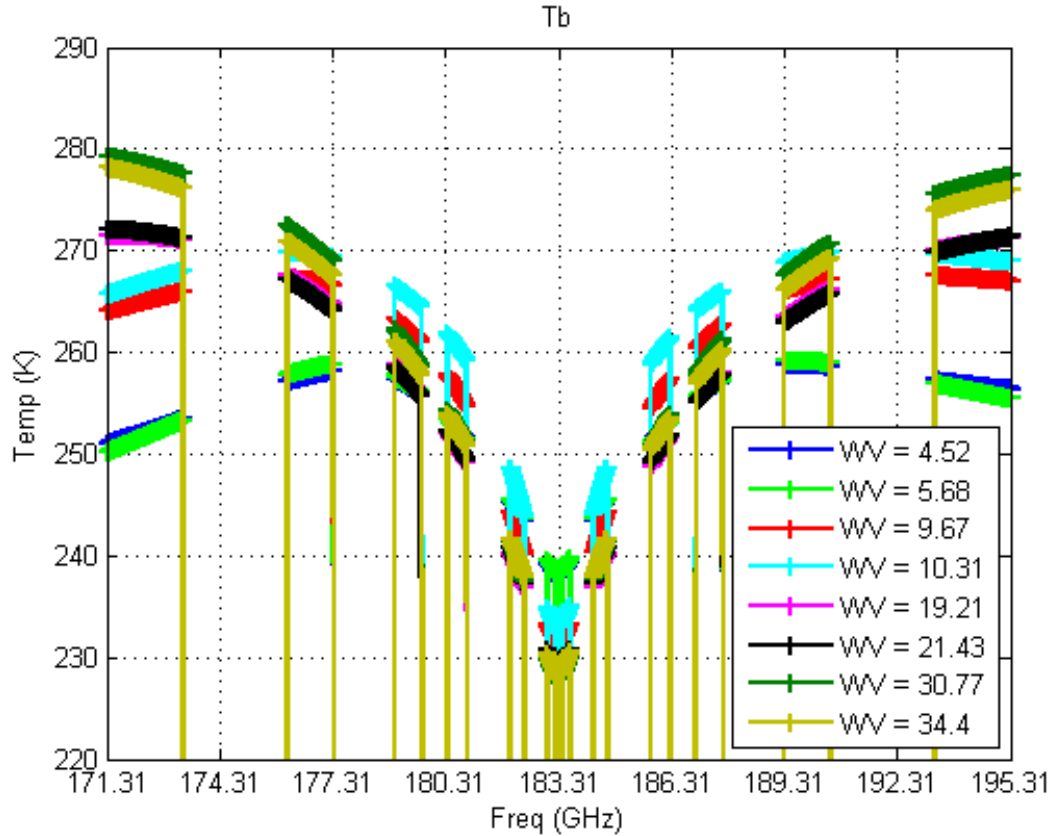


Figure 2-19: Simulated Tbs for the 6 channels of the SAPHIR for the 8 different atmospheric profiles.

Then to be accurate, we performed simulation of the Tbs across the whole BW, and we attempted to optimize the proper resolution for this purpose. With higher resolution, we have more samples and more accurate results, but the computation time is higher as well. In the following Table 2-2 the number of samples for each channel, and the associated run time using a Quad-core, Intel CPU with different resolutions is presented. Because we want > 3 sample per BW, we chose a resolution less than 100 MHz. The next Table 2-3 presents the corresponding Tbs for different channels. Since the Tb changes are small (of the order of 0.1 K) and considering the runtime, we chose the 100 MHz resolution for this study.

Table 2-2: run time, and number of samples using different resolutions.

Res (MHz)	Sim. Time (Sec)	Ch1	Ch2	Ch3	Ch4	Ch5	Ch6
5	1883.46	82	142	202	282	482	802
10	904.02	42	70	102	142	242	402
25	423.52	18	30	42	58	98	162
50	237.86	10	14	22	30	50	82
100	96.01	6	6	10	14	26	42

Table 2-3: simulated brightness temperatures using different resolutions.

Ch	Ch1	Ch2	Ch3	Ch4	Ch5	Ch6
5 MHz	239.0818	244.5833	252.2482	256.6636	258.7887	253.9704
10MHz	239.0831	244.5835	252.2481	256.6632	258.7883	253.9705
25MHz	239.0869	244.5824	252.2475	256.6619	258.7873	253.9707
50MHz	239.0933	244.5837	252.2465	256.6598	258.7856	253.9711
100MHz	239.1060	244.5862	252.2488	256.6646	258.7822	253.9719

CHAPTER 3: SENSORS AND CALIBRATION

3.1 Cross Track Scanners versus Conical Scanners

Inter-calibration of microwave radiometer channels using the GPM Microwave Imager (GMI) is a challenging task. In the GPM constellation we have a combination of cross track and conical scanner sensors, and the goal is to make a consistent measurement between all the sensors in this constellation. GMI is a conical scanner and will be the calibration reference for the other sensors in the constellation. Almost all the sensors with channels lower than 89 GHz are conical scanners, the inter-calibration between conical scanners have been done successfully over years, but for frequencies equal and higher than 89GHz, there is SSMIS on the Defense Meteorological Satellite Program (DMSP) which is a conical scanner, other sensors such as ATMS on NPP, MHS on NOAA 18, NOAA 19, MetOp-A and MetOp-B and SAPHIR on Megha -Tropique, are cross track sensors. For these sensors, each Instantaneous Field of View (IFOV) has different Earth incidence angles (EIA) and different slant paths through the atmosphere while conical scanner has constant earth incidence angle for all IFOVs.

In Fig. 3-1, the conical and cross track scanning satellites measurement geometries are presented.

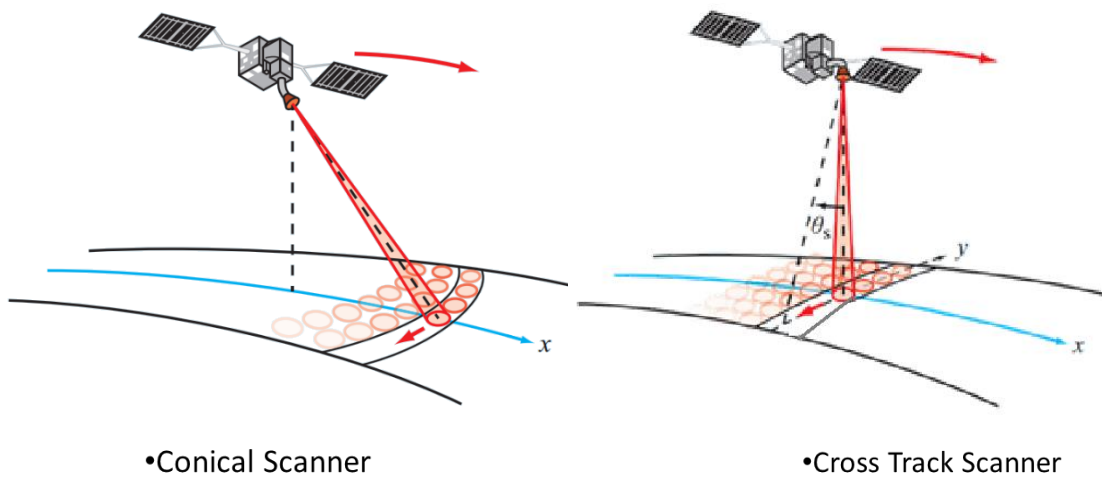


Figure 3-1: Conical scanning versus cross track scanning satellites [2].

3.1.1 Cross Track Sensors

Of the instruments used in this study, four are cross track scanners, namely; ATMS, MHS, AMSU-B and SAPHIR. Here we briefly describe them.

3.1.1.1 ATMS

ATMS is a cross-track microwave radiometer flying on board of the S-NPP satellite, which was launched on October 28, 2011 into a polar sun synchronous orbit (altitude 824 km and inclination 97.1°) [60]. The ATMS characteristics, including frequency, bandwidth, antenna beamwidth, and the noise equivalent temperature difference (NE Δ T), are reported in Table 3-1. ATMS has 22 channels operating from 23.8 to 190.31 GHz as shown in Fig. 3-2. A similar instrument is planned to fly on the U.S. next-generation polar-orbiting operational environmental satellite system named Joint Polar Satellite System (JPSS).

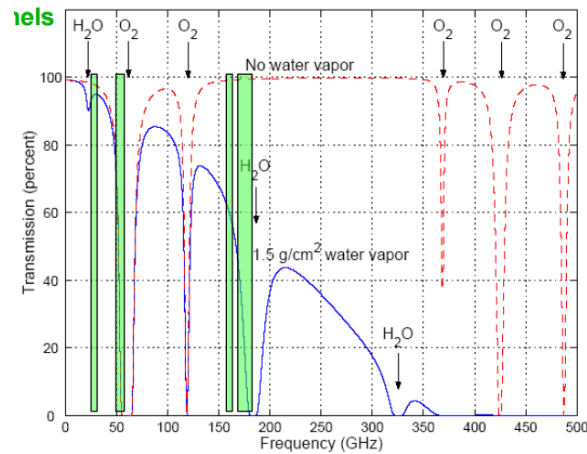


Figure 3-2: Atmospheric Transmission at Microwave Wavelengths and ATMS channels [61].

Table 3-1 ATMS Radiometric and Channel Characteristics [61].

<i>Channels</i>	<i>Frequency GHz</i>	<i>BW</i>	<i>NEDT</i>	<i>Pol</i>
1	23.80	270	0.5	QV
2	31.40	180	0.6	QV
3	50.30	180	0.7	QH
4	51.76	400	0.5	QH
5	52.80	400	0.5	QH
6	53.59±0.115	170	0.5	QH
7	54.40	400	0.5	QH
8	54.94	400	0.5	QH
9	55.50	330	0.5	QH
10	$f_0 = 57.2903$	330	0.75	QH
11	$f_0 \pm 0.3222 \pm 0.217$	78	1.0	QH
12	$f_0 \pm 0.3222 \pm 0.048$	36	1.0	QH
13	$f_0 \pm 0.3222 \pm 0.022$	16	1.5	QH
14	$f_0 \pm 0.3222 \pm 0.010$	8	2.2	QH
15	$f_0 \pm 0.3222 \pm 0.0045$	3	3.6	QH
16	88.2	2000	0.3	QV
17	165.5	3000	0.6	QH
18	183.31 ± 7	2000	0.8	QH
19	183.31 ± 4.5	2000	0.8	QH
20	183.31 ± 3	1000	0.8	QH
21	183.31 ± 1.8	1000	0.8	QH
22	183.31 ± 1	500	0.9	QH

3.1.1.2 SAPHIR

About two weeks before S-NPP, the Megha-Tropiques (MT) satellite, a joint program between France and India was launched on October 12, 2011 into a 20° inclination orbit (altitude 865 Km

and inclination 19.98°). The MT payload includes two microwave sensors relevant to the Global Precipitation Measurement (GPM) mission, namely; MADRAS, a conically scanning multi-frequency window channel radiometer and SAPHIR a water-vapor sounder with 6 channels centered on the 183 GHz water vapor line, but in this dissertation, only the SAPHIR data are used. These channels have been presented in the following Fig. 3-3. Also, the Imaging geometry of Megha-Tropiques, and SAPHIR has been presented in Fig. 3-4, and the functional block diagram of SAPHIR has been presented in Fig. 3-5.

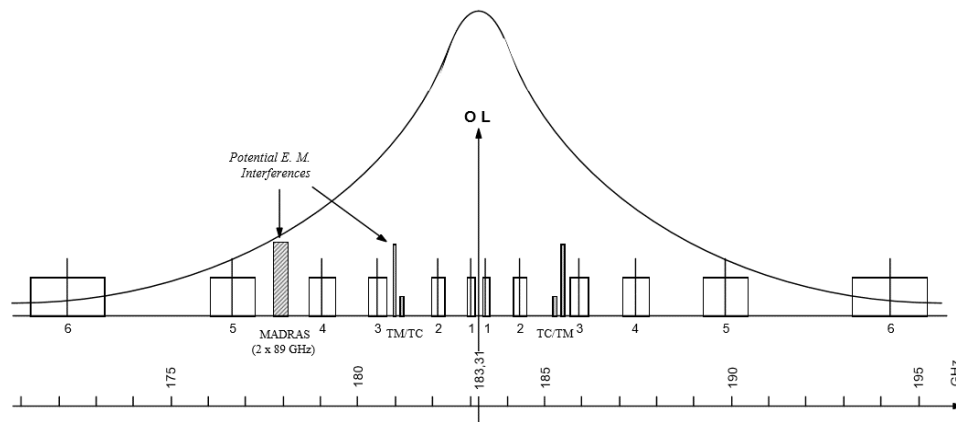


Figure 3-3: distribution of channels in SAPHIR instrument [62].

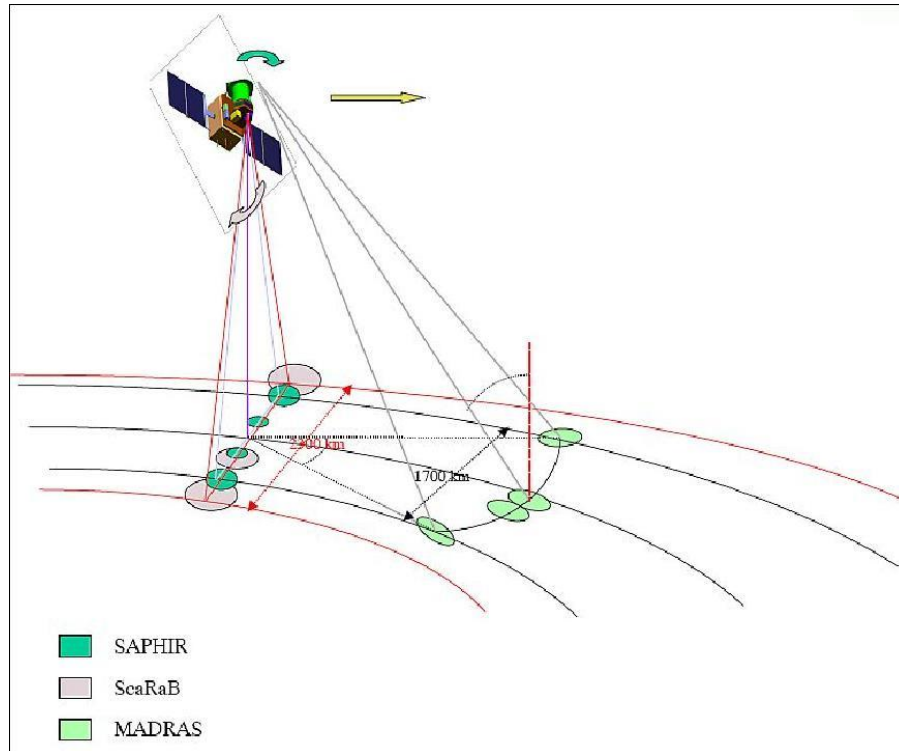


Figure 3-4: Imaging geometry of Megha-Tropiques, and SAPHIR [62].

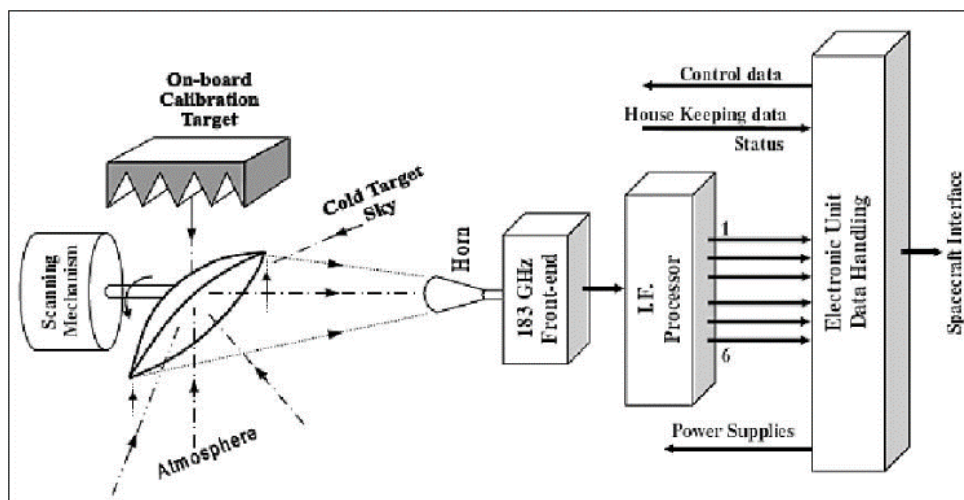


Figure 3-5: Functional block diagram of SAPHIR (image credit: CNES)[62].

Before the launch of Megha-Tropiques, there were no 183 GHz radiometers in low inclination orbits to facilitate inter-comparison of the operational (polar orbiting) microwave water vapor sounders [4, 5]. The characteristics of SAPHIR instruments, has been presented in Table 3-2.

Table 3-2 SAPHIR Radiometric and Channel Characteristics.

<i>Channels</i>	<i>Frequency GHz</i>	<i>BW</i>	<i>NEDT</i>	<i>Pol</i>
<i>1</i>	183.31 ± 0.2	200	2.35	QH
<i>2</i>	183.31 ± 1.1	350	1.45	QH
<i>3</i>	183.31 ± 2.8	500	1.36	QH
<i>4</i>	183.31 ± 4.2	700	1.38	QH
<i>5</i>	183.31 ± 6.8	1200	1.03	QH
<i>6</i>	183.31 ± 11	2000	1.10	QH

3.1.1.3 MHS

Another sensor, which we use in this dissertation, is MHS on board of MetOP-A & B and NOAA-18 & 19 satellites. These satellites are sun synchronous polar orbiters that cover the entire earth surface. MHS sensors have 5 cross-track scanning channels, with an antenna beamwidth of 1.1° and spatial resolution at nadir is approximately 16 km. The antenna provides a cross-track scan, scanning $\pm 49^\circ$ from nadir with a total of 90 earth fields-of-view per scan line at a rate of one scan every 8/3 seconds. The characteristics of MHS are presented in Table 3-3.

Table 3-3 MHS Radiometric and Channel Characteristics

<i>Channels</i>	<i>Frequency GHz</i>	<i>BW</i>	<i>NEDT</i>	<i>Pol</i>
1	89.0	2800	2.35	QV
2	157.0	2800	1.45	QV
3	183.31 ± 1.0	500	1.36	QH
4	183.31 ± 3.0	1000	1.38	QH
5	190.31	2200	1.03	QV

3.1.1.4 AMSU-B

AMSU-B is very similar to MHS. Both AMSU-B and MHS sensors have 5 cross-track scanning channels. The instruments have antenna beamwidths of 1.1° , with the spatial resolution at nadir being approximately 16 km. Their antennas provide a cross-track scan, scanning $\pm 49^\circ$ from nadir, with a total of 90 Earth fields-of-view per scan line at a rate of one scan every 8/3 seconds [63]. The characteristics of AMSU-B have been presented in Table 3-4. As it can be seen, the AMSU-B and MHS almost identical. Fig. 3-6 shows the time span of the AMSU-B and MHS, SAPHIR, and ATMS since the TRMM launch. Since MHS and AMSU-B together provide two decades measurements, if we calibrate these sensors successfully, we can have a consistent weather data for almost two decades.

Radiometers	1998	1999	2000	2001	2002	2003	2004	2005	2006	2007	2008	2009	2010	2011	2012	2013	2014	2015	2016
TRMM/ TMI																			
NOAA 15/ AMSU-B																			
NOAA 16/ AMSU-B																			
NOAA 17/ AMSU-B																			
NOAA 18/ MHS																			
METOP-A/ MHS																			
NOAA 19/ MHS																			
METOP-B/ MHS																			
Megha-Tropique/SAPHIR																			
NPP/ ATMS																			
GPM/ GMI																			

Figure 3-6: Time spans for the TRMM and GPM missions and the polar orbiters in these missions.

Table 3-4 Specifications of AMSU-B channels [64].

<i>Center Frequency (GHz)</i>	<i>Bandwidth (MHz)</i>	<i>NEΔT (K)</i>	<i>Polarization</i>
89 ± 0.9	1000	0.37	QV
150 ± 0.9	1000	0.84	QV
183.31 ± 1.0	500	1.06	QV
183.31 ± 3.0	1000	0.70	QV
183.31 ± 7.0	2000	0.60	QV

3.1.2 Conical Scanning Instruments

3.1.2.1 GMI

The Global Precipitation Measuring (GPM) mission is an international scientific collaboration to measure precipitation worldwide every 3 hours. The GPM Microwave Imager is a conical scanning microwave radiometer with 13 channels ranging from 10 to 183 GHz. GPM will continue Tropical Rainfall Measuring Mission (TRMM) mission, and in addition to carrying window channels similar to those on the TRMM Microwave Imager (TMI), GMI carries four high frequency, millimeter-wave, channels at frequencies near 166 GHz and 183 GHz. Also, because GMI has a larger antenna than TMI, with a 1.2 m diameter, it significantly improves spatial resolution of the measurements.

A major requirement of the GPM observatory is to provide a space borne radiometric calibration standard for precipitation measurements from the cooperative satellites in the constellation. Because of its 65° inclination low earth orbit, the GPM observatory provides frequent near-simultaneous collocations of brightness temperatures (T_b) between GMI and other satellite radiometers. The use of GMI as the calibration transfer standard enables a unified inter-satellite radiometric calibration (X-CAL) between all other GPM constellation passive microwave instruments. GMI is a conical scanner; its components are shown in Fig. 3-7.

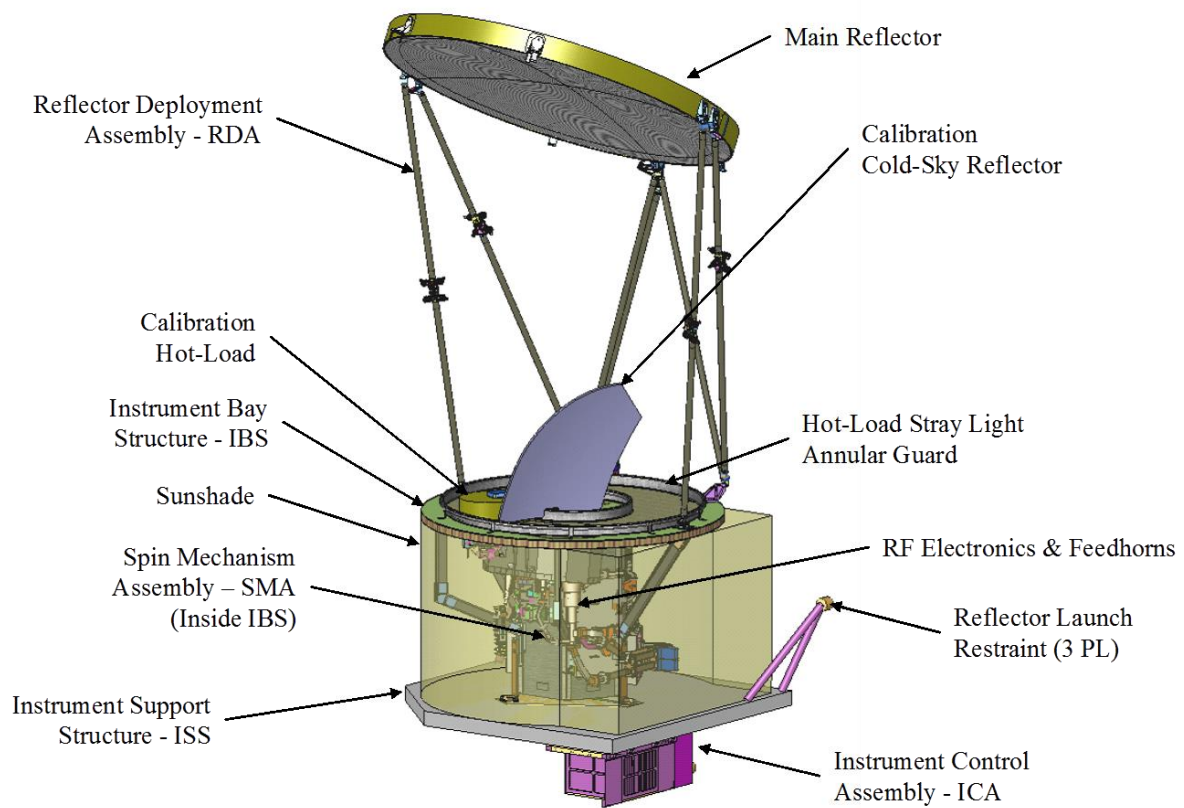


Figure 3-7 GMI instrument.

The scan geometry of GMI is illustrated in Fig. 3-8. From the GPM altitude of 407 Km, this conical scanner has a constant EIA = 52.8° , and over the 140° of azimuth for the earth viewing sector, results in a swath of 931 Km.

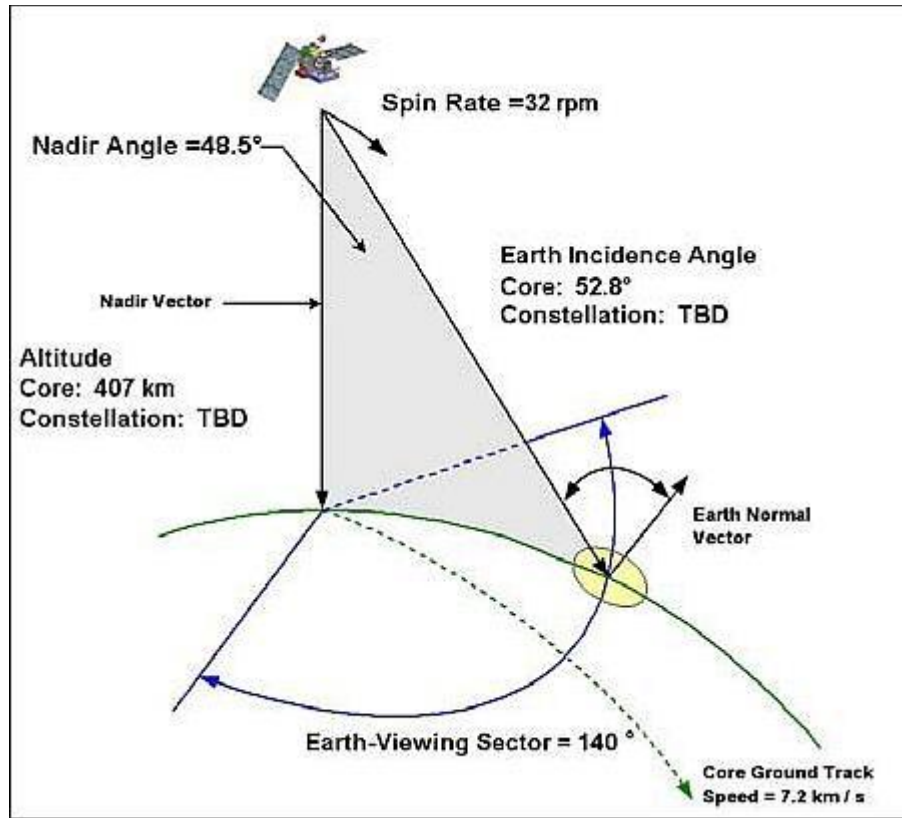


Figure 3-8 Scan geometry of GMI (NASA) [65].

The characteristics of the 13 channels of the GMI have been presented in the Table 3-5, but in this dissertation only the channels higher than 89 GHz have been used. Also, it should be mentioned that the size of IFOV varies for the different channels as illustrated in Fig. 3-9.

Table 3-5 GPM GMI Channel Specifications [65].

Channel No	Central Frequency (Ghz)	Central Frequency Stabilization (\pm MHz)	Bandwidth (MHz)	Polarization	Integration time (ms)	NEDT (K)	Antenna beamwidth @ 3 dB (°)
1	10.65	10	100	V	9.7	0.96	1.75
2	10.65	10	100	H	9.7	0.96	1.75
3	18.70	20	200	V	5.3	0.84	1.00
4	18.70	20	200	H	5.3	0.84	1.00
5	23.80	20	400	V	5.0	1.05	0.90
6	36.50	50	1000	V	5.0	0.65	0.90
7	36.5	50	1000	H	5.0	0.65	0.90
8	89.00	200	6000	V	2.2	0.57	0.40
9	89.00	200	6000	H	2.2	0.57	0.40
10	166.0	200	3000	V	3.6	1.5	0.40
11	166.0	200	3000	H	3.6	1.5	0.40
12	183.31 \pm 3	200	3500	V	3.6	1.5	0.4
13	183.31 \pm 7	200	4500	V	3.6	1.5	0.4

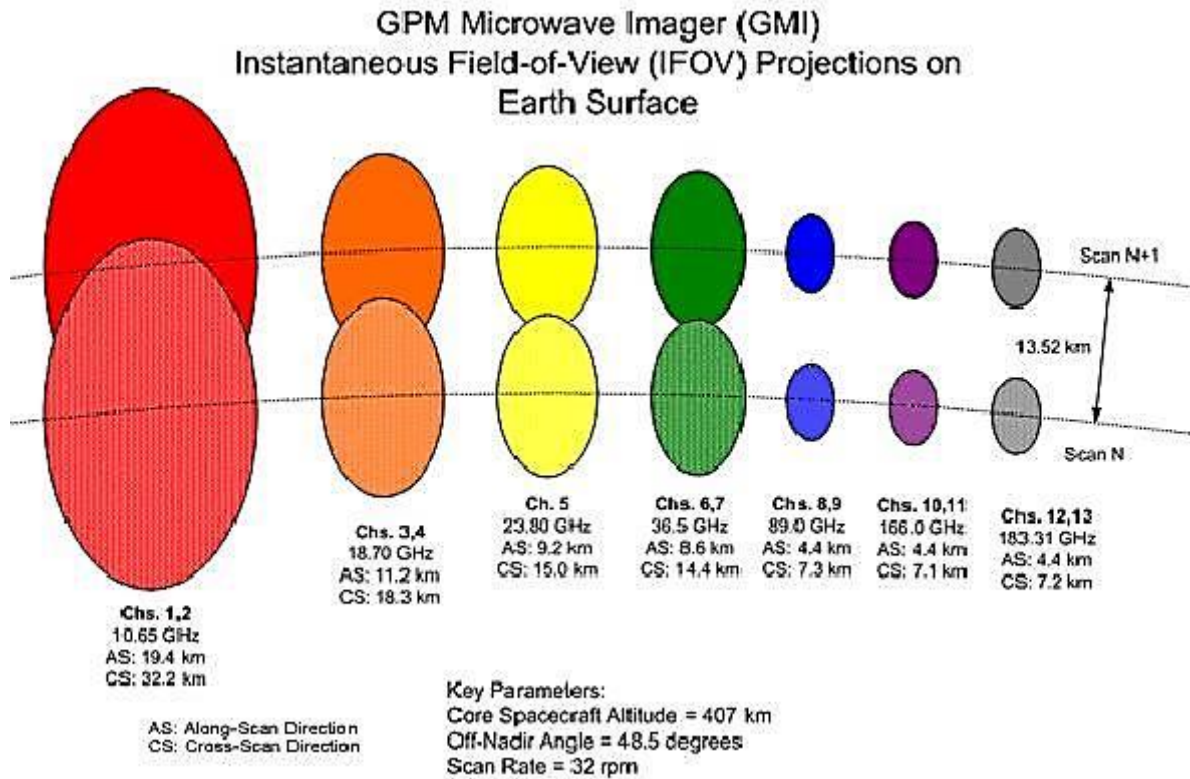


Figure 3-9: Antenna footprint (IFOV) for GMI channels for two consecutive along-scans (credit: NASA) [65].

3.1.2.2 SSMIS

SSMIS is a conical-scanning imager/sounder with 24 channels from 19 to 183 GHz, with 3 water vapor sounding channels around 183 GHz (including the sounder channels of GMI). This polar orbiting radiometer operates on board the USAF DMSP (Defense Meteorological Support Program) F16 to F19 satellites, which is a part of GPM constellation. The characteristics of this instrument are presented in the Table 3-6, and while the instruments on the F16 to F19 are not identical, the sounder channels of interest to this dissertation are the same.

Table 3-6: F18 SSMIS Sensor Characteristics (similar to F16, just the first 5 channels are Horizontal) [65].

Channel	Center Freq.(GHz)	Passband(MHz)	Freq.(MHz)/Polar.	NEDT(K)	Sampling Interval(km)	Footprint (km)
1	50.3	400	10 H	0.4	37.5	38 x 38
2	52.8	400	10 H	0.4	37.5	38 x 38
3	53.596	400	10 H	0.4	37.5	38 x 38
4	54.4	400	10 H	0.4	37.5	38 x 38
5	55.5	400	10 H	0.4	37.5	38 x 38
6	57.29	350	10 RCP(*)	0.5	37.5	38 x 38
7	59.4	250	10 RCP	0.6	37.5	38 x 38
8	150	1500	200 H	0.88	37.5	14 x 13 (imager)
9	183.31±6.6	1500	200 H	1.2	37.5	14 x 13 (imager)
10	183.31±3	1000	200 H	1.0	37.5	14 x 13 (imager)
11	183.31±1	500	200 H	1.25	37.5	14 x 13 (imager)
12	19.35	400	75 H	0.7	25	73 x 47
13	19.35	400	75 V	0.7	25	73 x 47
14	22.235	400	75 V	0.7	25	73 x 47
15	37	1500	75 H	0.5	25	41 x 31
16	37	1500	75 V	0.5	25	41 x 31
17	91.655	3000	100 V	0.9	12.5	14 x 13 (imager)
18	91.655	3000	100 H	0.9	12.5	14 x 13 (imager)
19	63.283248±0.285 271	3	0.08 RCP	2.4	75	75 x 75
20	60.792668±0.357 892	3	0.08 RCP	2.4	75	75 x 75
21	60.792668±0.357 892±0.002	6	0.08 RCP	1.8	75	75 x 75
22	60.792668±0.357 892±0.006	12	0.12 RCP	1.0	75	75 x 75
23	60.792668±0.357 892±0.016	32	0.34 RCP	0.6	75	75 x 75
24	60.792668±0.357 892±0.050	120	0.84 RCP	0.7	37.5	75 x 75

RCP - denotes right-handed circular polarization.

3.2 Cross Track with Cross Track

In the calibration of Cross Track scanning radiometers operating on different satellites, it should be noted that the matchups have different EIA's and different slant paths through the atmosphere. Also, with single difference comparisons of Tb's (even if the sensors are identical),

it is not possible to accurately determine the biases; except for the cases that EIAs of the two sensors are equal. Therefore, the single difference technique works well only when sensors look through nearly the same atmosphere path. This happens for intersections near the satellite sub tracks, when the radiometers view the surface at EIA's $< 15^\circ$ and their EIA differences are $< 5^\circ$.

On the other hand, when using the double difference technique to determine the radiometric biases, the EIA angle dependence should be eliminated, which results in more matchups. However, this assumes homogeneous atmospheric conditions that do not always exist, and filters for removing the matchups with non-homogeneous atmospheric conditions are required. Nevertheless, this significantly increases the number of match-ups for the double difference technique in comparison with the restricted single difference match-ups as illustrated in Fig. 3-10 for two cross track scanning satellites.

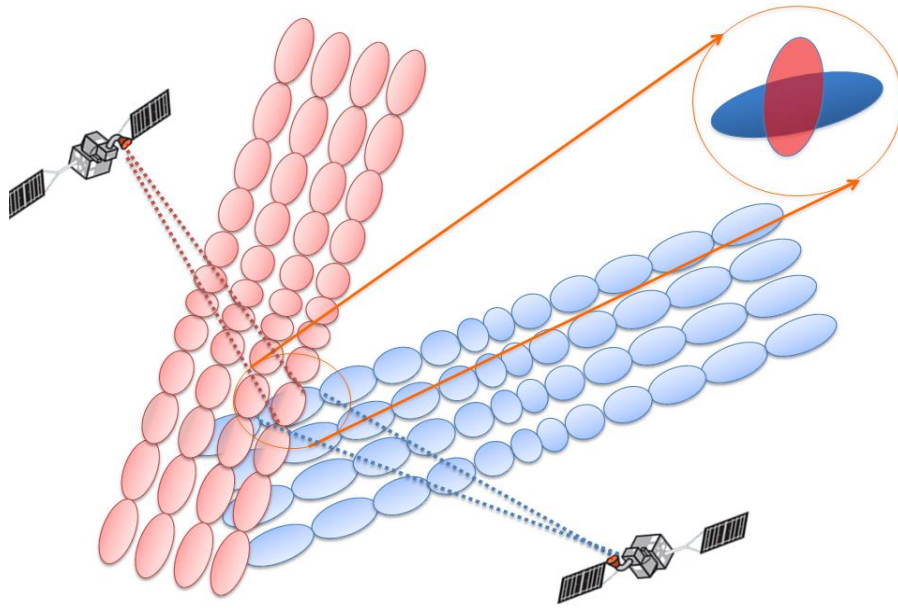


Figure 3-10: Cross track scanning satellite intersecting with another cross track scanning satellite.

Prior to GPM launch, the XCAL decided that the Microwave Humidity Sounder (MHS) on board the METOP-A satellite would be the transfer standard for the sounding channels (as a proxy of GMI). And to have a consistent dataset, we need to calibrate SAPHIR, ATMS, and MHS instruments together prior to the GMI. All of these sensors are cross-track scanners, and as it was described before, the size of IFOV and scan angles is changing along the scan in these instruments. Here, the DD procedure was modified to include both individual IFOV match-ups and binned averages over 1° boxes, and the DD bias determination has been examined for scan-position dependent biases. Where the absolute differences between their EIAs are within $\pm 5^\circ$. Also, conservative filters are applied to limit comparisons to clear sky oceanic observations within $< \pm 1$ hour.

Our team has successfully performed initial radiometric inter-calibration of the following millimeter radiometers: SAPHIR onboard the Megha-Tropiques satellite, Microwave Humidity

Sounder (MHS) on board METOPB, NOAA18, and NOAA19 satellites, Advanced Technology Microwave Sounder (ATMS), and Special Sensor Microwave Imager Sounder (SSMIS) on board DMSP F-series satellites as described by Ebrahimi et al. [66].

3.3 Conical with Cross Track

The conical with cross track scanner collocation has been illustrated in the Fig. 3-11. Concerning the geometry, there are major differences between cross track scanners and conical scanners. In conical scanning, the antenna is pointed off-nadir a fixed cone angle of incidence and the plane of incidence (containing the line-of-sight) is rotated about the nadir pointing axis, which results in a fixed constant: earth incidence angle (EIA), fixed vertical and horizontal beam polarization, and an constant instantaneous field of view (IFOV) along a circular path on the surface. Thus, when comparing the Tbs with mixed polarization with the Tbs from the conical scanners, we need to calculate the Tbs with the mixed polarization from the Tbs with the vertical and horizontal polarizations. The quasi-vertical brightness temperature is calculated as [67]:

$$\begin{aligned} T_{Qv} &= T_v \cos^2(\alpha) + T_h \sin^2(\alpha) \\ T_{Qh} &= T_h \cos^2(\alpha) + T_v \sin^2(\alpha) \end{aligned} \tag{3-1}$$

where the scan angle, α , is related to the EIA as:

$$\alpha = \sin^{-1}\left(\frac{R_e}{R_e + H} * \sin(\pi - EIA)\right) \tag{3-2}$$

$R_e = 6,371 \text{ km}$ is Earth radius, and H is the satellite altitude.

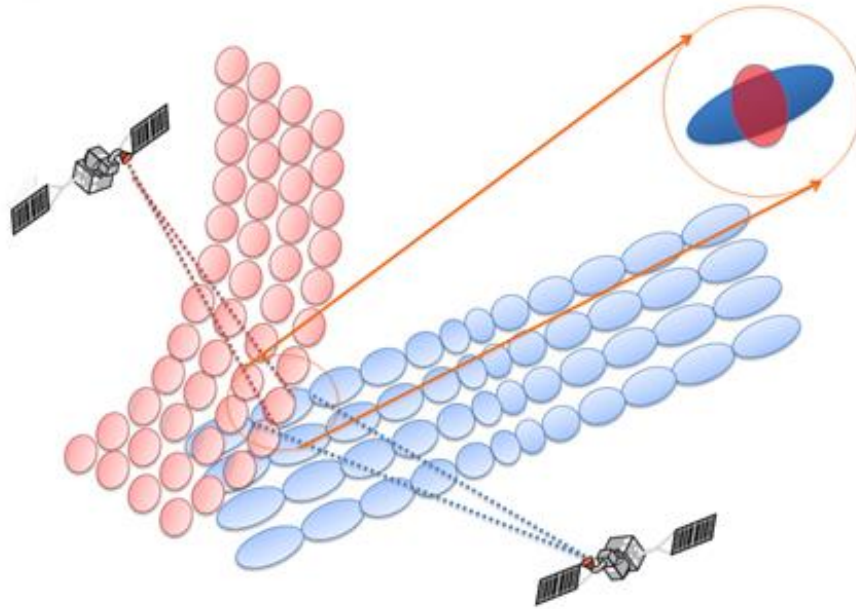


Figure 3-11: Conical scanning satellite intersecting with cross track scanning satellite.

GMI which is a conical scanner, is the transfer standard in the GPM constellation, the most of satellites with sounder channels are cross track scanners, the sensors that we have used here are SAPHIR on board of Mega-Tropique, ATM on board of NPP, and four nearly identical MHS on the board of MetOp-A, MetOp-B, NOAA-18 and NOAA-19, in the following table these sensors with their frequencies bands have been displayed.

Table 3-7: Sounder channels pairing.

Sensor	Sounder channel frequencies in GHz, $\pm n$ refers to $183.31 \pm n$									
SAPHIR (Cross Track, Inclined Orbit)				± 0.2	± 1.1		± 2.7	± 4.2	± 6.8	± 11
MHS on METOPA, B NOAA18 and 19 (Cross Track, Polar)		89 V	157 V		± 1		± 3		190 V	
ATMS (Cross Track, Polar)	23.8 V	88.2 V	165.5 H		± 1	± 1.8	± 3.0	± 4.5	± 7.0	
SSMIS on F17, F18, F19 (Conical, Polar)			150 H		± 1		± 3		± 7.0	
GMI Freq. (Conical, Inclined)	23.8 V	89 V	166 H/ 166 V	± 3.0						± 7.0

CHAPTER 4: CALIBRATION RESULTS

The inter-calibration has several steps. The first step involves a pre-screening process in which calibration biases across the scan or along the orbit path are removed [16]. Examples include removing cross-track biases [68] accounting for an emissive reflector [23] and solar intrusions and/or thermal gradients in the hot load [69-71]. Geolocation analysis is also used to identify and correct for errors in the EIA or view angle resulting from mounting offsets in the feed-horns and/or spacecraft attitude errors [7]. Although generally small, these errors can have a significant impact on the simulated Tb values and thus the resulting estimates of calibration differences. Once corrections are applied, a variety of techniques developed by teams within the XCAL working group are used to compare the calibrations of the constellation radiometers to the calibration reference sensor. The goal is to adjust the sensor calibration of the constellation radiometers to be physically consistent with the reference radiometer (i.e. GMI). To do this, the inter-calibration techniques compare channels at similar frequencies, accounting for expected differences in viewing parameters, frequency, bandwidth, polarization, and view angles using radiative transfer models. Comparing results from multiple independent approaches helps to identify flaws or limitations of a given approach and/or errors in the implementation. Consistency between approaches also increases confidence that the resulting Tb differences are due to calibration issues and provides a measure of the uncertainty.

4.1 Pre-screening

4.1.1 SAPHIR

In the prescreening the SAPHIR we found some anomalies in some orbits, one example of these anomalies has been presented in the Fig. 4-1. From longitude 40 degree to 120 degree, as we see there is an anomaly in the data, SAPHIR data has a swath triple time of the normal data set, and the incidence angle exceeds the 53 degree, we found these kind of anomalies for a few orbits in each year since the SAPHIR lunch. These are a result of incorrect geolocation in the data, and we have avoided these data with a simple EIA filter. In each scan SAPHIR data should be changing from -53 to 53 degree, and if the EIA exceeds this limit, we flag it as bad data.

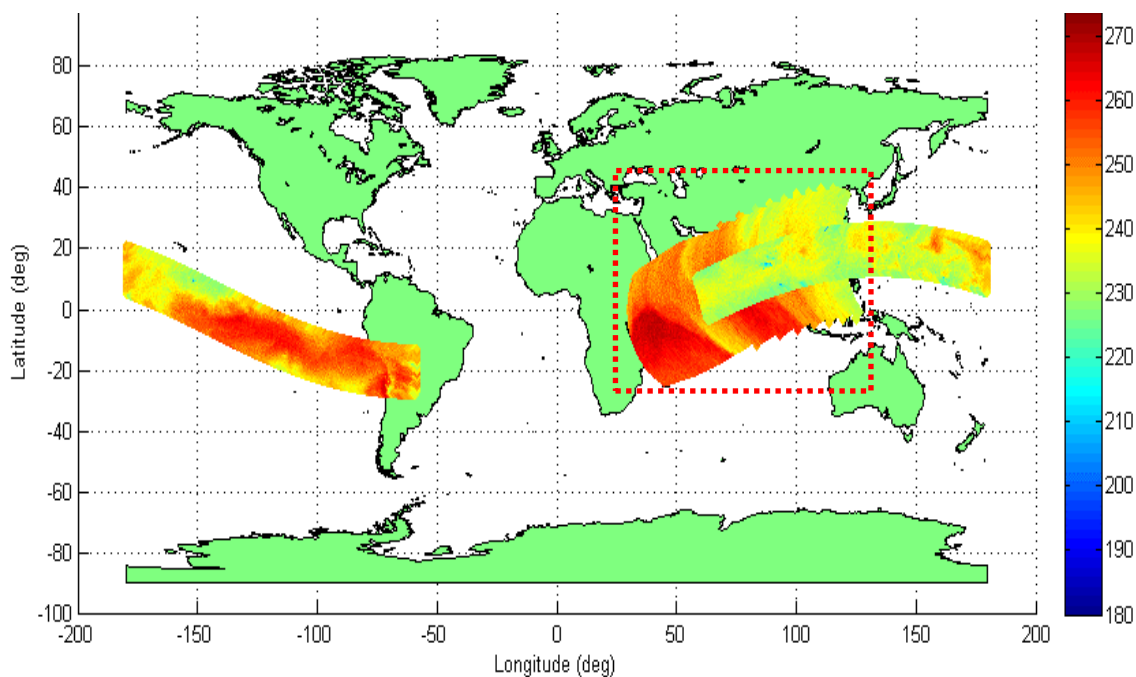


Figure 4-1: Brightness temperature of SAPHIR for the first Channel for an orbit with anomaly (20140724-S034853-E053048).

Also, we realized nadir is not the middle of the scan as it supposed to be. SAPHIR has 182 pixels in each scan, and nadir is in pixel 94. Which it causes a 1 to 2 degree biases in incidence angle versus the scan position. We have done similar analysis for other sensors, but we have not found any significant anomaly so far. In order be in the safe side, we have used similar filters to check the EIA for each scan position to make sure they do not exceeds the limits. Also, we have removed the outlier observations in each channel using a Gaussian filter, with the threshold of 3 sigma.

To start with, one full month of SAPHIR 1Base data derived from V 1.04 L1Base are used. This analysis is done for Month of August 2012. Preliminary look in the data, show few ambiguous Inc. Angle observations, which are filtered using a simple filter. A reference earth incidence angle (EIA) for each scan position is derived using simple average of all observed EIAs for the month. The average of EIA versus scan position has been presented in the Fig.4-2. If observed EIA- Ref. EIA $<\pm 1^\circ$ for all scan position, then that scan is accepted, otherwise it is rejected. The volume of data rejected over the month is less than 1%. All the analysis presented here, used these filtered data. Figure 4-3, shows the histogram of the data, before, and after filtering.

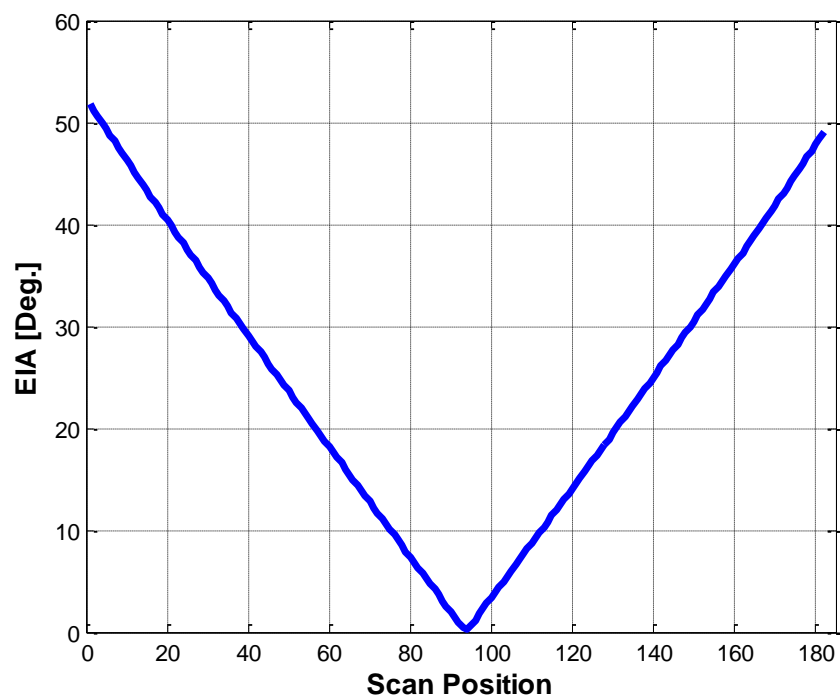


Figure 4-2: EIA reference Used for the filtering SAPHIR data.

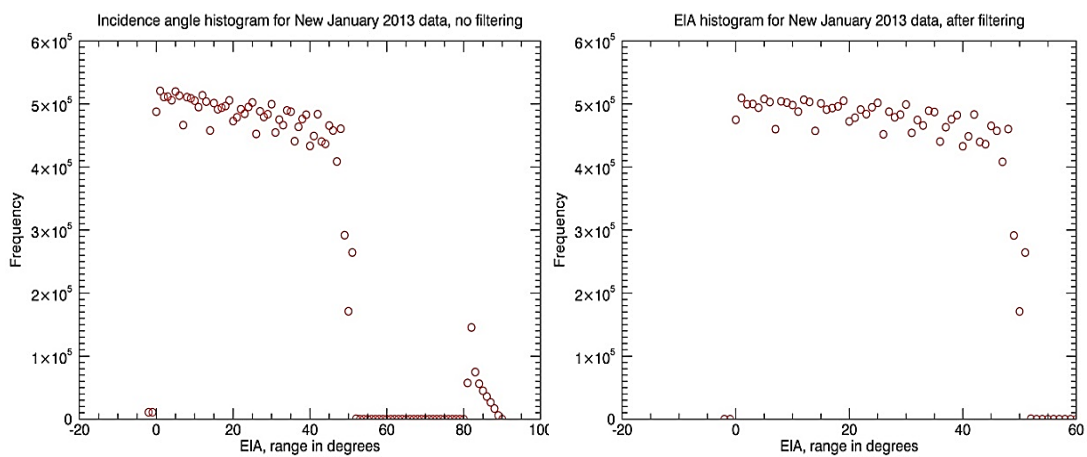


Figure 4-3: Before and after filtering with new reference.

4.1.2 MHS

Similar analysis have been performed for the MHS data. Here, the 1Base data derived from V04 L1Base are used. A reference earth incident angle (EIA) for each scan position is derived using simple average of all observed EIAs for the month. If observed EIA - Ref. EIA $< \pm 1^\circ$ for all scan position, then that scan is accepted, otherwise it is rejected. The volume of data rejected over the month is less than 1%. So far all the analysis presented used these filtered data.

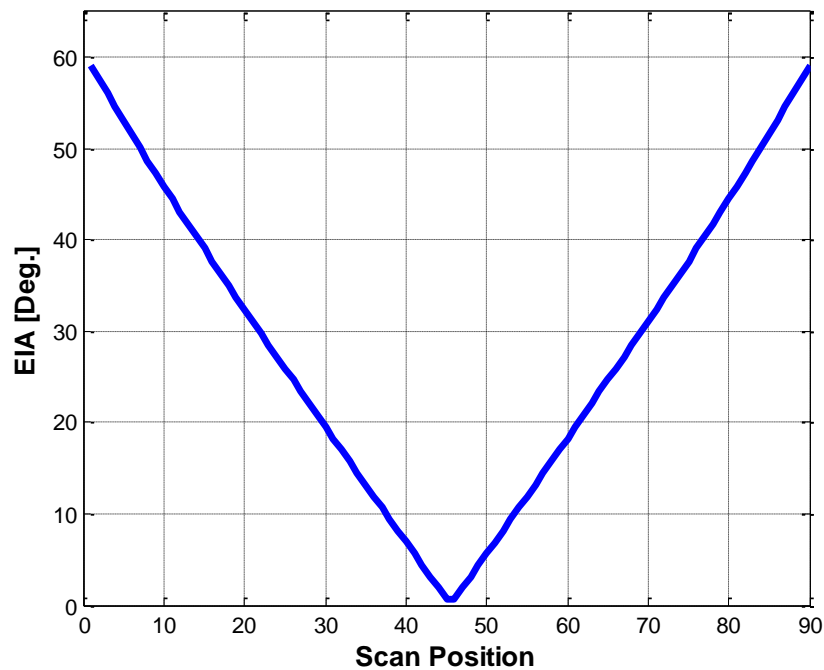


Figure 4-4: EIA reference Used for the filtering MHS data.

4.2 Clear Sky and Clear Ocean

Clouds can affect the satellite observations, particularly studies show clouds could have significant effect on 183 GHz channels measurements [72]. Also, the radiative transfer models which we use are designed for clear sky conditions. Therefore, it is required to filter out the cloud-contaminated observations before calculating the biases. Because of the atmospheric temperature rate, the Tbs for the channels sensitive to higher altitudes of the atmosphere are lower than the Tbs for the channels sensitive to the lower altitudes. In the presence of optically thick clouds, the Tbs for the upper channels become either very close or even greater than the Tbs for the lower channels [73, 74]

Here, for filtering the cloud, two filters have been applied to the datasets. One uses a convection filter that guarantee that each channel should be at least 1K warmer than the one above [75], and the other filter is the one presented by Moradi et al [74], using the Ice Water Path (IWP) data retrieved from the ground cloud radar , they have developed a cloud filter for SAPHIR. Which is as follow:

$$T_{b\ 183\pm1} - T_{b\ 183\pm7} < -15 \text{ and } T_{b\ 183\pm1} > 240\ K \quad (4-1)$$

Figure 4-5 provides the basis for this filter. It shows the difference between Tb1 and Tb7, i.e., $\Delta Tb = Tb1 - Tb7$, as a function of IWP values. As shown, the observations are almost independent of IWP as long as ΔTb is less than $-15\ K$; then, ΔTb increases with IWP. This figure also shows the relation between Tb1 and IWP. Tb1 is normally larger than 240 K under clear-sky conditions or in the presence of thin clouds and then decreases with IWP [74].

Also for the emissivity model used in the RTM model is accurate for clear ocean, so here the sea ice has been filtered using the ice flag from the environmental dataset, also the surface type flag embedded in the MHS data sets. And the sea surface temperature.

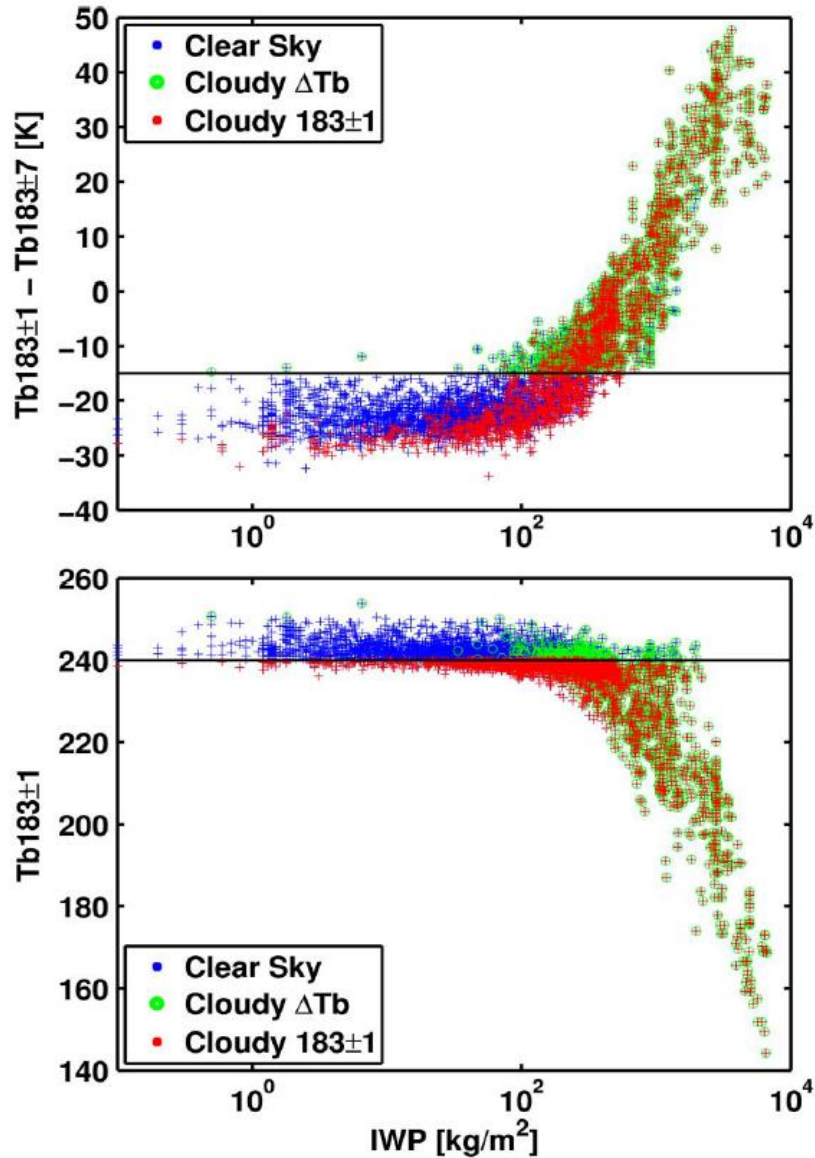


Figure 4-5 Relation between (top) IWP and $\Delta Tb = Tb_1 - Tb_7$ and (bottom) IWP and ATMS Tb s from channel 1. The legend shows the data that are considered either clear or cloudy by one of the filters [74].

4.3 Double Differences

4.3.1 *Cross Track with Cross Track*

The Tb dataset used for this study are; version V04A 1Base, and 1C files for SAPHIR, ATMS, and MHS data from March 2014 to March 2016.

4.3.1.1 *SAPHIR/MHS Comparison*

As mentioned before in each cross-track scanner, each antenna scan position has a different Earth incidence angle (EIA) and a different slant path through the atmosphere. Thus, it is important to investigate the changes of biases with incidence angle. In the ideal case, there should not be any scan position dependences in the biases, and it is necessary to eliminate any dependencies to EIA changes. In the Fig. 4-6, the 2D histograms of DD biases between the SAPHIR and MHS radiometers are presented for 183.31 ± 1 GHz channel. Since both sensors have nearly identical center frequencies and bandwidths, the objective is to investigate the radiometric bias changes with scan angle. To emphasize only the scan dependence, the DD anomaly is calculated by subtracting the mean DD bias (over all scan positions) from the DD for each scan position. Considering the theoretical (modeled) Tbs, the RTM with the Rosenkranz model is used with four different sources of environmental data; namely: GDAS, ERA-I, GDAS plus Retrieved RH, and ERA-I plus Retrieved RH.

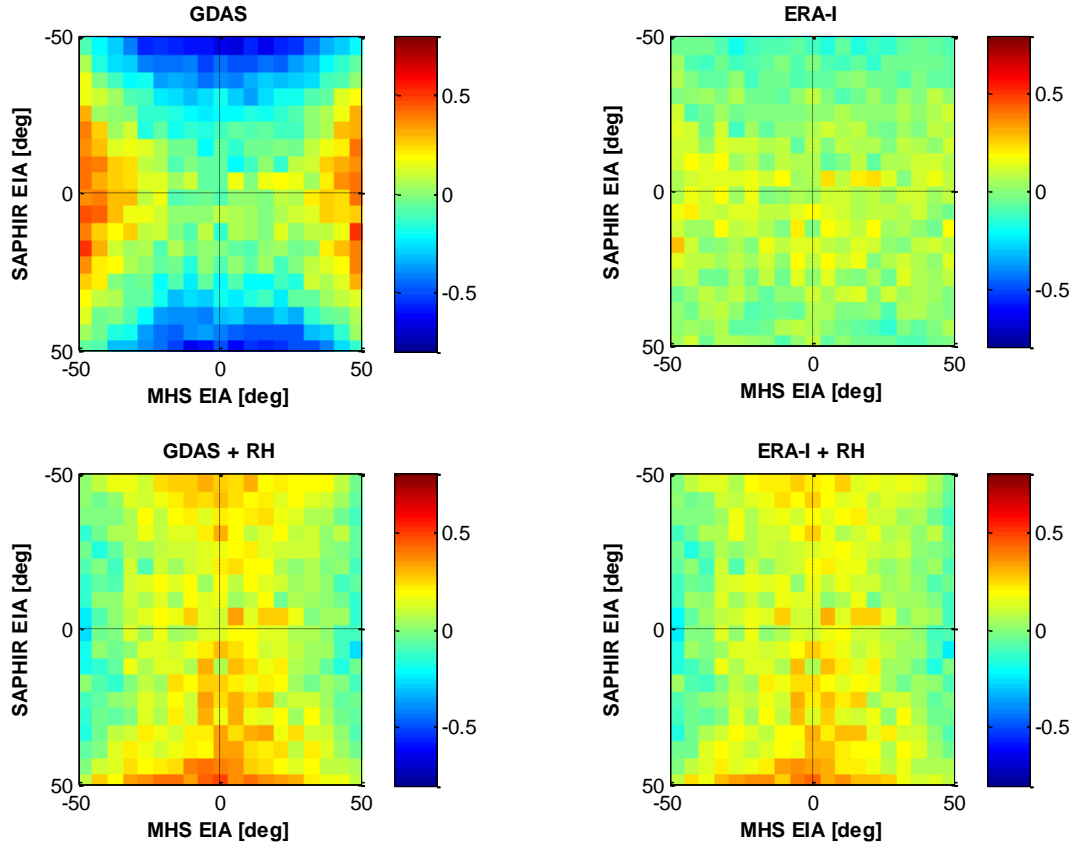


Figure 4-6: Double difference anomaly dependence on earth incidence angle for MHS minus SAPHIR for channel 183.31 ± 1 GHz for various sets of environmental parameters: upper left panel using GDAS, upper right using ERA-I, lower left using GDAS with water vapour profile from SAPHIR retrieved RH, and lower right using ERA-I plus retrieved RH.

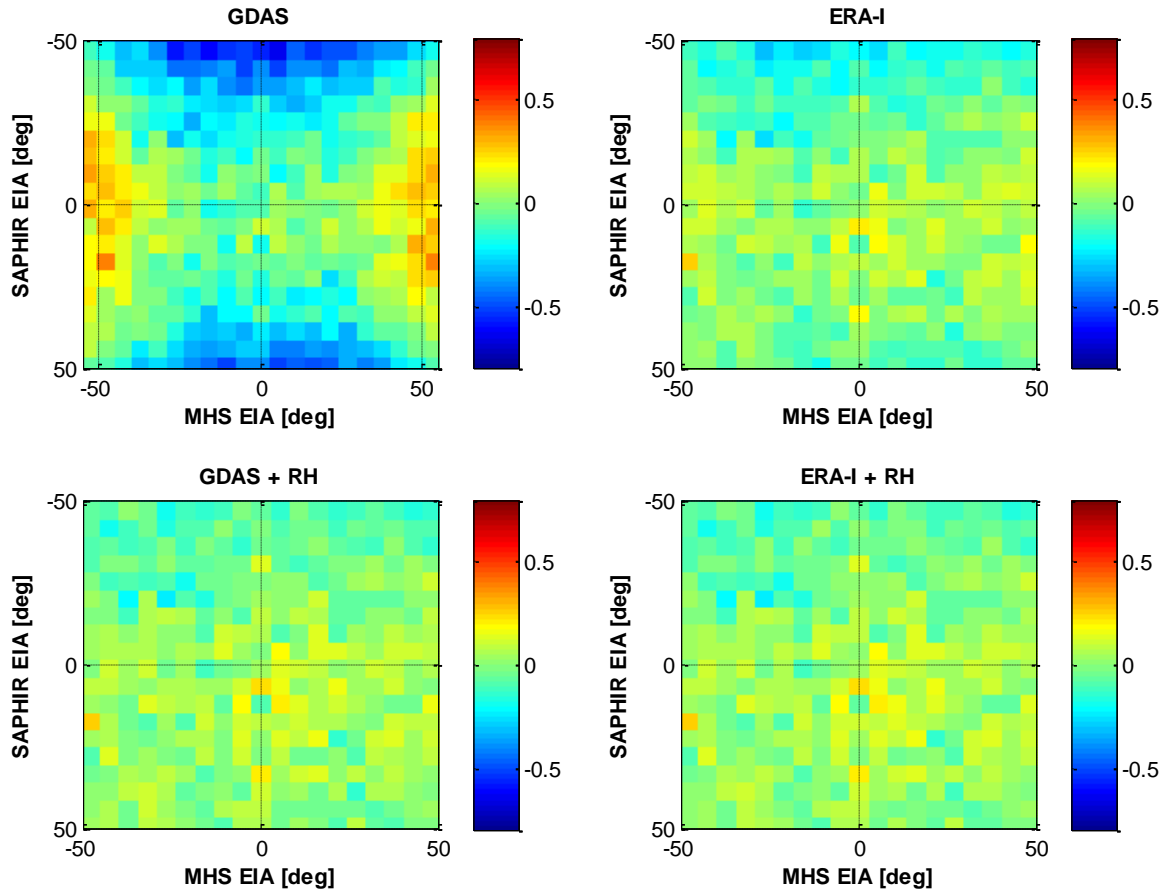


Figure 4-7: Double difference anomaly dependence on earth incidence angle for MHS minus SAPHIR for channel 183.31 ± 3 GHz for various sets of environmental parameters: upper left panel using GDAS, upper right using ERA-I, lower left using GDAS with water vapour profile from SAPHIR retrieved RH, and lower right using ERA-I plus retrieved RH.

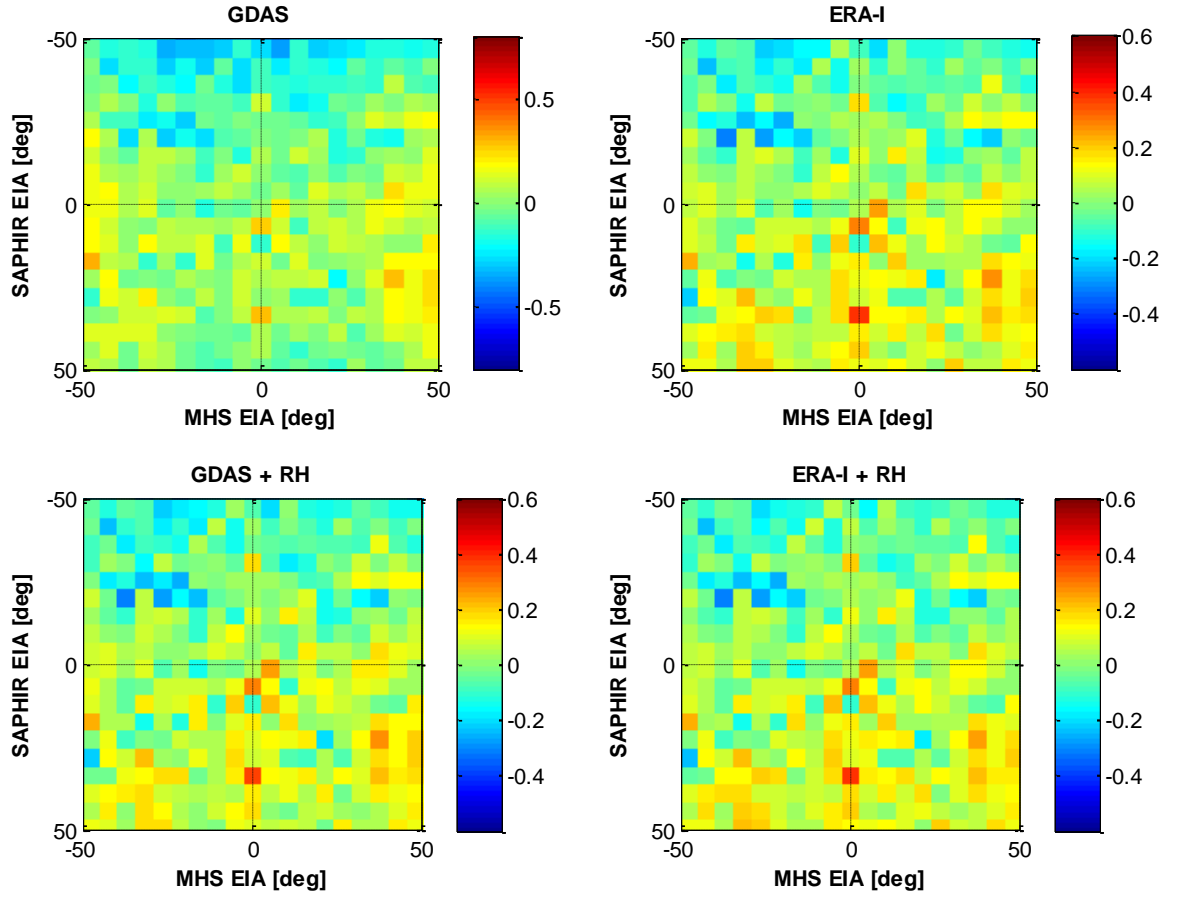


Figure 4-8: Double difference anomaly dependence on earth incidence angle for MHS minus SAPHIR for channel 183.31 ± 7 GHz for various sets of environmental parameters: upper left panel using GDAS, upper right using ERA-I, lower left using GDAS with water vapour profile from SAPHIR retrieved RH, and lower right using ERA-I plus retrieved RH.

Consider first the upper left panel where the DD is evaluated using GDAS environmental parameters. This case exhibits the largest scan angle dependence with a dynamic range of $\sim \pm 0.8$ K. Note that there is an “X” pattern of lower anomaly along the diagonals of the histogram, where the incidence angles of the two sensors are equal. For this condition, each sensor is affected equally by the weighting functions because their slant paths are equal for each

atmospheric layer; and errors, introduced by improper physics and/or an incorrect water vapor profile, become common mode and cancel in the DD. On the other hand, where the EIA's of the sensors differ, especially toward the end of the scan position for one and the nadir for the other, the DD anomalies are the greatest. This is consistent with large SD (observed – modeled) biases resulting from inaccurate water vapor profiles in the upper troposphere, where the weighting functions peak for this channel. Because the SD biases directly depend upon the slant path and because they are different for the two sensors, these effects do not cancel in the DD technique, which is a significant weakness of the procedure for this XCAL application. This is verified by noting the polarity of the anomaly changes depending upon which sensor is viewing nadir (i.e., SAPHIR at nadir produces a positive anomaly, while MHS at nadir produces a negative anomaly).

Next, consider the ERA-I case (upper right panel) where the scan angle dependence is a factor of 4 smaller (DD anomalies are $< \pm 0.2$ K) relative to the nadir position. Here, the (observed – modeled) SD's are smaller, probably because the upper troposphere water vapor profile is closer to reality, and the effect of slant range is effectively removed by the DD.

In the remaining two cases, the SAPHIR retrieved RH profile replaced both the GDAS and ERA-I profiles, and these cases give nearly identical results, as shown in the lower panels. Compared to the upper panels, these cases are better than the GDAS but not quite as good as the ERA-I, and even here there remains a weak “X” pattern of lowest anomaly observed when the sensors EIA match.

Thus, to minimize the scan position dependencies in the biases, it was concluded that the most reliable DD were for collocations, where both sensor slant paths are equal. This was

implemented by restricting the absolute values of the EIA differences of the two sensors to be within $\leq 10^\circ$.

4.3.2 *Individual Matchups vs Binned Average*

In order to perform inter-calibration between two sensors with different properties and characteristics, a careful collocation is required, there are different methods to do the collocations, in our previous studies we have compare two different methods of individual matchups and collocation of binned average data [66], we observed the results from both methods are quite similar and as the computational time for binned average method is considerably lower, we decided to use binned average method.

Moreover, for the imager channels the atmospheric opacity is low, and the surface emission is dominant in the observed temperature, so in the collocations of these channels matching the observations from the same Instantaneous field of view (IFOV) are comparable. In the other hand, in the sounder channels the atmospheric opacity is high, so the position of satellites and the slant path geometries through the atmosphere of the observations are more important

For inter-calibration of SAPHIR and MHS, we have done the collocations using the two methods of binned average, and IFOV matchups. These results for SAPHIR and MHS on board of MetOp-A, NOAA-18, and NOAA-19 have been presented in the following table. It is shown that the comparison of individual match-up's or binned average approaches yield to nearly identical results. Also it is seen that the biases between the different MHS sensors are very small.

Table 4-1: biases between SAPHIR and MHS using the binned average and IFOV matchups methods.

Sensors	M3S2		M4S3		M5S5	
	Binned Avg.	IFOV Match	Binned Avg.	IFOV Match	Binned Avg.	IFOV Match
SAPHIR/MetOp-A	-0.44	-0.32	0.02	0.03	-0.7	-0.67
SAPHIR/NOAA-18	-0.42	-0.27	-0.16	-0.09	-0.56	-0.50
SAPHIR/NOAA-19	-0.79	-0.60	-0.38	-0.19	-0.53	-0.40

As described above, for a cross-track scanner, each antenna scan position has a different Earth incidence angle (EIA) and results in a different slant path through the atmosphere. So, it is important to investigate the changes of radiometric biases with incidence angle. Based upon the instrument designs, it is expected that the biases should be independent of scan angle; therefore if systematic scan angle dependent biases are discovered, it is necessary to characterize and remove such effects.

The biases versus observed Tb have been presented in the Fig. 4-9. Consider first the left hand panel of this figure, where the DD biases for the 183 ± 1 GHz channels are shown. The results show an unexplained systematic increase in the DD biases with the scene temperature, and the biases derived using GDAS water vapor profiles are significantly different that the other three cases, which is consistent with the previous anomaly comparisons.

Next, the center panel shows XCAL comparisons for the 183 ± 3 GHz channels, where the results for the four environmental cases are closer. This may be the result that the Tb weighting functions are lower in altitude where the water vapor profile is better represented by the numerical weather models. While the four cases are in better agreement, never-the-less results

also show a systematic dependence on the scene temperature. When comparing the left-hand and center panels for the cases using the SAPHIR RH retrievals, the results are quite consistent; however, they are not for GDAS and ERA-I cases.

The XCAL results, for radiometer channels well removed from the line resonance (MHS 190 GHz compared to SAPHIR 183 ± 7 GHz) are given in the right-hand panel of Fig. 4-9. Here the four cases are practically identical, and they exhibit a similar increasing dependence on scene temperature but with a larger mean bias (~ 0.7 K).

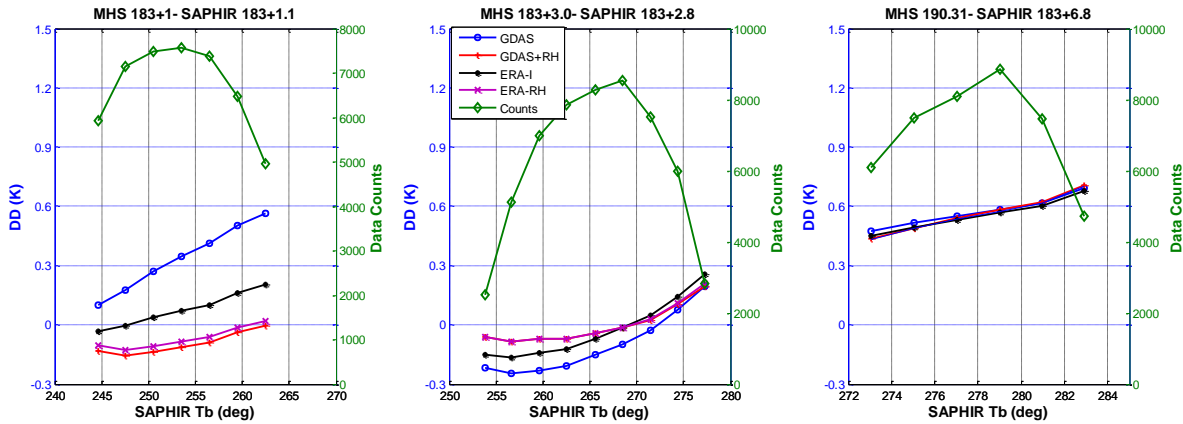


Figure 4-9: Double differences variation with temperature for MHS-SAPHIR with using GDAS, ERA-I, and retrieved RH. The number of data counts at each point has been presented with solid green line and diamond shape.

Finally, additional SAPHIR/MHS XCAL comparisons are presented in Fig. 4-10, where the retrieved RH profile is derived from the collocated GPS-RO data set. For this figure only three environmental cases are shown, namely: GDAS, ERA-I and GPS-RO. Overall these results are similar to those given in Fig. 4-9; however, for the left-hand panel of Fig. 4-10 (183 ± 1 GHz),

the results for ERA-I and GPS-RO are nearly identical, which is because the humidity profiles of GPS-RO, and ERA-I are very similar to each other [76].

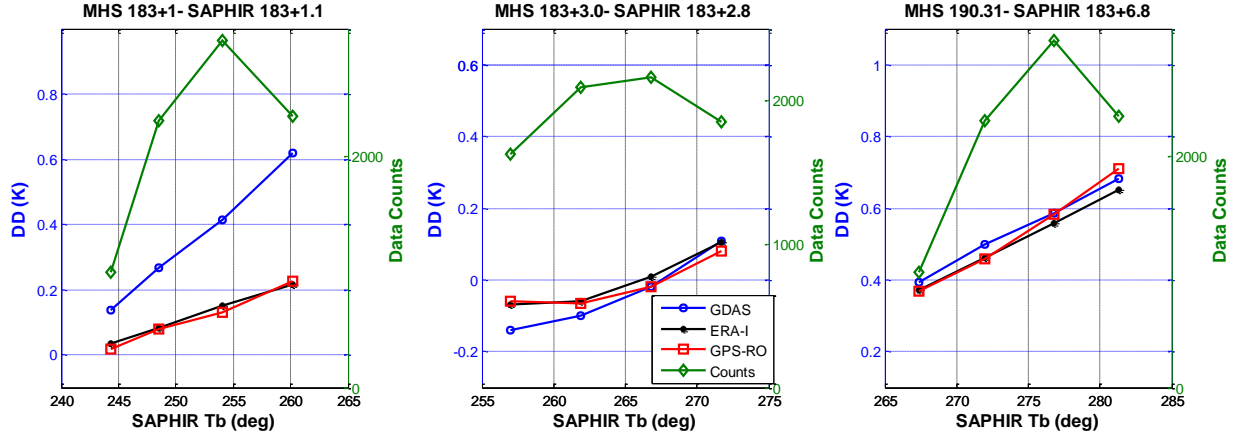


Figure 4-10: Double differences variation with temperature for MHS-SAPHIR with using GDAS, ERA-I, and GPS-RO profiles. The number of data counts at each point has been presented with solid green line and diamond shape.

4.3.2.1 SAPHIR with ATMS

In a similar manner as above, the XCAL biases for ATMS relative to SAPHIR were analyzed, and the corresponding results are presented in Fig. 4-11, as a function of the SAPHIR scene brightness. Starting with the upper left and middle panels, the SAPHIR channel 183 ± 1 GHz is compared with the ATMS 183 ± 1 GHz, and 183 ± 1.8 GHz channels respectively for the four environmental cases, namely: GDAS, ERA-I, and with the SAPHIR retrieved RH profiles. These DD results are very similar to the SAPHIR/MHS results presented in Fig. 4-9.

As the radiometer channel frequency moves progressively from the resonant line (e.g., 183 ± 3 GHz upper right panel, 183 ± 4.5 lower left panel and 183 ± 7 GHz lower middle panel), the DD

biases progressively converge for the four cases and become nearly identical. The reason for this is that the weighting functions in the upper troposphere are less important for these channels, and apparently the water vapor profiles are similar for the three cases.

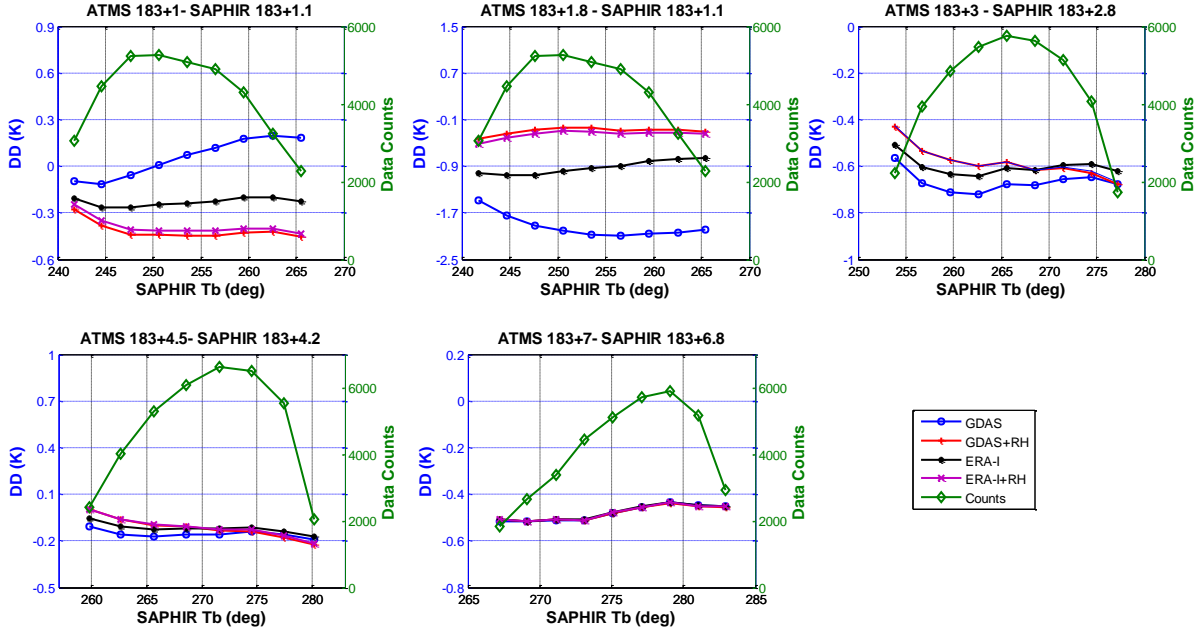


Figure 4-11: Double differences variation with temperature for ATMS-SAPHIR with using GDAS, ERA-I, and retrieved RH. The number of data counts at each point has been presented with solid green line and diamond shape.

4.3.2.2 ATMS with MHS

The results for inter-calibration between ATMS and MHS are presented in Fig. 4-12. It should be mentioned that these are the biases resulting from triple matchups of SAPHIR, MHS, and ATMS within ± 30 deg latitude. Since both MHS and ATMS operate on polar orbiting satellites, most matchups occur in high latitude, where the total precipitable water is considerably lower. For these cases, the influence of the surface emission is not negligible, and therefore the DD biases

are less reliable. However, using the triple difference method with respect to SAPHIR, we are able to obtain the calibration bias between these two sensors in the tropical latitudes.

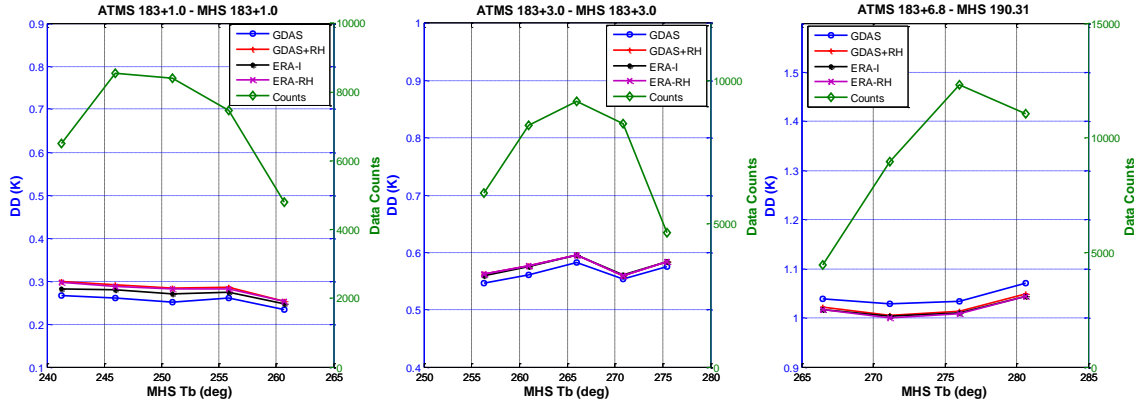


Figure 4-12: Double differences variation with temperature for ATMS-MHS with using GDAS, ERA-I, and retrieved RH. The number of data counts at each point has been presented with solid green line and diamond shape.

4.3.3 MHS with MHS

Here MetOp-A is used as transfer standard, and the biases between MetOp-B and NOAA-18, and NOAA-19 has been measured for 2015. Because the MHS radiometers on these satellites are almost identical, the biases can be calculated with the single differences approach for the collocations with the same incidence angle. But, we measure the biases using the Double Difference technique to eliminate or decrease the incidence angle dependence. In the cross track scanning sensors, there is significant dependence between temperature and the Earth Incidence Angle, as shown in Fig. 4-13. Figure 4-14 shows the DD anomalies for the corresponding pixels, from which it's clear that the biases for all the channels are almost independent of the scan position, with the 89GHz channel showing the higher EIA dependence.

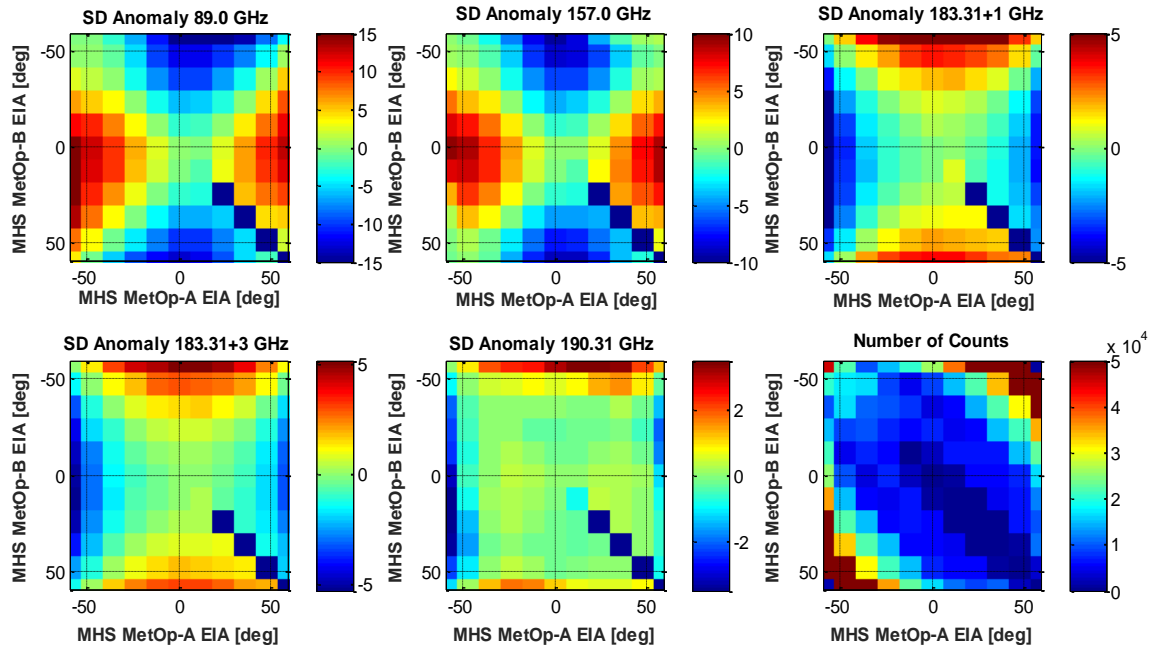


Figure 4-13: Single difference anomaly dependence on earth incidence angle for MHS on board of MetOp-B minus MHS on board of MetOp-A for the corresponding five channels, and number of counts for each pixels.

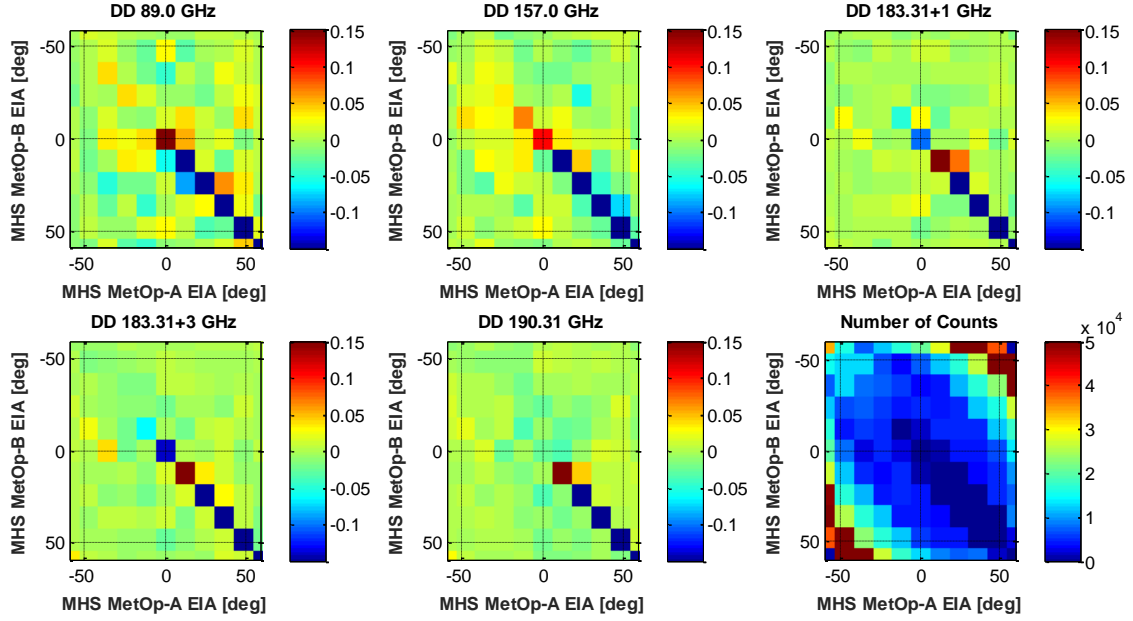


Figure 4-14: Double difference anomaly dependence on earth incidence angle for MHS on board of MetOp-B minus MHS on board of MetOp-A for the corresponding five channels, and number of counts for each pixels.

The biases variation with latitude was also illustrated in Fig. 4-15. This figure presents a normalized density plot, where the solid black line represents the linear fit. We have not observed any regional dependence. We find that the biases are very small, and do not variate with the latitude changes.

A similar analysis was performed for the biases between Metop-A-NOAA-18, and Metop-A-NOAA-19. But the number of the collocation points is far less than MetOp-A-MetOp-B matchups; for this reason, we only performed matchups over the Polar Regions. From our analysis, we find that the variation as a function of EIA, and latitude are negligible as well. The average values and the uncertainties of the biases for these sensors for the dataset over 2015, is

presented in the Table 5. This results show that the biases are less than 0.5 Kelvin for all the channels; particularly, the biases between MetOp-A and MetOp-B are very small.

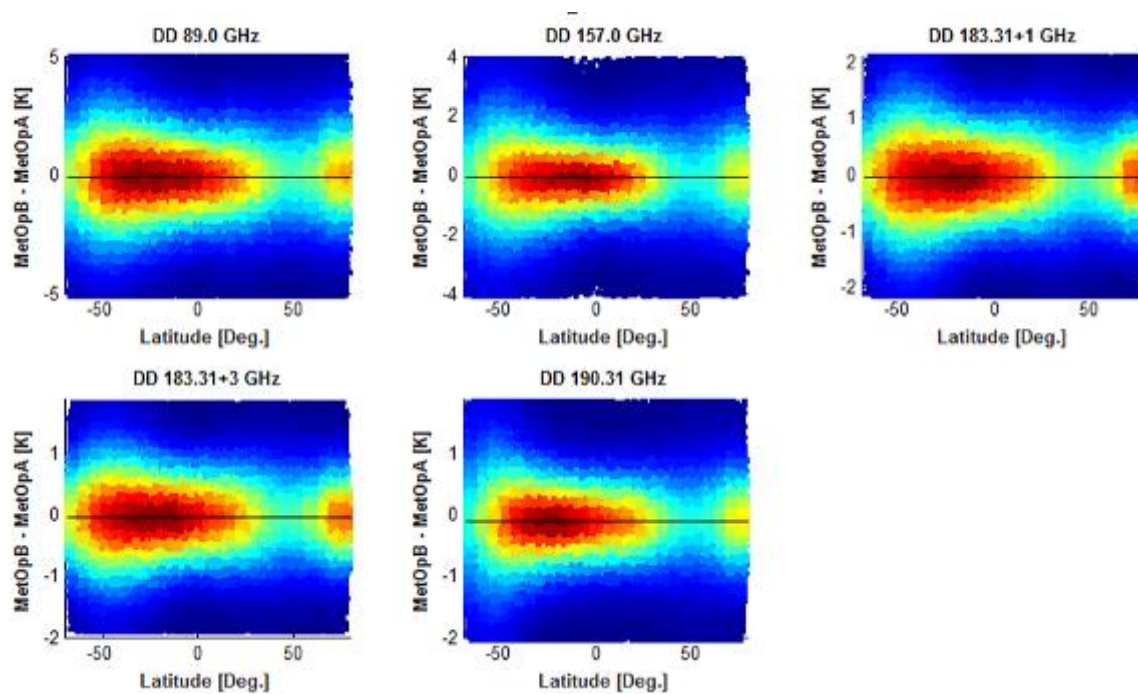


Figure 4-15: MetOp-B – MetOp-A biases changes with latitude.

Table 4-2: biases between MHS sensors for 2015

CHANNELS	89QV	157QV	183.31± 1.0QH	183.31± 3.0QH	183.31± 7.0QH
MetOp_A - MetOp_B	0.12±1.71	-0.09±0.9	0.01±0.43	-0.03±0.54	0.04±0.46
MetOp_A – NOAA18	-0.42±2.9	-0.11±2.4	0.13±1.9	0.06±0.80	0.07±0.43
MetOp_A - NOAA19	0.46±3.1	0.31±1.2	0.23±2.1	0.06±0.23	0.36±0.45

4.3.4 MHS with AMSU-B

Continuing our analysis, the biases between MHS on board of MetOp-A and AMSU-B on board of NOAA-17 for 2009 were measured. In the first step, the dependence of the biases with changes of EIAs was investigated, and the results are presented in Fig 4-16. Biases for all the channels are almost independent of the scan position; except for the 89 GHz channel, where variations around ± 0.2 K were observed. The reason for these variations is in the discrepancies between observed brightness temperatures in AMSU-B with the modeled brightness temperature. Further investigation is needed, but beyond the scope of this paper. The DDs between MHS on MetOp-B and AMSU-B on board of NOAA-17 for 2009 are presented in Table 6. The biases are larger than for MHS sensors, having larger uncertainties. These results are preliminary, and more analysis is needed in order to determine the final values for the biases.

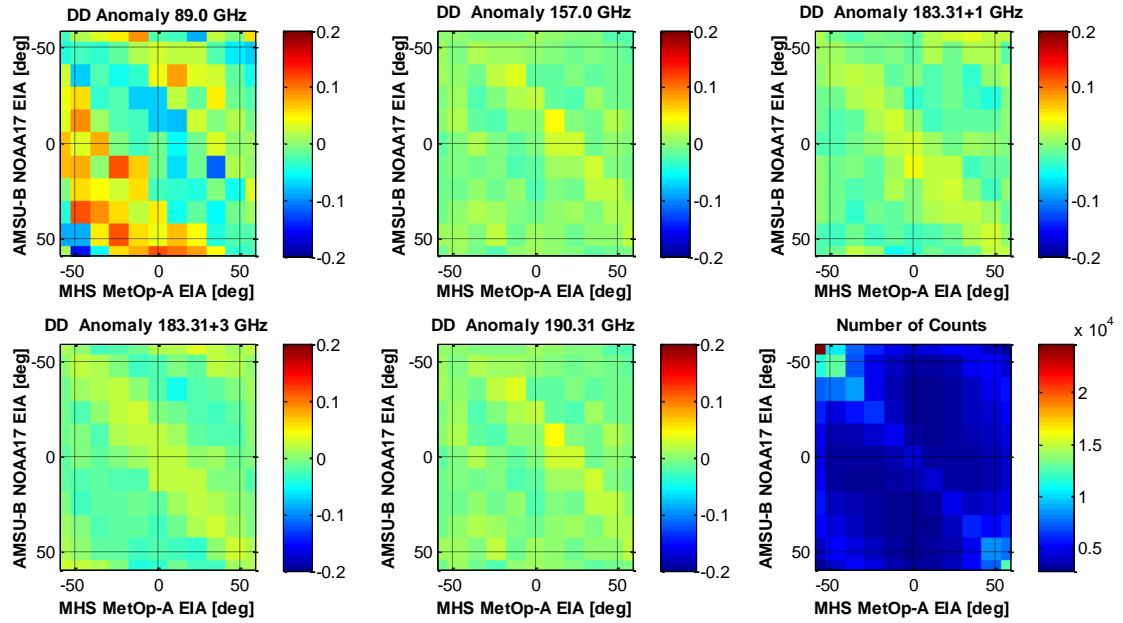


Figure 4-16: Double difference anomaly dependence on earth incidence angle for AMSU-B on board of NOAA17 minus MHS on board of MetOp-A for the corresponding five channels, and number of counts for each pixels.

Table 4-3: Biases between MHS on MetOp-A and AMSU-B on board of NOAA-17 for 2009.

CHANNELS	89QV	157QV	183.31± 1.0QH	183.31± 3.0QH	183.31± 7.0QH
MetOp_A – NOAA17	0.72±2.71	-0.86±1.9	0.51±0.43	-0.31±0.42	0.24±0.36

4.4 Conical Scanner with Cross Track Scanner

4.4.1 GMI with MHS

In the GPM constellation, the required consistency in the input brightness temperatures is accomplished by inter-calibrating the constellation radiometers using the GPM Microwave

Imager (GMI) as the calibration reference [77]. MHS radiometers, as part of GPM constellation, have been calibrated with GMI as well. It should be considered in the cross track scanners the polarization of the Tbs changes with the scan position that it's a mixture of vertical and horizontal polarizations. The full descriptions of the calibration technique can be found in Berg et al. [78]. In Fig. 4-17, the double differences as a function of MHS EIAs are presented. From this figure, it is noticeable that the 89 GHz has the largest variations, and these decreases in the channels with higher frequencies. The average values of the biases are shown with solid black line; the averages are very small for all the channels, which show that MHS and GMI are in a good agreement. Also, Fig. 4-18 illustrates the variations of the biases with the latitude. The average values of the biases are shown with solid black line; which is not changing with the latitude, and it shows are biases are not changing with the spatial changes. Also, the results of biases for the all the MHS sensors is presented in Table 4.

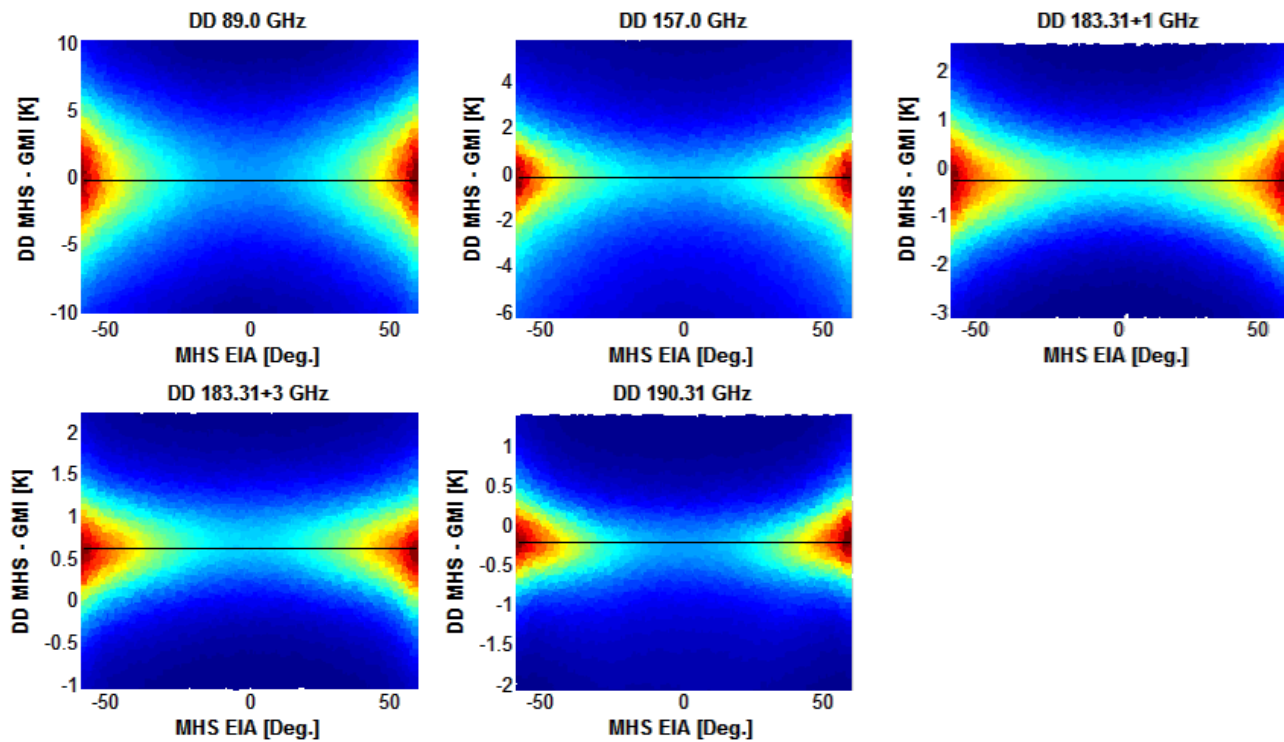


Figure 4-17: Double difference dependence on earth incidence angle for MHS on board of MetOp-B minus GMI for the corresponding five channels.

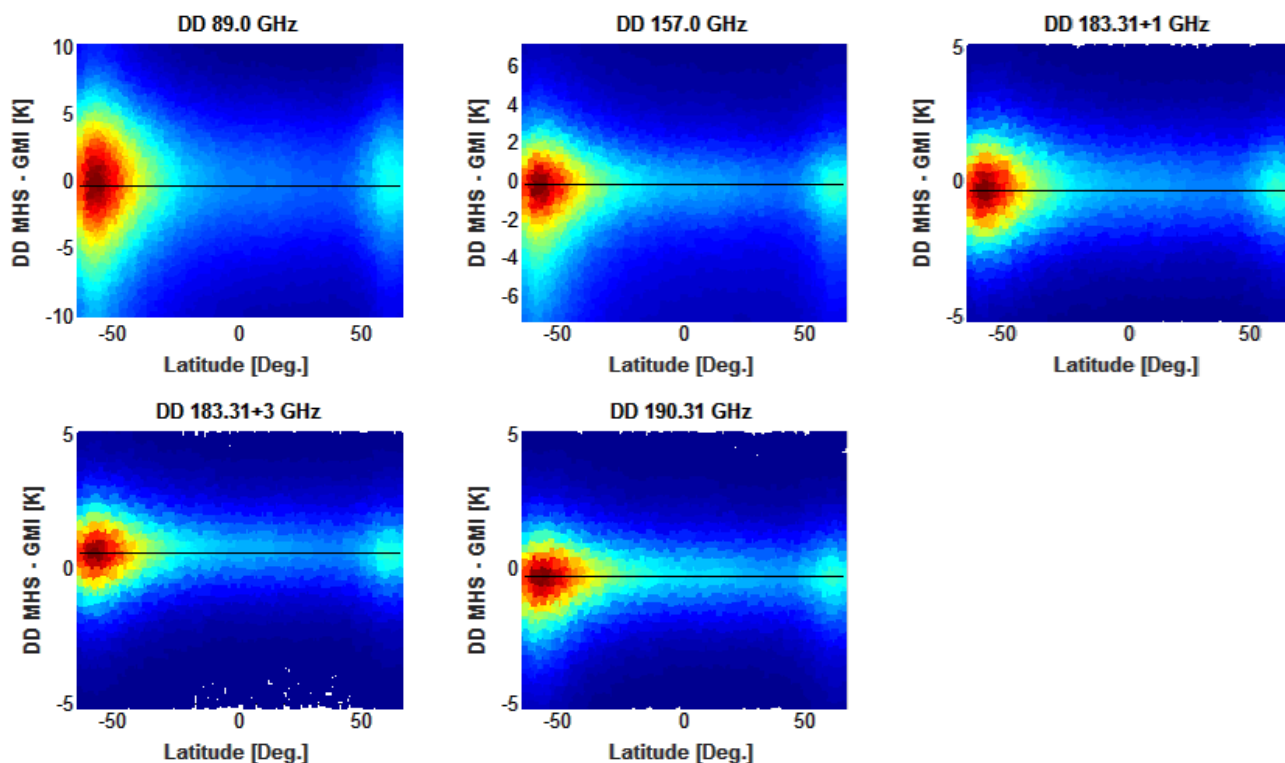


Figure 4-18 :Double difference dependence on the earth latitude for MHS on board of MetOp-B minus GMI for the corresponding five channels.

Table 4-4: biases between GMI and MHS sensors for 2015.

CHANNELS	89QV	157QV	183.31± 1.0QH	183.31± 3.0QH	183.31± 7.0QH
MetOp_A - GMI	0.43±2.20	-0.41±1.2	0.16±1.4	-0.31±0.57	-0.25±0.44
MetOp_B - GMI	0.38±1.17	-0.47±1.0	0.06±1.6	-0.35±0.56	0.22±0.43
NOAA18 - GMI	-0.04±1.25	-0.23±1.2	0.52±1.4	0.10±0.56	0.21±0.41
NOAA19 - GMI	-0.08±1.2	-0.48±1.1	0.26±1.5	-0.02±0.54	0.23±0.45

4.4.1.1 SSMIS with SAPHIR

Before launch of GPM on February 2014, SAPHIR has been used for calibration of SSMIS. The dataset used for this analysis is level 1C data of SSMIS and 1Base data of SAPHIR from July to December of 2012. Table 1 shows the corresponding channels of the SSMIS and SAPHIR with their central frequency and bandwidth. The first step is the comparison of the measured brightness differences between sensors. The observed brightness temperature comparison for SAPHIR and SSMIS (183 ± 3 GHz channel) is shown in Fig. 4-19 for 3 DMSP satellites (F16, F17 and F18). Based upon these scatter diagrams, the comparison is best for SSMIS on F18. Further, the Double Differences for F18 exhibit a slight variability with time as shown in Fig. 4-20.

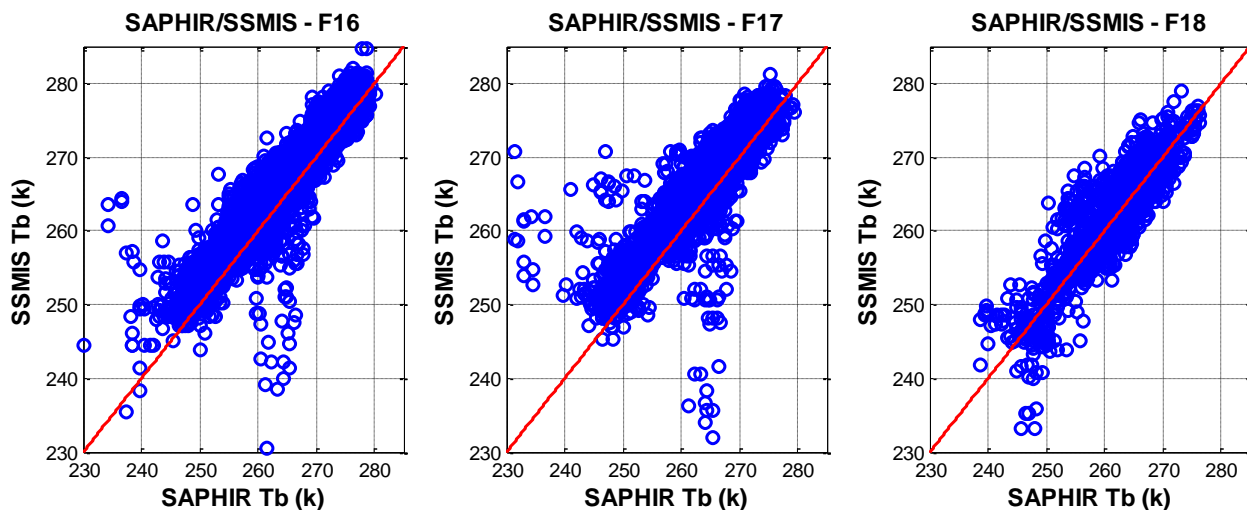


Figure 4-19: Observed brightness temperature comparisons for SAPHIR and SSMIS for the 183 ± 3 GHz channel for F16, F17 and F18 [66].

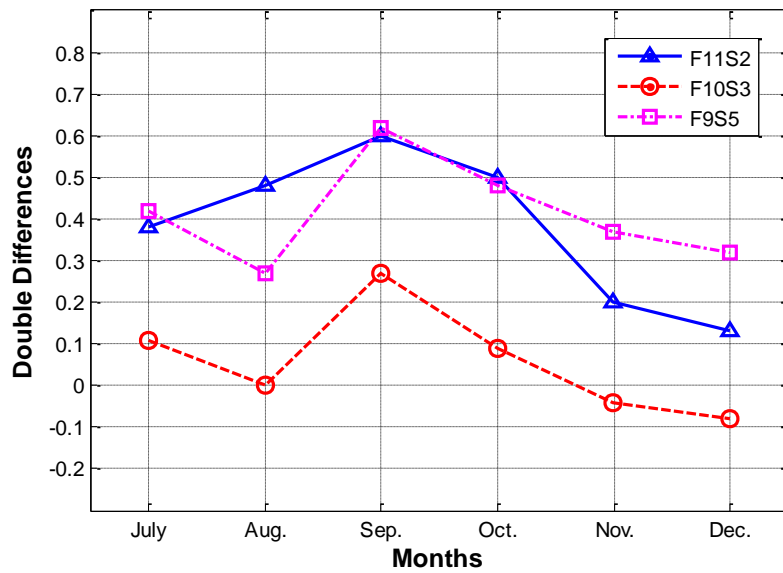


Figure 4-20: Double Differences values for F18 for six months [66].

Finally, the corresponding six-month average value of the Double Differences for F16, F17 and F18, for both Binned Average and IFOV Match-up methods, are presented in Table 4-6. A close examination shows that the results for both methods are quite similar.

Table 4-5: Average Double Differences values for different satellites for both Binned Average and IFOV Match-ups methods [66].

Satellites	183±1 GHz		183±3 GHz		183±7 GHz	
	Binned Average	IFOV Matchup	Binned Average	IFOV Matchup	Binned Average	IFOV Matchup
F16	-1.59	-1.51	-0.86	-0.69	-0.45	-0.35
F17	-1.25	-0.78	-0.10	0.23	1.31	1.57
F18	0.40	0.31	0.06	0.52	0.41	0.71

4.4.1.2 GMI with SAPHIR

The Tb dataset used for this study are; 1Base files GMI version ITE030 and SAPHIR, version V02A data from March to December 2014. SAPHIR is a cross-track scanner, so each antenna scan position has a different Earth incidence angle (EIA) and a different slant path through the atmosphere. In inter-comparison of SAPHIR with a conical scanner like GMI, it is important to investigate the changes of biases with incidence angle. Figure 4-21 shows the changes of GMI-SAPHIR biases versus incidence angle for Rosenkranz model using GDAS and ERA-I geophysical data, and ERA-I with retrieved Relative Humidity. As it is shown in this figure, when using GDAS dataset, changes of EIA result in the DDs varying by 0.6 K for 183+3 and by 0.3 K for 183+7 channel. On the other hand, when using the ERA-I data, these changes respectively decrease to 0.3 and 0.2 K. also it can be seen because of the asymmetry in SAPHIR dataset, results are not symmetric as it is expected.

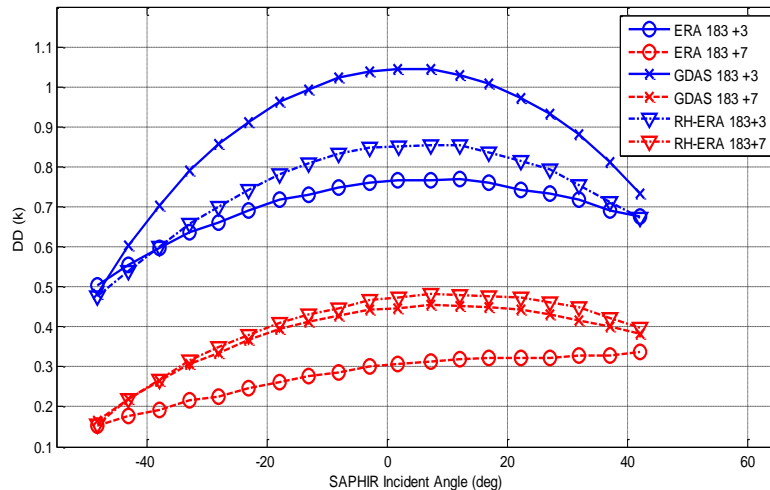


Figure 4-21: Double differences dependence on Incidence angle for GMI-SAPHIR with using GDAS and ERA.

Also, it is noted that the value of double differences slightly increases with scene brightness temperature as shown in Fig. 4-22. When using GDAS and ERA-I, changes of DDs are almost linear with increasing T_b .

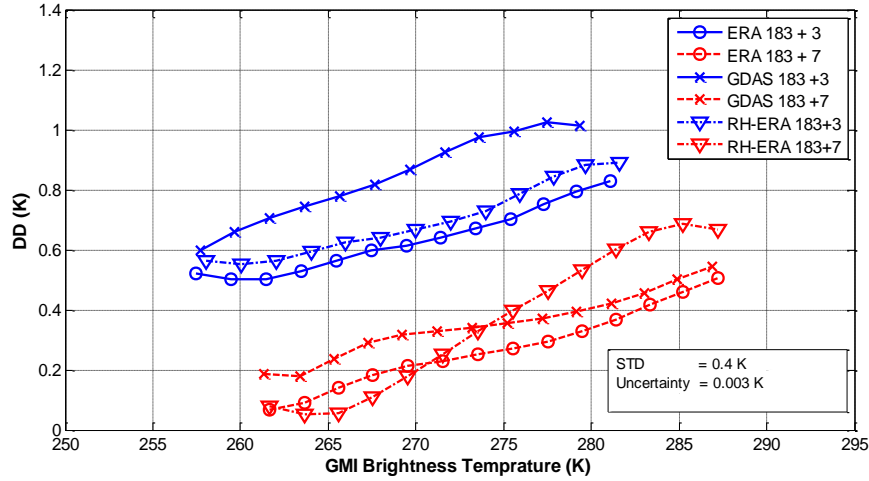


Figure 4-22: Double differences variation with temperature for GMI-SAPHIR with using GDAS and ERA.

Changes of biases over time are shown in Fig. 4-23. The upper panel shows the values of DDs, where 183 ± 3 GHz are represented by blue and 183 ± 7 GHz with red symbols. The second panel presents changes of the satellite direction of flight (yaw 0° or 180°) for GPM and Megha-Tropique, which occur periodically in time. Fortunately, the DDs are independent of the respective satellite yaw angles; however at the time of the yaw flip, we see small “jumps on DDs”. Also on the 180th of 2014, DDs have a peak, which is because the EIA of SAPHIR is close to Nadir, and it is shown in Fig. 4-1 that DD maximizes at EIA equal to zero.

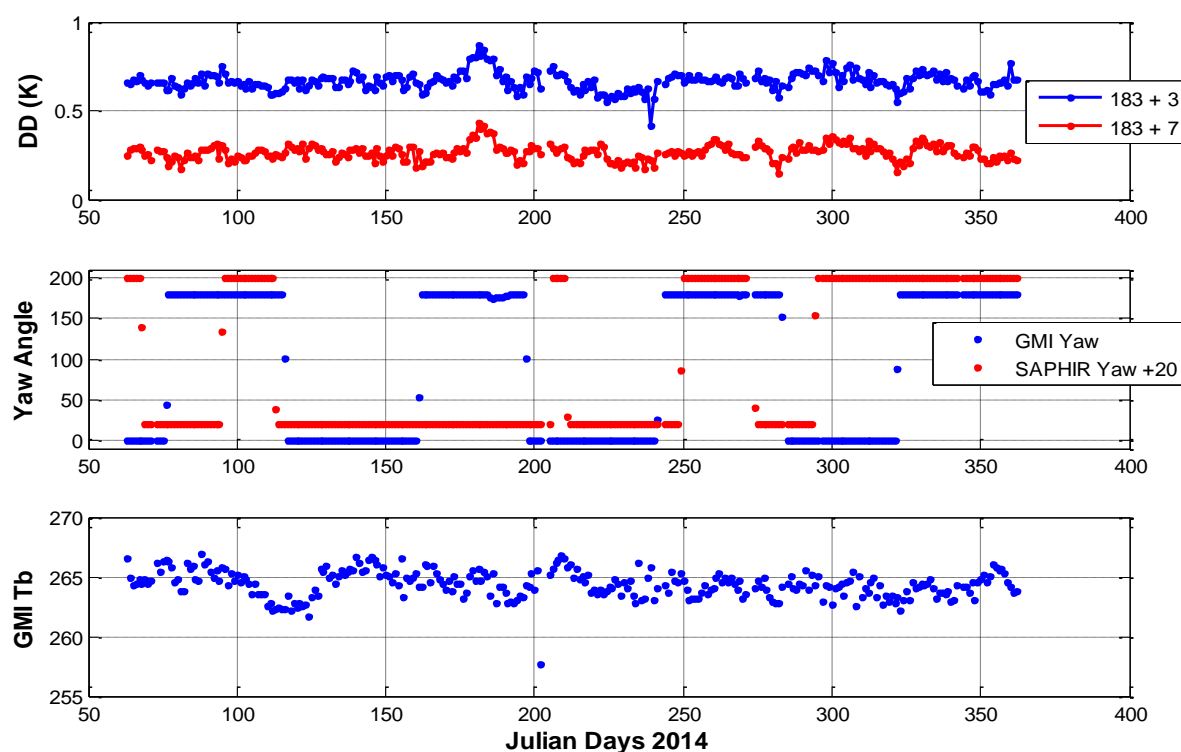


Figure 4-23: variation of biases with time for 2014 [79].

Although the changes in DD with incidence angle are not high, never-the-less to improve the comparison, the matchups are selected where the differences between EIA's are within 2 degree. The calculated DDs for both GDAS and ERA-I for RSS and Elsasser emissivity models are presented in Table 1. The changes in DD biases are less than 0.05 K for the selected data.

Table 4-6: Double differences using Rosencranz, MonoRTM with GDAS and ERA-I [79].

RTM model	Channels	GDAS	ERA
Rosencranz	183.3 \pm 3.0 GHz	0.58 \pm 0.56	0.59 \pm 0.53
	183.3 \pm 7.0 GHz	0.31 \pm 0.53	0.29 \pm 0.45
MonoRTM	183.3 \pm 3.0 GHz	0.53 \pm 0.64	0.54 \pm 0.65
	183.3 \pm 7.0 GHz	0.28 \pm 0.51	0.23 \pm 0.52

CHAPTER 5: CONCLUSION AND SUMMARY

Previously CFRSL developed a “double difference” technique for the inter-satellite radiometric calibration (XCAL) of conical scanning microwave imaging radiometers in support of NASA’s Global Precipitation Measurement Mission (GPM). While this DD technique was quite robust and successful for the conical scan geometry, unfortunately, the casual application for cross-track millimeter sounders has definite limitations that were uncovered during the conduct of this dissertation.

First, for conical imagers, the majority of emission comes from the surface and lower atmosphere, and the slant path through the atmosphere is fixed independent of the azimuth scan angle. Even when the two radiometers have different EIA’s, there is a finite but constant differential path length that is independent of azimuth scan angle. If the numerical weather model (NWM) environmental parameters are good estimates of the true values, then the effect of the differential path length is exactly captured in the simulated single difference. On the other hand, if the environmental parameters are not representative of the true values, then the effects of path length will only partially cancel and contribute a bias error in the DD results. Our procedure of using two different NWM results provides an estimate of this uncertainty by calculating the mean and standard deviation between the DD biases for these different cases.

For sounders the situation is more complicated for two reasons. First, when comparing match-up between radiometers, there is a large variance in their scan angles, which results in a wide range of differential propagation path lengths that are proportional to the differential scan angle between the two radiometers. Second, this may not be an issue if the water vapor profile is well

known, but unfortunately, the majority of sounder radiances come from the troposphere, where there is large uncertainty in the water vapor profile between NWM's. As a result, the effect of differential path length on the simulated radiances does not usually cancel in the double difference comparison. Compared to imager XCAL, the sounders have larger errors associated with the DD biases that are variable with scan geometry i.e., that are functions of both the scan angle and the differential path length.

To understand these issues, a wide variety of match-up combinations were evaluated (see Chap-4), and this dissertation presented results for the radiometric biases between different pair of sounding radiometers that exhibited a dependence upon scan angle. Further, the magnitude of these biases were also dependent upon the source of atmosphere humidity profiles used. Therefore, for channels near the 183 GHz water vapor absorption line peak, it was concluded that reliable XCAL comparisons can be made only when the path lengths of the two sensors are approximately equal, which is accomplished by restricting the EIA differences to a small value.

Further, it is important to mention that matching the scan angles for the two radiometers, significantly reduces the sensitivity of the radiometric bias to the assumed water vapor profile, but it is not eliminated. Particularly, there remains is a significant difference between XCAL results using GDAS and ERA-I environmental data for 183 ± 1 GHz channel.

On the other hand, when incorporating the water vapor profiles retrieved from the GPS-RO technique into the NWM's, the results for ERA-I and GPS-RO are nearly identical, and show significantly reduced sensitivity to scan angle. Further, the XCAL biases are not sensitive to the choice of other environmental parameters, which is highly desired. This implies that for sounders

(especially near the 183 GHz absorption line), the DD technique yields different biases depending upon the incorrect water vapor profiles.

Finally, when restricting the sounder radiometers to match scan angle and when using the SAPHIR retrieved relative humidity or the GPS-RO water vapor profiles in the troposphere, there is high confidence in the XCAL biases for all sounder channels. Thus, using measured water vapor profiles within the troposphere significantly improves the DD results.

FUTURE WORK: This dissertation provides the basis for inter-calibration of all the sounder channels since the start of TRMM mission, and future work will focus on applying the presented techniques to all the AMSU-B, and MHS radiometers on board of NOAA satellites, and thereby provide a consistent measurement from 1998 up to present in near future.

Also, this work can be extended to the future missions, such as upcoming The Time-Resolved Observations of Precipitation structure and storm Intensity with a Constellation of Smallsats (TROPICS) mission. It consists of a constellation of CubeSat's with three channels near the 183.31 GHz water vapor channels.

REFERENCES

1. SPACE, G. and F. CENTER, *PRECIPITATION MEASUREMENT MISSIONS*.
2. Ulaby, F.T., et al., *Microwave radar and radiometric remote sensing*. 2014: University of Michigan Press Ann Arbor.
3. *History of microwave radiometer measurements*. Available from: http://gop.meteo.uni-koeln.de/ag_crewell/doku.php?id=instruments:hatpro:hatpro.
4. Czekala, H., et al., *Discrimination of cloud and rain liquid water path by groundbased polarized microwave radiometry*. Geophysical Research Letters, 2001. **28**(2): p. 267-270.
5. Bennartz, R. and P. Bauer, *Sensitivity of microwave radiances at 85–183 GHz to precipitating ice particles*. Radio Science, 2003. **38**(4).
6. Kneifel, S., et al., *Snow scattering signals in ground-based passive microwave radiometer measurements*. Journal of Geophysical Research: Atmospheres, 2010. **115**(D16).
7. Moradi, I., et al., *Correcting geolocation errors for microwave instruments aboard NOAA satellites*. Geoscience and Remote Sensing, IEEE Transactions on, 2013. **51**(6): p. 3625-3637.
8. Blackwell, W.J., et al. *On-orbit radiometric validation and field-of-view calibration of spaceborne microwave sounding instruments*. in *Asia-Pacific Remote Sensing*. 2008. International Society for Optics and Photonics.
9. John, V.O., et al., *Assessment of intercalibration methods for satellite microwave humidity sounders*. Journal of Geophysical Research: Atmospheres, 2013. **118**(10): p. 4906-4918.
10. Wentz, F.J., *A well-calibrated ocean algorithm for special sensor microwave/imager*. Journal of Geophysical Research: Oceans, 1997. **102**(C4): p. 8703-8718.
11. Yan, B. and F. Weng, *Intercalibration between special sensor microwave imager/sounder and special sensor microwave imager*. IEEE Transactions on Geoscience and Remote Sensing, 2008. **46**(4): p. 984-995.
12. Yang, G.-P., et al., *Temporal and spatial variations of dimethylsulfide (DMS) and dimethylsulfoniopropionate (DMSP) in the East China Sea and the Yellow Sea*. Continental Shelf Research, 2011. **31**(13): p. 1325-1335.
13. Sapiiano, M.R., et al., *Toward an intercalibrated fundamental climate data record of the SSM/I sensors*. IEEE Transactions on Geoscience and Remote Sensing, 2013. **51**(3): p. 1492-1503.

14. Wentz, F.J., P. Ashcroft, and C. Gentemann, *Post-launch calibration of the TRMM microwave imager*. IEEE Transactions on Geoscience and Remote Sensing, 2001. **39**(2): p. 415-422.
15. Wentz, F.J., *A 17-Yr Climate Record of Environmental Parameters Derived from the Tropical Rainfall Measuring Mission (TRMM) Microwave Imager*. Journal of Climate, 2015. **28**(17): p. 6882-6902.
16. Wilheit, T.T., *Comparing calibrations of similar conically scanning window-channel microwave radiometers*. Geoscience and Remote Sensing, IEEE Transactions on, 2013. **51**(3): p. 1453-1464.
17. John, V.O., et al., *Understanding intersatellite biases of microwave humidity sounders using global simultaneous nadir overpasses*. Journal of Geophysical Research: Atmospheres, 2012. **117**(D2).
18. Hong, L., *Inter-satellite microwave radiometer calibration*. 2008: ProQuest.
19. Hou, A.Y., et al., *The global precipitation measurement mission*. Bulletin of the American Meteorological Society, 2014. **95**(5): p. 701-722.
20. Michaelides, S.C., *Precipitation: advances in measurement, estimation and prediction*. 2008: Springer Science & Business Media.
21. Berg, W., et al., *Intercalibration of the GPM Microwave Radiometer Constellation*. Journal of Atmospheric and Oceanic Technology, 2016(2016).
22. Biswas, S.K., et al., *Intercalibration of microwave radiometer brightness temperatures for the global precipitation measurement mission*. Geoscience and Remote Sensing, IEEE Transactions on, 2013. **51**(3): p. 1465-1477.
23. Gopalan, K., et al., *A time-varying radiometric bias correction for the TRMM microwave imager*. Geoscience and Remote Sensing, IEEE Transactions on, 2009. **47**(11): p. 3722-3730.
24. Meissner, T., F. Wentz, and D. Draper, *GMI calibration algorithm and analysis theoretical basis document*. Remote Sensing Systems, 2009: p. 1-110.
25. Zou, X., et al., *A ray-tracing operator and its adjoint for the use of GPS/MET refraction angle measurements*. Journal of Geophysical Research: Atmospheres, 1999. **104**(D18): p. 22301-22318.
26. Meissner, T. and F.J. Wentz, *The emissivity of the ocean surface between 6 and 90 GHz over a large range of wind speeds and earth incidence angles*. Geoscience and Remote Sensing, IEEE Transactions on, 2012. **50**(8): p. 3004-3026.
27. Elsaesser, G.S., *A parametric optimal estimation retrieval of the non-precipitating parameters over the global oceans*. 2006, Colorado State University.

28. Liebe, H., P. Rosenkranz, and G. Hufford, *Atmospheric 60-GHz oxygen spectrum: New laboratory measurements and line parameters*. Journal of quantitative spectroscopy and radiative transfer, 1992. **48**(5): p. 629-643.
29. Rosenkranz, P.W., *Water vapor microwave continuum absorption: A comparison of measurements and models*. Radio Science, 1998. **33**(4): p. 919-928.
30. NCEP, F., *operational model global tropospheric analyses, continuing from July 1999*. Research Data Archive at the National Center for Atmospheric Research, Computational and Information Systems Laboratory, Boulder, CO. Available: <http://rda.ucar.edu/datasets/ds083>. **2**.
31. Dee, D., et al., *The ERA-Interim reanalysis: Configuration and performance of the data assimilation system*. Quarterly Journal of the Royal Meteorological Society, 2011. **137**(656): p. 553-597.
32. *NCEP (National Centers for Environmental Prediction) FNL (Final) Operational Global Analyses*.
33. Steele, M., R. Morley, and W. Ermold, *PHC: A global ocean hydrography with a high-quality Arctic Ocean*. Journal of Climate, 2001. **14**(9): p. 2079-2087.
34. Studio, N.S.V. *Aquarius Sea Surface Salinity Flat Maps 2012* Available from: <https://svs.gsfc.nasa.gov/4233>.
35. Meissner, T. and F.J. Wentz, *The complex dielectric constant of pure and sea water from microwave satellite observations*. IEEE Transactions on Geoscience and Remote Sensing, 2004. **42**(9): p. 1836-1849.
36. Yang, J.X., *Spaceborne microwave radiometry: Calibration, intercalibration, and science applications*. 2016, The University of Michigan.
37. Payne, V.H., et al., *Air-broadened half-widths of the 22-and 183-GHz water-vapor lines*. IEEE Transactions on Geoscience and Remote Sensing, 2008. **46**(11): p. 3601-3617.
38. Kakar, R.K., *Retrieval of clear sky moisture profiles using the 183 GHz water vapor line*. Journal of Climate and Applied Meteorology, 1983. **22**(7): p. 1282-1289.
39. Wang, J. and L. Chang, *Retrieval of water vapor profiles from microwave radiometric measurements near 90 and 183 GHz*. Journal of Applied Meteorology, 1990. **29**(10): p. 1005-1013.
40. Wilheit, T.T., *An algorithm for retrieving water vapor profiles in clear and cloudy atmospheres from 183 GHz radiometric measurements: Simulation studies*. Journal of Applied Meteorology, 1990. **29**(6): p. 508-515.

41. Sivira, R., et al., *A layer-averaged relative humidity profile retrieval for microwave observations: design and results for the Megha-Tropiques payload*. Atmospheric Measurement Techniques, 2015. **8**(3): p. 1055-1071.
42. Brogniez, H., et al., *Estimating Confidence Intervals around Relative Humidity Profiles from Satellite Observations: Application to the SAPHIR Sounder*. Journal of Atmospheric and Oceanic Technology, 2016. **33**(5): p. 1005-1022.
43. Hong, G., et al., *Detection of tropical deep convective clouds from AMSU-B water vapor channels measurements*. Journal of Geophysical Research: Atmospheres, 2005. **110**(D5).
44. Fjeldbo, G., et al., *The two-frequency bistatic radar-occultation method for the study of planetary ionospheres*. Journal of Geophysical Research, 1965. **70**(15): p. 3701-3710.
45. Feng, M., *Detection of high-latitude ionospheric irregularities from GPS radio occultation*. 2010, MSc dissertation, University of Calgary.
46. Ware, R., et al., *GPS sounding of the atmosphere from low Earth orbit: Preliminary results*. Bulletin of the American Meteorological Society, 1996. **77**(1): p. 19-40.
47. Wickert, J., et al., *Atmosphere sounding by GPS radio occultation: First results from CHAMP*. Geophys. Res. Lett, 2001. **28**(17): p. 3263-3266.
48. Rocken, C., et al., *COSMIC system description*. Terrestrial Atmospheric and Oceanic Sciences, 2000. **11**(1): p. 21-52.
49. Kursinski, E., et al., *Observing Earth's atmosphere with radio occultation measurements using the Global Positioning System*. Journal of Geophysical Research: Atmospheres, 1997. **102**(D19): p. 23429-23465.
50. Hajj, G.A., et al., *CHAMP and SAC-C atmospheric occultation results and intercomparisons*. Journal of Geophysical Research: Atmospheres, 2004. **109**(D6).
51. Staten, P.W., *An Evaluation of Radio Occultation Measurements for Long-term Tropopause Monitoring*. 2008, The University of Utah.
52. Rocken, C., et al., *Analysis and validation of GPS/MET data in the neutral atmosphere*. Journal of Geophysical Research: Atmospheres, 1997. **102**(D25): p. 29849-29866.
53. Anthes, R.A., C. Rocken, and K. Ying-Hwa, *Applications of COSMIC to meteorology and climate*. Terrestrial Atmospheric and Oceanic Sciences, 2000. **11**(1): p. 115-156.
54. Ao, C.O., et al., *Lower troposphere refractivity bias in GPS occultation retrievals*. Journal of Geophysical Research: Atmospheres, 2003. **108**(D18).
55. VISUALS ILLUSTRATING APRIL 12, N.R.; Available from: <http://www2.ucar.edu/news/cosmic-visuals-multimedia-gallery>.

56. Zou, X., H. Liu, and R. Anthes, *A statistical estimate of errors in the calculation of radio-occultation bending angles caused by a 2D approximation of ray tracing and the assumption of spherical symmetry of the atmosphere*. Journal of Atmospheric and Oceanic Technology, 2002. **19**(1): p. 51-64.
57. Occultation Locations for COSMIC, H.; Available from: <http://www.ucar.edu/news/releases/2006/cosmic.shtml>.
58. Abtew, W. and A. Melesse, *Vapor Pressure Calculation Methods*, in *Evaporation and Evapotranspiration*. 2013, Springer. p. 53-62.
59. König, M. *Product Tutorial on Total Precipitable Water Content Products*. Available from: http://www.eumetrain.org/data/3/359/print_2.htm.
60. ATBD, J.A., *Joint Polar Satellite System (JPSS) Advanced Technology Microwave Sounder (ATMS) SDR Radiometric Calibration Algorithm Theoretical Basic Document (ATBD)*. 2011.
61. William J. Blackwell, C.F.C., Richard N. Czerwinski, R. Vincent Leslie, and Idahosa Osaretin, *The Advanced Technology Microwave Sounder (ATMS): New Capabilities for Atmospheric Sensing*, in AMS. 2012: New Orleans, LA.
62. *Megha-Tropiques (Meteorological LEO Observations in the Intertropical Zone)*. Available from: <https://directory.eoportal.org/web/eoportal/satellite-missions/m/megha-tropiques>.
63. Bonsignori, R. *The Microwave Humidity Sounder (MHS): in-orbit performance assessment*. in *Remote Sensing*. 2007. International Society for Optics and Photonics.
64. NOAA. *National Oceanic and Atmospheric Administration instrument Descriptions*. Available from: <http://mirs.nesdis.noaa.gov/instruments.php>.
65. STAR, N., *Sensors GPM GMI Overview*.
66. Ebrahimi, H., et al. *Radiometric inter-calibration of SAPHIR using the Microwave Humidity Sounders*. in *Microwave Radiometry and Remote Sensing of the Environment (MicroRad), 2014 13th Specialist Meeting on*. 2014. IEEE.
67. Wessel, J.E. and D. Boucher Jr, *Comparison between cross-track and conical scanning microwave window channels near 90 GHz*. Geoscience and Remote Sensing, IEEE Transactions on, 1998. **36**(1): p. 16-24.
68. Yang, J.X. and D.S. McKague, *Improving Collocation-Based Scan-Dependent Intercalibration Over the Ocean for Spaceborne Radiometry*. IEEE Geoscience and Remote Sensing Letters, 2016. **13**(4): p. 589-593.

69. Berg, W., et al., *Improved geolocation and earth incidence angle information for a fundamental climate data record of the SSM/I sensors*. IEEE Transactions on Geoscience and Remote Sensing, 2013. **51**(3): p. 1504-1513.
70. Kunee, D.B., et al., *Special sensor microwave imager sounder (SSMIS) radiometric calibration anomalies—Part I: Identification and characterization*. IEEE Transactions on Geoscience and Remote Sensing, 2008. **46**(4): p. 1017-1033.
71. Imaoka, K., et al. *Post-launch calibration and data evaluation of AMSR-E*. in *Geoscience and Remote Sensing Symposium, 2003. IGARSS'03. Proceedings. 2003 IEEE International*. 2003. IEEE.
72. Greenwald, T.J. and S.A. Christopher, *Effect of cold clouds on satellite measurements near 183 GHz*. Journal of Geophysical Research: Atmospheres, 2002. **107**(D13).
73. Adler, R.F., et al., *Aircraft microwave observations and simulations of deep convection from 18 to 183 GHz. Part I: Observations*. Journal of Atmospheric and Oceanic Technology, 1990. **7**(3): p. 377-391.
74. Moradi, I., et al., *Intercalibration and validation of observations from ATMS and SAPHIR microwave sounders*. Geoscience and Remote Sensing, IEEE Transactions on, 2015. **53**(11): p. 5915-5925.
75. Wilheit, T.T. *Comparisons of SAPHIR with MHS on METOP-A, NOAA 18, & NOAA19*. in *Toulouse XCAL meeting*. 2013. Toulouse , france.
76. Kishore, P., et al., *Global (50 S-50 N) distribution of water vapor observed by COSMIC GPS RO: Comparison with*. Issue: Journal of Atmospheric and Solar-Terrestrial Physics, 73 (13), 2011.
77. Wilheit, T., et al. *Intercalibrating the GPM constellation using the GPM Microwave Imager (GMI)*. in *2015 IEEE International Geoscience and Remote Sensing Symposium (IGARSS)*. 2015. IEEE.
78. Wang, W.B.S.B.R.C.S.D.D.D.H.E.S.F.W.L.J.R.K.D.M.V.P.J., *Intercalibration of the GPM Microwave Radiometer Constellation*. Journal of Atmospheric and Oceanic Technology, 2016.
79. Ebrahimi, H., S. Datta, and W.L. Jones. *Investigation of radiative transfer model effect on radiometric inter-calibration of GPM sounder channels*. in *2015 IEEE International Geoscience and Remote Sensing Symposium (IGARSS)*. 2015. IEEE.